University of Bath

PHD

The corrosion of metal matrix composites

Coleman, Sarah L.

Award date:
1991

Awarding institution:
University of Bath

Link to publication

Alternative formats
If you require this document in an alternative format, please contact:
openaccess@bath.ac.uk

Copyright of this thesis rests with the author. Access is subject to the above licence, if given. If no licence is specified above, original content in this thesis is licensed under the terms of the Creative Commons Attribution-NonCommercial 4.0 International (CC BY-NC-ND 4.0) Licence (https://creativecommons.org/licenses/by-nc-nd/4.0/). Any third-party copyright material present remains the property of its respective owner(s) and is licensed under its existing terms.

Take down policy
If you consider content within Bath's Research Portal to be in breach of UK law, please contact: openaccess@bath.ac.uk with the details. Your claim will be investigated and, where appropriate, the item will be removed from public view as soon as possible.

Download date: 05. May. 2023

THE CORROSION OF METAL MATRIX COMPOSITES

submitted by

Sarah L Coleman

for the degree of PhD

School of Materials Science

University of Bath

1991

Copyright

Attention is drawn to the fact that copyright of this Thesis rests with the author. This copy of the Thesis has been supplied on condition that anyone who consults it is understood to recognise that its copyright rests with its author and no quotation from the Thesis and no information derived from it may be published without the prior consent of the author. This Thesis may be made available for consultation within the University Library and may be photocopied or lent to other libraries for the purposes of consultation.

Signed .....

UMI Number: U042357

All rights reserved

INFORMATION TO ALL USERS
The quality of this reproduction is dependent upon the quality of the copy submitted.

In the unlikely event that the author did not send a complete manuscript
and there are missing pages, these will be noted. Also, if material had to be removed,
a note will indicate the deletion.

UMI U042357
Published by ProQuest LLC 2013. Copyright in the Dissertation held by the Author.
Microform Edition © ProQuest LLC.
All rights reserved. This work is protected against
unauthorized copying under Title 17, United States Code.

ProQuest LLC
789 East Eisenhower Parkway
P.O. Box 1346
Ann Arbor, MI 48106-1346

UNIVERSITY OF BATH
LIBRARY
25 17 SEP 1992
PHD

ACKNOWLEDGEMENTS

I gratefully acknowledge Professors V.D. Scott and B. McEnaney for their continued supervision and guidance during this project. I would like to thank Mr. K.R. Stokes for his helpful advice and discussion and also the Technical Staff of the School of Materials Science for their support. Finally I would like to acknowledge the financial support of the Science and Engineering Research Council and the MOD Procurement Executive.

SUMMARY

The corrosion characteristics of aluminium alloys containing a number of ceramic reinforcements has been investigated. The reinforcements included continuous carbon and Nicalon fibres, short alumina (Saffil) fibres and silicon carbide particulate. The matrix metals consisted of aluminium, an Al-7Si-0.5Mg casting alloy and an Al-4Cu-1.5Mg precipitation hardening alloy. The composites were fabricated either by liquid metal infiltration (LMI), squeeze casting or powder metallurgy.

The corrosion studies have been carried out using natural immersion and accelerated corrosion methods such as the cyclic polarisation test. Special attention has been focused on a double cyclic polarisation technique. This has proved to be invaluable for predicting the susceptibility of MMC to pitting attack, good correlation having been found between pitting and protection potentials derived from this method and those from open circuit potential measurements made under natural immersion conditions. The electrochemical studies have been combined with detailed microstructural analysis.

Examination of the corroded surfaces and sections through the corroded material has been carried out using optical, scanning electron microscopy (SEM), transmission electron microscopy (TEM) and energy dispersive spectroscopy (EDS). These have enabled the sites of corrosion attack to be identified, such as fibre/matrix interfaces, secondary and intermetallic phases and pores and crevices caused by poor infiltration during fabrication.

The MMC containing the most electrically conducting fibre, carbon, appeared to suffer the greatest degree of attack at fibre/matrix interfaces. The effect was not wholly due to a galvanic action, but to the presence of a reaction product, aluminium carbide, Al_4C_3, which reacted strongly with water. The geometry of the reinforcement was found to effect the propagation of corrosion pits. Continuous fibres tended to act as barriers and channel the corrosion along the fibres, whereas the Saffil short fibres and SiC particulate allowed lateral growth of corrosion pits.

The chemical composition of the metal matrix was found to play an important role regarding corrosion sites. In particular intermetallics containing iron, present largely as an impurity, proved detrimental to the corrosion resistance and caused enhanced attack of the surrounding metal due to a microgalvanic action. The method of composite manufacture also affected the corrosion process and was related to pores caused by poor infiltration in regions of densely-packed fibres.

CONTENTS

	Page
CHAPTER 1 INTRODUCTION	1
CHAPTER 2 LITERATURE SURVEY	5
2.1 Fabrication of Metal Matrix Composites	5
2.1.1 Liquid Phase Methods	6
(a) Squeeze Casting	6
(b) Liquid Metal Infiltration	7
(c) Compocasting	8
(d) Spray Deposition	9
2.1.2 Solid Phase Methods	10
(a) Powder Metallurgy	10
(b) Diffusion Bonding	10
2.2 Corrosion of Aluminium and its Alloys	11
2.2.1 Pitting Corrosion of Aluminium	13
2.2.2 Crevice Corrosion	15
2.3 Methods of Corrosion Testing	17
2.3.1 Gravimetry	17
2.3.2 Open Circuit Potential	18
2.3.3 Polarisation Techniques	19
(a) Potentiokinetic Methods	20
(i) Anodic Polarisation	20
(ii) Cyclic Polarisation	20
(b) Potentiostatic Method	24
2.3.4 Scratch Technique	25
2.3.5 Pit Propagation Rate Method	27
2.4 Corrosion of Aluminium Metal Matrix Composites	28
2.4.1 Silicon Carbide-reinforced Al Alloy	28
2.4.2 Carbon-reinforced Al Alloy	32
2.4.3 Boron-reinforced Al Alloy	36
2.5 Aims of the Present Investigation	38
CHAPTER 3 EXPERIMENTAL DETAILS	40
3.1 Materials	40
3.1.1 Matrix Metals	40
3.1.2 Reinforcements	40
3.1.3 Metal Matrix Composites	42
3.1.4 Fabrication of MMC by Squeeze Casting	42
3.2 Preparation of Test Specimens	43
3.2.1 Unreinforced Matrix Metals	43
3.2.2 Metal Matrix Composites	44
3.2.3 Transmission Electron Microscopy Specimens	45
3.2.4 Aluminium Single Crystal Specimens	45

3.3 Corrosion Testing 46
3.3.1 Corrosion Test Environment 46
3.3.2 Gravimetry 46
3.3.3 Open Circuit Potential 47
3.3.4 Potentiodynamic Polarisation 48
(a) Apparatus 49
(b) Anodic Polarisation 50
(c) Double Cyclic Polarisation 50
3.3.5 Potentiostatic Polarisation 51
3.3.6 Galvanic Couples 51

3.4 Microstructural Study 52
3.4.1 Optical Microscopy 52
3.4.2 Quantitative Microscopy 52
3.4.3 Scanning Electron Microscopy 53
3.4.4 Transmission Electron Microscopy 54
3.4.5 Electron-Probe Microanalysis 55
3.4.6 Measurement of Oxide Film Thickness 56

CHAPTER 4 RESULTS 61

4.1 Assessment of the Polarisation Technique 61
4.1.1 The Polarisation Apparatus 61
4.1.2 The DCP Method 62
(a) Definition of a Protection Potential 62
(b) Definition of the Characteristic Potentials from a DCP curve 63
(c) Sensitivity of the DCP Technique 65

4.2 Characterisation of as-received Materials 66
4.2.1 Materials Based Upon Al-Si-Mg (357) Alloy 67
(a) 357 Alloy 67
(b) Carbon-reinforced 357 Produced by Liquid Metal Infiltration 68
(c) Carbon-reinforced 357 Produced by Squeeze Casting 69
(d) Nicalon-reinforced 357 70
(e) Saffil-reinforced 357 71

4.2.2 Materials Based Upon Al-Cu (2124) Alloy 71
(a) 2124 Alloy 71
(b) Carbon-reinforced 2124 72
(c) SiC-reinforced 2124 73

4.2.3 Materials Based Upon Al 74
(a) Commercial Purity Aluminium 74
(b) Carbon-reinforced Super Purity Al 74

4.3 Corrosion Studies on 357 Alloy 76
4.3.1 Gravimetry 76
4.3.2 Open Circuit Potential 76
4.3.3 Double Cycle Polarisation 77
(a) 20mV/min Scan Rate 77
(b) 2mV/min Scan Rate 78
4.3.4 Corrosion Morphology 79

4.4 Corrosion Studies on Carbon-reinforced 357 (LMI) 81
4.4.1 Gravimetry 81
4.4.2 Open Circuit Potential 81
4.4.3 Double Cycle Polarisation 82
(a) 20mV/min Scan Rate 82
(b) 2mV/min Scan Rate 83
4.3.4 Galvanic Couple 84
4.4.4 Corrosion Morphology 85

4.5 Corrosion Studies on Carbon-reinforced 357 (squeeze cast) 87
4.5.1 Open Circuit Potential 87
4.5.2 Double Cycle Polarisation 87
4.5.3 Corrosion Morphology 88

4.6 Corrosion Studies on Nicalon-reinforced 357 89
4.6.1 Gravimetry 89
4.6.2 Open Circuit Potential 89
4.6.3 Double Cycle Polarisation 90
(a) 20mV/min scan rate 90
(b) 2mV/min scan rate 90
4.6.4 Galvanic Couple 91
4.6.5 Corrosion Morphology 91

4.7 Corrosion Studies on Saffil-reinforced 357 93
4.7.1 Gravimetry 93
4.7.2 Open Circuit Potential 93
4.7.3 Double Cycle Polarisation 93
(a) 20mV/min scan rate 93
(b) 2mV/min scan rate 94
4.7.4 Corrosion Morphology 95

4.8 Corrosion Studies on 2124 Alloy 95
4.8.1 Gravimetry 95
4.8.2 Open Circuit Potential 96
4.8.3 Double Cycle Polarisation 96
4.8.4 Corrosion Morphology 97

4.9 Corrosion Studies on Carbon-reinforced 2124 97
4.9.1 Open Circuit Potential 97
4.9.2 Double Cycle Polarisation 97
4.9.3 Galvanic Couple 98
4.9.4 Corrosion Morphology 98

4.10 Corrosion Studies on SiC-reinforced 2124 100
4.10.1 Gravimetry 100
4.10.2 Open Circuit Potential 100
4.10.3 Double Cycle Polarisation 100
4.10.4 Corrosion Morphology 101

4.11 Corrosion Studies on Commercial Purity Aluminium 102
4.11.1 Gravimetry 102
4.11.2 Open Circuit Potential 102
4.11.3 Double Cycle Polarisation 102
4.11.4 Corrosion Morphology 103

4.12 Corrosion Studies on Carbon-reinforced Al 103
4.12.1 Open Circuit Potential 103
4.12.2 Double Cycle Polarisation 104
4.12.3 Galvanic Couple 104
4.12.4 Corrosion Morphology 105

CHAPTER 5 DISCUSSION 106

5.1 General Observations of the Corrosion Tests 106
5.1.1 Gravimetry 106
5.1.2 Open Circuit Potential 109
5.1.3 Double Cycle Potential 112
(a) Sensitivity of the DCP Technique 114
(b) Effect of Scan Rate 115
(c) The Inflection Potential 117
5.1.4 Galvanic Couple 119

5.2 Assessment of the Corrosion Tests 121
5.2.1 Comparison of OCP and DCP Tests 121
5.2.2 Assessment of Other Parameters to Characterise Corrosion 124

5.3 Materials 126
5.3.1 Effect of Reinforcement 126
5.3.2 Effect of Matrix Alloy 129
5.3.3 Effect of Second Phases 130
5.3.4 Effect of Fabrication Route 133

CHAPTER 6 CONCLUSIONS 137

6.1 Corrosion Test Methods 137
6.2 Corrosion of MMC 139

REFERENCES

TABLES

DIAGRAMS

CHAPTER 1

INTRODUCTION

The concept of using strong, stiff fibres to reinforce materials is by no means a recent idea. The incorporation of straw within mud for use as a building material was an ancient development and even nature resorts to composites for load bearing structures in the form of wood and bone. More recently, composites comprising of ceramic or metal reinforcements in plastic, metal and ceramic matrices have evolved with potential advantages over their component materials.

Metal matrix composites (MMC) offer improvements over conventional alloys in applications where low density and high strength and stiffness are prime requirements. The fibres confer the strength, rigidity and toughness to the metal matrix which is relatively ductile. MMC also have the capacity to withstand higher temperatures without loss of mechanical properties, than many of the fibre reinforced plastics. Thus MMC provide the possibility to make considerable weight savings particularly in aerospace applications where reducing weight is a prime requirement.

Research into MMC during the 1960s focused mainly upon a boron fibre reinforcement but this met with only limited success. Poor composite properties were found as a result of chemical reactions occuring between the fibre and matrix at the high temperatures used in manufacture. Fabrication routes were therefore restricted to solid state processes such as diffusion bonding.

Advances in ceramic fibre technology such as chemical vapour deposition processes and methods of coating fibres brought about renewed interest in

MMC during the early 1970s. Furthermore, the development of relatively inert fibres such as silicon carbide and alumina, has encouraged the developement of liquid phase fabrication routes, whilst progress in powder metallurgy (PM) technology has lead to the production of particulate reinforced metals by a PM route.

A revival in interest and a more realistic appraisal of potential of MMC has led to increased effort on characterising their mechanical properties. However comparatively little attention has been given to their secondary properties such as corrosion.

Most research into the corrosion behaviour of MMC has concentrated on matrix materials of aluminium and its alloys. The corrosion properties of these metals are well understood, aluminium alloys having long been used in marine environments owing to their generally good corrosion resistance and their light weight. The improved mechanical properties offered by reinforcing these materials with fibres have re-established interest in these materials for marine applications. Consequently there is a great need for knowledge concerning the modification of corrosion properties brought about by a fibre reinforcement.

Research to date has been based upon aluminium and on Al-Mg-Si alloys reinforced with carbon, silicon carbide or boron fibres. The general findings are that the corrosion behaviour of the composites is more severe than that of the unreinforced metal. Crevices, pores, interfacial reaction products and galvanic coupling in the composite may result in enhanced or localised attack of the matrix. Furthermore, the presence of reinforcing fibres in metals such as aluminium which are covered with a protective

oxide film, may, by impairing the continuity of the surface oxide, thereby promote localised attack.

The aim of the present study was to investigate not only the corrosion properties of these new materials, but also to establish experimental techniques which might be most accurately applied to obtain corrosion data on MMC.

The MMC employed in this investigation were fabricated by liquid metal infiltration (LMI), squeeze casting or powder metallurgy and had matrices of pure aluminium, an Al-7Si-0.5Mg casting alloy or an Al-4Cu-1.5Mg precipitation hardening alloy. Carbon, and Nicalon (essentially silicon carbide) continuous fibres, Saffil (alumina) short fibre and silicon carbide particulate were employed as reinforcements.

The corrosion behaviour of the MMC has been studied in de-aerated, 3.5wt% NaCl solution during simple immersion and also under accelerated conditions, where specimens were forced to corrode by an applied potential. The double cycle polarisation (DCP) test is an accelerated test, which was employed in parallel with the simple immersion tests to predict susceptibility of the MMC to pitting corrosion.

The microstructures of the materials have been characterised both before and following corrosion using optical and scanning electron microscopy (SEM), and energy dispersive spectrometry (EDS) to establish the chemical composition of the preferential sites of corrosion attack.

The thesis is composed of five chapters in addition to this introduction. The second chapter presents a survey of the literature relating to the

fabrication of metal matrix composites, the corrosion of aluminium, the techniques which have most commonly been applied to assess the corrosion of aluminium and its alloys, and finally the corrosion of MMC. The experimental procedures are presented in the third chapter, which includes details of the preparation of materials, the corrosion test apparatus and the equipment used for microstructural studies. The results of the corrosion tests and microstructural investigations are reported in Chapter four. Chapter five is a discussion of the findings from this investigation, which focuses upon the corrosion test methods and the corrosion behaviour of the materials in relation to the reinforcement type, the matrix alloy, the fabrication route and the role of second phases. Finally, Chapter six presents the conclusions which have been drawn from this study.

CHAPTER 2

LITERATURE SURVEY

The literature survey comprises four sections. In the first part, the fabrication methods which have been applied to MMC are described and the second part is a discussion of the corrosion behaviour of aluminium. The most popular methods of corrosion testing are reviewed in the third section, and the fourth section reports the findings which have been published of the limited corrosion studies on MMC. Finally, the fifth section summarises the aims of this investigation in the light of the literature review.

2.1 FABRICATION OF METAL MATRIX COMPOSITES

Many fabrication routes have been explored for the production of MMC, with varying degrees of success. The main difficulties involve firstly, the incorporation of brittle reinforcements into a matrix without incurring breakages, and secondly, achieving a strong interface between the reinforcement and matrix without the formation of detrimental reaction products.

Fabrication methods may be broadly classified into two groups; (i) solid state processes, which operate below the melting point of the matrix and (ii) liquid phase processes, which are conducted above the melting point of the matrix. The process selected depends to a great extent upon the choice of reinforcement and matrix. Liquid phase routes offer the advantage of intimate reinforcement-matrix contact which reduces residual porosity in the final composite. Solid state processes on the other hand are less likely to promote the formation of adverse interfacial reactions products as

reported by Levi *et al* (1978), Lloyd (1989) and Yang and Scott (1991a). The most popular fabrication routes will now be discussed.

2.1.1 LIQUID PHASE FABRICATION PROCESSES

(a) Squeeze Casting

One of the most successful techniques for fabricating MMC is squeeze casting, illustrated schematically in Fig.2.1. Considerable research has been dedicated to this process owing to its potential for producing near-net shape components which require little or no secondary processing. The method, which is described by Harris (1988 & 1989), Chadwick (1990) and Bader *et al* (1985), involves infiltration of a pre-heated fibre preform by the molten metal. Pressures of up to 100MPa are applied by an hydraulic ram. This is maintained until solidification begins, thereby forcing the metal into the preform, infiltrating the fibres, compressing any gas bubbles and feeding shrinkage as it occurs. The advantage of applying pressure during the casting process, as stated by Chadwick and Yue (1989), is that gas or shrinkage porosity is almost eliminated. In addition it opens up the possibility of producing composites with metal matrices not normally used during casting owing to poor fluidity in the molten state.

Components fabricated by this method have been found to possess mechanical properties which are equal to or greater than wrought products of the same compositions. Das and Chaterjee (1981) noted that the good mechanical properties resulted from the fine grain microstructure which was characterised by small dendrites, small

constituent particles and a more homogeneous distribution of structural components.

The major disadvantage of squeeze casting lies with the high pressures involved. Damage to brittle reinforcements may occur, particularly when the reinforcement is present in high volume fractions. Also the necessity for such high pressures limits the size of component which can be produced by this method.

(b) Liquid Metal Infiltration

The liquid metal infiltration (LMI) process is proving to be one of the most promising production routes for MMC. The LMI method, described by Mykura (1988 & 1991) and Chiou and Chung (1991), is similar to that of squeeze casting with the difference that the process is operated under vacuum and the pressure is applied by inert gas. The essential procedure, illustrated schematically in Fig.2.2, is as follows.

A preheated fibre preform is placed into a split metal die, also preheated and in the shape of the component. The die is then closed and the die and molten metal reservoir chamber evacuated of all air down to a pressure of <1mbar. The melt chamber is pressurised to ~1000psi (~7MPa) by an inert gas such as argon, which forces the molten metal into the die so as to infiltrate the fibre preform. The molten metal is kept under pressure until solidification occurs. The gas pressure is then removed, the system vented and the die opened. As with squeeze casting it has the advantage of near-net-shape forming with little or no further processing required, although the size and complexity of the component is not as restricted; indeed Mykura (1988) has reported parts of up to two metres long having been

produced by this method. In addition it has an advantage over squeeze casting in that the pressures involved are over an order of magnitude lower, thereby minimising preform compression.

One of the major draw backs of the LMI technique lies with control of the operating temperature. Masur *et al* (1987) have shown that infiltration has a strong dependance on fibre temperature. Too low a fibre temperature results in solidification of the metal prior to complete infiltration and hence porosity in the cast. However, if the fibre temperature is too high, the long solidification time promotes the possibility of undesirable reactions occurring at the fibre/matrix interface. Indeed, Yang and Scott (1991a) have shown that the formation of aluminium carbide at the fibre/matrix interface in a carbon-reinforced Al-Si alloy produced by LMI has a very detrimental effect upon the mechanical properties of the composite.

(c) Compocasting

Compocasting is a useful technique for the fabrication of MMC containing short fibres, whiskers or particulates. The technique, described by Levi *et al* (1978) and Zhu (1988), involves the addition of a discontinuous reinforcement to a semi-solid slurry which has been produced by stirring the molten metal as it cools until it is approximately 30-50% solid. The reinforcement therefore becomes mechanically trapped by the slurry. Stirring continues as the mixture cools. This promotes intimate contact between the metal and reinforcement by repeatedly breaking the alumina skin which forms on the aluminium surface. Interactions are likely to occur between the reinforcement and the matrix by this method which limits the process to certain reinforcement-matrix combinations.

Furthermore, Harris (1988) noted that extensive fibre damage may result from the compocasting process, making it more suitable for fabricating particle-reinforced composites.

Following mixing, the slurry is poured from the bottom of the crucible into a mould. Alternatively, it may undergo further processing in the form of squeeze casting, as described by Milliere and Suery (1988) and Karandikar and Chou (1991). The advantage of following compocasting with squeeze casting is that porosity associated with traditional casting processes is considerably reduced.

(d) Spray Deposition

The production of particulate-reinforced composites by spray deposition has been researched by White and Willis (1989). The matrix metal, which is contained in a crucible, is heated by induction until molten. The crucible is then pressurised and the molten metal is injected into an atomiser. An atomised stream of metal is produced into which is introduced the particulate reinforcement. The metal and particulate are then co-deposited onto a substrate which is placed in the line of flight. Careful control of the atomising and particulate feeding is required to ensure a uniform distribution of the reinforcement within the matrix. Although still in the research stages, White and Willis (1989) believe it to be capable of producing 100kg ingots with a homogeneous, fine-grain microstructure. An advantage of the method is that the short contact times during spraying, limits the formation of undesirable interfacial reaction products.

2.1.2 SOLID STATE FABRICATION PROCESSES

(a) Powder Metallurgy

Short fibre or particulate reinforcements may successfully be incorporated into a matrix by a powder metallurgy fabrication process. The process involves mixing and blending the metal powders with the reinforcement in the required proportions until there is a homogeneous dispersion of the reinforcement. The powder mix then undergoes consolidation to form a green compact, before being hot isostatically pressed. The composite may then be extruded into billets and hot rolled into a sheet form.

As noted by Mileiko (1989) the technique involves lower processing temperatures and, therefore, a greater control of the reinforcement-matrix interface properties. In addition, the extrusion stage leads to orientation of the whiskers, which may be desirable for many applications. The method also produces composites which have uniform distributions of the reinforcement. Disadvantages are the limited availability of pre-alloyed powders, and the high level of cleanliness required to prevent inclusions in the final product as noted by White and Willis (1989).

(b) Diffusion Bonding

Continuous fibres and matrix may be combined in the solid state by diffusion bonding, which involves the simultaneous application of heat and static pressure. The process, which is described by Chou *et al* (1985) and has been employed for a variety of systems by Alexander *et al* (1968), is generally applied to the consolidation of lay-ups of metal-foils and fibre-arrays, or to tape or wire preforms which have been fabricated by

chemical vapour deposition, plasma spraying, electrodeposition or hot rolling.

The advantage of this technique lies with the relatively low temperatures involved. However, the process is expensive and the high pressures involved are likely to lead to fibre breakages. Furthermore, as noted by Harris (1989), difficulties may arise with the penetration of the filament layers by the metal foils to form a fully dense material.

2.2. CORROSION OF ALUMINIUM AND ITS ALLOYS

Aluminium owes its good corrosion resistance to the tenacious oxide film which covers its surface. The alumina film which is only ~25-50Å thick is highly protective in most environments and if damaged, reforms immediately, restoring corrosion protection to the metal. However, under certain conditions of potential and pH, as expressed by the Pourbaix diagram for aluminium, Fig.2.3, the protective film is unstable and corrosion may occur. Aluminium is passive between pH4 and pH8.5, but in more acidic or more alkaline environments, corrosion in the form of localised attack is possible. In addition, corrosion of aluminium may take place in near-neutral solutions where aggressive anions such as chloride ions are present.

The oxide film thickens in air at a slow rate which decreases with time, but in aqueous environments, the rate of film growth is much greater. The initial corrosion product is thought to be aluminium hydroxide which changes with immersion time to become hydrated aluminium oxide. The aqueous formed film, although thicker, is less adherent and consequently does not offer the same level of protection.

It is well established that the mechanisms of the corrosion process in aqueous environments are electrochemical. When a metal is immersed in solution, certain areas of the metal acquire a different electrode potential from the remainder of the surface. Localised cathodic and anodic areas therefore become established, the anodic sites having the more negative electrode potential. This results in dissolution of the anodic sites due to the flow of current between the regions of different potential. On some metals, (Chandler, 1985), corrosion at the anodic sites becomes stifled and new anodic areas adjacent to the old ones become active, the interchange of anodic and cathodic areas leading to an almost uniform attack over a period of time. However for some materials this interchange of sites does not occur and so the corrosion becomes localised at a number of anodic sites on the surface, the remainder of the surface being largely cathodic. The respective anodic and cathodic reactions are as follows;

Anodic:

$$2Al \longrightarrow 2Al^{3+} + 6e^-$$

Cathodic:

$$6H_2O + 6e^- \longrightarrow 6OH^- + 3H_2$$

$$3/2O_2 + 6e^- + 3H_2O \longrightarrow 6OH^-$$

Under certain conditions, the aluminium and hydroxyl ions may combine to form hydrated Al_2O_3 corrosion product.

The mechanisms of the localised corrosion of aluminium, namely pitting and crevice attack, will now be discussed.

2.2.1 PITTING CORROSION OF ALUMINIUM

Pitting corrosion may be described as the local dissolution of metal from a passivated metal or alloy which is immersed in near-neutral solutions containing aggressive ions such as chloride ions. Many theories have been proposed regarding the initiation and growth of corrosion pits, the theory being dependant to some extent upon the experimental approach adopted.

A mechanism given by Hoar *et al* (1965), based upon their studies into pitting, suggested that the initiation of pits involved the adsorption of activating anions, particularly chloride ions, at specific sites on the metal surface such as impurities or grain boundaries. The aggresive anions penetrated the film under the electrostatic field across the film/solution interface when the film reached a critical value corresponding to the breakdown potential. Either the anions would travel completely through the film, or the metal cations would travel outwards to meet them. The film was thus "contaminated" with ions and hence became a superior ion conductor compared with the original passive film. This resulted in the rapid release of cations at the film/solution interface, thereby promoting pitting.

Richardson and Wood (1970) studied the pitting of aluminium by scanning electron microscopy and concluded that flaws in the surface oxide film acted as nucleation sites for pitting. The flaws could be of a "residual" type produced during film growth at impurity-rich regions, or could be "mechanical" in origin, associated with stress relief in the film resulting from oxide formation over mechanical surface defects, *e.g.* scratch lines. Pits would initiate at these weak spots and propagate by metal dissolution of the sample and the undermining of the oxide film.

Intermetallic or second phases are also common sites for pit initiation. Hubner and Wranglen (1964) reported that pits can be initiated in the surface of aluminium, by iron-rich precipitates, probably $FeAl_3$, which act as local cathodes. Similar observations were made by Murray *et al* (1967), who discovered that the process could be accelerated by the presence of a small amount of copper ions in the water. The effect was related to the deposition of copper on the $FeAl_3$ particles which made them more efficient as cathodes in the corrosion process.

In their studies on an Al-Mg alloy, Gehring and Peterson (1981) found that pits initiated at intermetallics of the type $(CrFeMn)Al_6$. They attributed this to the less protective nature of the oxide film at the intermetallic particles and also to the galvanic action between the aluminium matrix and the more noble intermetallics.

Once initiated, the propagation of corrosion pits can be rapid, the process being autocatalytic as noted by Hoar *et al* (1965). Such behaviour was considered to arise from the high concentration of chloride ions within the pit, which reduced the pH of the electrolyte to more acidic levels. From studies of the pitting of aluminium, Hubner and Wranglen (1964) thus described the self-generating conditions for pit propagation as follows.

(1) Inside the pit, preventing repassivation there is,

(a) a limited supply of oxygen,

(b) a low pH due to hydrolysis of metal ions,

(c) a migration of chloride ions into the pit owing to the current generated by the pit, and

(d) the formation of a concentrated salt solution of high electrical conductivity.

(2) In the pit mouth, an hydroxide diaphragm forms, preventing mixing of the solution inside the pit with the bulk solution, and hence strengthening the factors described in (1).

(3) Outside the pit, preventing general attack there is,

(a) cathodic protection of the surrounding surface by the corrosion current,

(b) alkali passivation, particularly in the presence of calcium bicarbonate, and

(c) deposition of more noble metals, particularly copper, which increases the effectiveness of cathodic sites and facilitates the maintenance of an electrode potential more noble than the critical or breakthrough potential within the pit.

2.2.2 CREVICE CORROSION

The mechanism of crevice corrosion is not unlike pitting corrosion and indeed, once initiated, proceeds in a similar fashion. However, it is distinguishable from pitting in the initiation phase. Whereas pits form generally on plane surfaces due to the metallurgical factors described in the previous section, crevice corrosion is initiated by differential concentrations of oxygen or ions in the electrolyte between the crevice and its surroundings.

Fontana (1987) noted that two basic reactions occurred on the metal surface; (i) metal dissolution to metal ions and (ii) oxygen reduction to hydroxide ions. He proposed that initially the reactions occurred uniformly over the entire surface, including the interior of the crevice, the

generation of metal ions being counter-balanced electrostatically by the creation of negative hydroxyl ions. However, after a while, the oxygen within the crevice became depleted because the oxygen was more readily replaced at the surface than in the crevice. Thus within the crevice, the cathodic process was impeded by the depletion of oxygen and eventually the reaction ceased. The dissolution of metal within the crevice continued, however, creating an excess positive charge. In order to balance the charge, negative ions such as chloride ions migrated into the crevice to balance the charge. This results in an increase in the concentration of metal chloride in the crevice. The metal chloride was readily hydrolysed in water by the following process:

$$M^+Cl^- + H_2O = MOH + H^+Cl^-$$

The HCl dissociated in water and the resulting increase in hydrogen ion concentration accelerated the metal dissolution. An auto-catalytic situation was thus established. As the corrosion within the crevice increased, the oxygen reduction process on the surrounding surface increased, thereby cathodically protecting the surface.

Oldfield *et al* (1987) summarised the above mechanism as occurring in four stages;

(a) de-aeration within the crevice caused by the consumption of oxygen during the maintenance of a passive film,

(b) a decrease in the pH and an increase in the chloride concentration of the crevice solution caused by metal hydrolysis, and migration of chloride ions into the crevice respectively,

(c) breakdown of the passive film in the crevice due to the build-up of a "critical crevice solution", and

(d) propagation of crevice corrosion.

2.3 CORROSION TEST METHODS FOR ALUMINIUM

A variety of techniques are available for the corrosion testing of materials, and these range from the very simple to the very complex. The simple tests involve measurement of the weight loss of metal caused by exposure to a corrosive environment (gravimetry). The more complex tests are based upon electrochemical principles and involve measurement of the minimum potential at which pits are initiated, the pitting potential, E_{pit}. The common corrosion test methods for aluminium will now be discussed.

2.3.1 GRAVIMETRY

Gravimetry, which involves measuring the mass of material corroded away over a known period of time, can yield reasonable accuracy when good cleaning procedures are employed for the removal of corrosion products from the surface but, as noted by Barnartt (1976) and Schrier (1978), the corrosion rates measured by this method are only an average value. The method implies that the corrosion has occurred at a constant rate throughout the test and that the surface has been uniformly attacked. However, this is rarely the case, firstly because corrosion rate tends to diminish with time and secondly because materials such as aluminium are susceptible to localised attack.

Nisancioglu and Holtan (1979) successfully employed the gravimetric method in corrosion studies on a range of aluminium alloys. To overcome

the problem of the change in corrosion rate with time, they measured the weight loss due to pitting as a function of immersion time and concluded that gravimetry was a valuable technique when it was used as a comparative test and combined with electrochemical methods.

Indeed, the consensus is that gravimetric tests should be conducted with caution. The weight loss should be calculated over a range of immersion times, and the results analysed and compared with data from other test methods.

2.3.2 OPEN CIRCUIT POTENTIAL

The open circuit potential test is an electrochemical technique which involves the measurement of potential changes with respect to time of a freely-corroding specimen. The technique is often considered as being erratic, but Nisancioglu and Holtan (1978a & 1979) have shown that with careful interpretation of the data, fairly accurate results may be achieved. They proposed that the potential-time plots obtained from open circuit potential (OCP) measurements could be divided into four distinct regions, Fig.2.4, which relate to different surface behaviour. Region I corresponds to pit initiation and lasts for ~1 minute, whereas region II, which represents pit propagation, may continue for several hours. The quasi-stationary potential in region II corresponds to the pitting potential, E_{pit}. They observed oscillations, mostly as potential surges in the positive direction, in region I and the early part of region II. These became changes in the negative direction in the latter part of region II and continued into region III, where the potential declined to more negative values. This region they believed to correspond to a reduction in the cathodic area and lower pit current densities, in agreement with Bond *et*

al (1966), the result being a switch from anodic to cathodic control in region III. Thus repassivation occurs in region IV and the rapid surges in potential disappear.

Foroulis and Thubrikar (1976) showed there to be good correlation between the pitting potential and the OCP when conducting corrosion studies on aluminium. They found that a necessary prerequisite for the nucleation of pits in pure aluminium when immersed in chloride solutions is that the OCP must at some stage become more positive than the pitting potential for a period of time which is sufficient for pits to nucleate. Once nucleated, any pits that have been initiated may be sustained at more negative potentials than E_{pit}, although no new pits will initiate.

Sherif and Narayan (1989) investigated the variation in OCP with immersion time of aluminium and found that the effects of aluminium purity, surface treatment, oxygen content and pH of solutions, and mechanical agitation all affected the OCP response.

Wood *et al* (1974) confirmed that surface roughness affected the OCP and reported that the initial phase of the OCP curve, which is associated with pit initiation, is more reproducible if the surface preparation is kept constant. The latter stages were less reproducible, regardless of surface preparation.

2.3.3 POLARISATION TECHNIQUES

The major disadvantages of natural immersion methods, such as those just described, lies with the long periods of immersion which may be required. In some cases exposure of the specimens to the corrosive

solution may take months or even years to produce useful data. This is unacceptable for many studies, and therefore a form of accelerated test is desirable. Polarisation tests, which involve controlling the potential of the specimen, are often employed for this reason.

(a) Potentiokinetic Tests

(i) Anodic Polarisation

Anodic polarisation involves applying a potential to a specimen whilst measuring the corresponding current induced within it. If a material which is susceptible to localised attack is polarised in a positive (anodic) direction, then the potential at which pits become initiated produces a corresponding increase in the current density. A typical anodic polarisation curve is illustrated in Fig.2.5.

The first experiments using the anodic polarisation technique were conducted by Brennert (1937) on specimens of iron. He noted an increase in current and attributed it to breakdown of the passive surface layer. He named this potential the break-through potential, although it is now more usually called the pitting potential, E_{pit}. In general, the more positive the pitting potential, the more resistant the material is to pitting attack. The anodic polarisation method may be used to investigate the influence of different factors such as heat-treatments or the fabrication process of a particular material.

(ii) Cyclic Polarisation

A variation of the above method which is often employed is the cyclic polarisation test, a schematic illustration of a cyclic polarisation curve

being given in Fig.2.6. Pourbaix *et al* (1963) discovered that a second important potential could be defined from this method, which they called the protection potential, E_{prot}. The method involves anodically polarising a specimen by increasing the potential until it is more positive than E_{pit}, so that the passive film is broken down and pitting occurs (the forward scan). The direction of the potential scan is then reversed, and the specimen is polarised in the cathodic direction until the curve intersects the forward scan thereby forming a loop. This intersection between the forward and reverse scans, E_x in Fig.2.6, was described by Pourbaix *et al* (1963) as the protection potential, E_{prot}, the potential at which pits were no longer active and the passive layer was restored. Otani *et al* (1988), however, defined E_{prot} as the point of inflection in the reverse scan, labelled as E_{infl} in Fig.2.6. They based this definition upon the work of Nisancioglu and Holtan (1978b), who monitored the current density on specimens of aluminium when the potential sweep was terminated above and below E_{infl}. When terminated above E_{infl}, the current increased continuously and steady state conditions were not reached within a time period of one day. However, if terminated below E_{infl}, the current density attained a constant value within one day at the most. In support of these findings Otani (1988) noted from microstructural observations that when specimens were polarised in a salt solution for one hour at a potential between E_x and E_{infl} that pitting did not initiate or propagate.

The area enclosed by the cyclic polarisation loop is commonly known as the hysteresis area. Also shown in Fig.2.6 is the corrosion potential, E_{corr}, which is the potential at which the anodic and cathodic reactions are equal and opposite during the polarisation experiment, and the effective current is a minimum.

Pourbaix *et al* (1963) proposed from their study on alloy steels that a knowledge of E_{pit} and E_{prot} would enable predictions of the specimen corrosion behaviour to be made as follows. At potentials lower than E_{pit}, no corrosion will occur. However, if the potential exceeds E_{pit}, even for a short time, pits become initiated. Once initiated, pits may continue to propagate at potentials below E_{pit} until the protection potential is reached. Below E_{prot} the pits become repassivated and localised corrosion ceases to occur.

Some authors have found that the method by which the potential is changed during polarisation can affect the shape of the polarisation curve. There are three basic methods by which the potential can be controlled:

1) in a continuous fashion at a constant rate (potentiodynamic)
2) in a stepwise fashion at a constant rate (quasi-stationary)
3) in a stepwise fashion where the potential is changed only when a constant current is established (stationary)

Broli and Holtan (1973) showed that on aluminium, E_{pit} was a function of the scan rate employed, E_{pit} becoming more positive at faster rates. This was observed also by Leckie (1970). Broli and Holtan (1973) noted that the hysteresis area became larger as the scan rate was increased, and no hysteresis loop at all was found by the stationary method. They proposed that electrochemical equilibria was never attained in potentiodynamic and quasi-stationary tests in contrast to the stationary method where equilibria was being achieved at each stage in the test. They concluded, therefore, that the stationary method gave the most accurate value of the

pitting potential and that E_{pit} and E_{prot} were actually the same potential.

Nisancioglu and Holtan (1978a) found that values of E_{pit} on aluminium did not differ greatly between potentiodynamic, quasi-stationary and stationary tests, provided that scan rates were of the order of a few mV/min. They attributed the major cause of difference to an induction time for pit initiation, *i.e.* the specimen may be polarised substantially above E_{pit}, but pitting will not be observed until an induction time has elapsed. E_{pit} therefore becomes more positive with faster rates of scan.

In contradiction to the work of Broli and Holtan (1973), a number of authors have shown that a protection potential does exist and that its value depends upon the extent of propagation of pits and crevices. Wilde (1972) demonstrated that for a 430 stainless steel, E_{prot} was not a unique material property but merely reflected the experimental conditions necessary to repassivate the corrosion pits. By conducting tests at a variety of scan rates, he showed that propagation was greater for the slower scan rates and hence the protection potential was more negative. Similarly, if the current density at which the potential scan was reversed was increased, E_{prot} moved to more negative values because of an increase in the extent of corrosion.

Wilde and Williams (1971) showed that E_{prot} was not a unique value for a given material and proposed that the parameter, E_{pit}-E_{prot}, called the difference potential, was a measure of the extent of attack. In support of their argument they showed that good correlation existed between the weight loss recorded on stainless steel exposed to sea water for 4.5 years and the difference potential from cyclic polarisation tests.

Syrett (1977) interpreted the change of E_{prot} with increased propagation to the solution chemistry changes which occur inside the pit. He suggested that in the early stages of pitting, the corrodent within the pit became increasingly more aggressive in saline environments due to the increasing acidity from chloride ions. As the pit grew it became more difficult to repassivate the walls of the pit and thus E_{prot} was depressed to more active values as the corrosion proceeded.

(b) Potentiostatic Tests

A method which overcomes the problems associated with the induction time in potentiokinetic tests is potentiostatic polarisation. It involves measuring the current density changes with respect to time for a specimen held at a constant potential. As noted by Szklarska-Smialowska and Janik-Czachor (1971) there are essentially two ways in which the experiment may be carried out.

The first method may be used for determining the pitting potential. The specimen is held at a constant potential for a pre-determined period of time, and the current is monitored. A new sample is used for each potential. At $E<E_{pit}$ the current density decreases with time and the metal surface remains passive. However, at $E \geq E_{pit}$ the current density increases because pits have become initiated.

The second method may be used to determine the protection potential. A sample is polarised to a high anodic potential to initiate pitting and then polarised to a potential below E_{pit} and held there for the remainder of the test, a new sample being used for each test. At $E>E_{prot}$ propagation of pits occurs and the current density continues to increase with time. At

$E<E_{prot}$ however, the pits become repassivated and the current density decreases with time.

The potentiostatic technique has been employed by Wood *et al* (1974) on aluminium alloys. They reported the existence of an induction time for pitting. The curves of current density *vs* time were characterised by a flat induction period, during which pitting was not evident upon the surface. This was followed by a sharp rise in the current, where pitting became evident upon the specimen surface.

Nisancioglu and Holtan (1978a) also observed an induction period on aluminium alloys. They suggested that the duration of the test must exceed the expected induction time for pit initiation at the test potential. The induction time was found to be inversely proportional to $E-E_{pit}$ where E is the applied potential ($>E_{pit}$). Therefore, lengthy experiments could result, particularly in the vicinity of E_{pit}.

The potentiostatic method has also been successfully applied for the determination of the pitting potential on aluminium (Bond *et al*, 1966), and the determination of the protection potential on a Fe-16Cr alloy (Szklarska-Smialowska and Janik-Czachor, 1971).

(c) Scratch Technique

The scratch method is essentially a variation of the potentiostatic test, in which the protective film on a specimen held at a constant potential is broken by scratching. The current density is monitored and the time taken for repassivation is recorded. The potential at which repassivation occurs is, however, a source of disagreement. Pessall and Liu (1971)

believed it to represent the pitting potential and stated that under equilibrium conditions the pitting and protection potential were the same. Syrett (1977) on the other hand, believed in the existence of two distinct potentials, E_{pit} and E_{prot}, and regarded the potential obtained from this technique as representing E_{prot}.

Pessall and Liu (1971) successfully applied the technique to stainless steel to determine a value of E_{pit} which was dependent only upon specimen composition and test environment. They found that Fe-Cr and Fe-Cr-Mo alloys gave different E_{pit} characteristics for the scratch technique and the potentiokinetic methods. Only slightly different E_{pit} values were obtained on ternary alloys using the two methods, but the scratch technique gave consistently lower values for the binary alloys. Lizlovs and Bond (1975) found similarly that the scratch method gave more negative values of E_{pit} for some stainless steels, but comparable values for others. Both they and Pessall and Liu (1971) agreed, however, that the scratch technique gave the most accurate value of the pitting potential and that this was independent of surface condition and other minor variations in the test procedure. Syrett (1977) agreed that the scratch method gave more reliable values of the potential, which he considered to be the protection potential. However he noted that the method had the major disadvantage that the passive film was broken by scratching in areas which would not necessarily be favoured as pitting sites. He considered that the potential represented that for the repassivation of scratches rather than pits.

(d) Pit Propagation Rate Method

A test which was suggested by Syrett (1977) as overcoming the shortcomings of both the cyclic polarisation test and the scratch method, is the pit propagation rate (PPR) method. The principles of the test are as follows. A specimen is immersed in the test solution for 1 hour before being taken through an anodic cycle, illustrated in Fig.2.7. The potential is potentiodynamically driven at 36V/hr to a preselected potential between E_{corr} and E_{pit} ($0.25V_{SCE}$ in Fig.2.7). It is held at this potential for 10 minutes to obtain a steady current density in the passive condition, (I_{pass}). The potential is then driven above E_{pit} until a nominal current density of $10mA/cm^2$ is reached, indicating that pits have initiated. The potential is then reduced in a single step to the preselected potential below E_{pit} ($0.25V_{SCE}$) and held for 10 minutes. Hence as no new pits would initiate between E_{pit} and E_{prot}, the current density recorded (I_{total}) would be a measure of the rate of general corrosion plus the rate of pit growth. The potential is decreased once more in a single step to the original corrosion potential so as to repassivate the pits, before scanning to the preselected value again. This ensures that the current has not changed under passive conditions. From these results the current generated by pit growth can be determined from $I_{pit} = I_{total} - I_{pass}$. The pit propagation rate can thus be calculated from I_{pit}/pitted area, the pitted area being determined from microscopic examination. Syrett applied the test to stainless steels and discovered that the protection potentials from this method were considerably more noble than those from cyclic polarisation tests.

2.4 CORROSION OF METAL MATRIX COMPOSITES

Most of the published work on the corrosion of metal matrix composites has focused upon aluminium and aluminium alloys reinforced with graphite, silicon carbide or boron. The following sections discuss the corrosion behaviour of aluminium-based MMC containing these reinforcements and the experimental techniques which have been applied.

2.4.1 CORROSION OF SILICON CARBIDE-REINFORCED ALUMINIUM ALLOYS

The effect of silicon carbide reinforcement on the corrosion properties of aluminium alloys has been investigated by a variety of techniques. Reinforcements in the form of continuous fibres, whiskers or particles have all received attention.

Aylor and Kain (1985) investigated the corrosion behaviour of a 6061 (Al-Si) alloy reinforced with fibres, whiskers and particulate. The whisker and particulate MMC were fabricated by a powder metallurgy route, the blended powders being hot-pressed between 1100 (>99% Al) aluminium surface foils. The fibre-reinforced MMC was produced by the diffusion bonding of plasma-sprayed SiC and 6061 Al foils. Test panels of these materials were exposed to total marine immersion, splash/spray alternate tidal immersion and also marine atmosphere exposures. The test period ranged from 30 to 365 days. They found that gravimetric measurements did not accurately represent the degree of corrosion owing to the build-up of internally entrapped corrosion products which off-set the overall weight loss. Microstuctural analysis of the MMC with SiC particulate showed that the corrosion took the form of pitting and was related initially to the corrosion resistance of the 1100 aluminium surface foils. Once penetration

of the surface foils had occurred (~230 days), corrosion concentrated around the SiC particles. Regarding the SiC whisker MMC, pitting corrosion was concentrated around the whiskers, which Aylor and Kain attributed to crevices at the reinforcement/matrix interface. In the case of the SiC fibre MMC, attack occurred intergranularly in the 6061 Al surface foils and penetration through the surface foils into the composite did not occur during the test.

Aylor and Moran (1985) also observed preferential attack at the reinforcement/matrix interface of a 6061 (Al-Si) alloy reinforced with SiC whiskers. The material was fabricated by powder metallurgy and studied in the as-received and T6 heat-treated conditions. They noted that the morphology and extent of pitting differed between the composite and the corresponding unreinforced alloy, the composite exhibiting a larger number of pits, which were smaller and shallower than those in the corroded alloy. Cyclic polarisation tests showed the composite materials to yield pitting potentials which were more noble than the lowest value of E_{pit} for the alloy. They therefore concluded that the presence of SiC whiskers did not increase the susceptibility of the aluminium surface film to pitting corrosion.

These findings are also consistent with the results of corrosion tests performed by Trzaskoma *et al* (1983) and Trzaskoma (1990) on powder metallurgy produced 6061 (Al-Si) and 5456 (Al-Mg) alloys reinforced with SiC whiskers. They noted that although the pitting potential remained unaffected by the reinforcement, the corrosion morphology was altered and a significantly greater number of pits formed on the composites compared with the corresponding unreinforced alloys. They attributed this to the presence of a greater number of detrimental secondary

intermetallic phases in the composite. In the case of the 5456-based MMC the intermetallics were enriched with chromium and manganese, which were alloying elements present in the alloy, and also iron, which was present as an impurity phase. EDS analysis indicated that pits initiated at these particles.

In contrast to the 6061 and 5456 based materials, Trzaskoma *et al* (1983) discovered that a 2024 (Al-Cu) alloy became more susceptible to pitting on addition of SiC whiskers. The pitting potential obtained from anodic polarisation tests was ~100mV more active for the composite than the alloy.

Paciej and Agarwala (1988) studied the effect of SiC particulate on the corrosion of a 7091 (Al-Zn-Mg) alloy. The composite was manufactured by powder metallurgy and studied in the as-received condition (A), after heat-treatment at 910°F for 1 hour (B), and after heat treatment at 910°F for 2 hours followed by 4 days at room temperature (C). The corrosion tests comprised gravimetry, potentiodynamic polarisation and open circuit potential measurements. They found that corrosion rates calculated from weight loss measurements, were higher for the MMC than for the corresponding unreinforced alloy. The rate for all materials increased rapidly during the first stages of immersion (~3 days), A having the highest corrosion rate, followed by B then C. The rate then declined for all materials over the following 12 days. Steady state corrosion potentials recorded over short immersion times (~3000 seconds) on both composite and alloy systems reflected a similar trend. The initial potentials for the materials were in decreasing order of electronegativity, A < B < alloy < C. They observed that these initial negative potentials reflected the dissolution of active phases or intermetallics in the matrix material. After

2000 seconds the corrosion potentials became more stable and the alloy was found to have the most active potential, followed by C, B and finally A. Microstructural examination showed that the pits had formed around the SiC particles, which Paciej and Agarwala noted could possibly be due to the high dislocation density at the particulate/matrix interface providing an area of high residual stress. Hence these regions were likely sites for crevice or pit formation. The pitting potentials from potentiodynamic polarisation tests were most active for the composites in the order A < B < C < alloy , which is in close agreement with the results of weight loss tests.

Paciej and Agarwala (1985) investigated also the corrosion behaviour of a 7091 (Al-Zn-Mg) alloy reinforced with SiC whiskers, fabricated by a powder metallurgy process and noted that its corrosion resistance was worse due to inhomogeneity factors. Hence, they concluded that processing variables as well as heat treatment played an important role in the corrosion behaviour of MMC.

Otani *et al* (1988 & 1989) conducted an investigation into the corrosion behaviour of an Al-Si-Mg alloy and commercial purity aluminium, both of which were reinforced with continuous SiC (Nicalon) fibres. The composites were fabricated by the liquid metal infiltration process. In addition to weight loss measurements, they adopted a double cyclic polarisation (DCP) technique *i.e.* two cyclic polarisation curves performed in succession. Otani (1988) reported this to be an improved technique over the traditional cyclic polarisation method as he found that for a variety of materials, particularly MMC, the pitting potential was ill-defined by the first polarisation cycle and no inflection corresponding to E_{pit} could be found. If, however, a second polarisation cycle was performed immediately

following the first, the pitting potential was well-defined on the second cycle. It was found that weight loss tests on the composites were unsuccessful due to the entrappment of internal corrosion products. This made assessment of the DCP technique difficult. Regarding the unreinforced alloys, however, the weight loss data from gravimetric tests gave good correlation with the hysteresis area and difference potentials (which both represent the extent of attack), obtained from the DCP test. It was noted that the difference potential test could still be useful in placing the materials into a ranking order. Regarding the microstructures, the presence of SiC fibres was found to play a secondary role in the corrosion process by acting as a barrier to corrosion pit growth or by altering the microstructure of the metal. The major influence of the fibres was found to lie within the metal matrix; large amounts of second phases containing iron were found in the commercial purity aluminium, such as $FeAl_6$, and these produced a strong microgalvanic corrosion effect. In the case of the Al-Si-Mg based MMC, the presence of the silicon meant that a $FeSiAl_5$ intermetallic was formed. This was less severely attacked and apparently appeared to inhibit corrosion propagation. In this MMC, the pits formed at regions of silicon segregation close to the fibres and propagated along the fibres due to the higher concentration of silicon along the fibre/matrix interface.

2.4.2 CORROSION OF CARBON-REINFORCED ALUMINIUM ALLOYS

There is a consensus of opinion among authors that the incorporation of graphite fibres into aluminium alloys has a detrimental affect upon the corrosion behaviour of the alloys.

Aylor and Kain (1985) investigated the corrosion resistance of a 6061 (Al-Si) alloy, both unreinforced and reinforced with graphite fibres. The composite was fabricated by hot-press diffusion bonding of graphite/6061Al wires between aluminium-surface foils. They subjected test panels, which were in the as-received, anodised and nickel-coated conditions, to marine environments and then made microstructural observations. After 30 days, they noted that the uncoated MMC had suffered pitting attack, which was similar to that of the unreinforced control alloy, the corrosion proceeding intergranularly through the surface foils. The nickel-coated panels showed more severe corrosion, indicating that the coating accelerated the attack rather than providing a barrier. This they attributed to flaws in the coating and concluded that longer immersion times of the uncoated MMC would result in attack similar to that found on the nickel-coated panels. The nickel-coated panel showed penetration of the surface foils and thereafter galvanic interaction between the fibres and matrix. This type of attack would lead to a build-up of internal corrosion products and eventual degradation of the composite. The anodised panels showed that despite having been attacked, after 180 days the coating still provided good protection for the composite. Overall the control panels exhibited greater corrosion resistance than the composite panels.

Aylor *et al* (1984) reported the results of weight loss measurements made on graphite fibre-reinforced 6061 (Al-Si) alloy. They found that the results did not accurately reflect the extent of corrosion of the MMC material due firstly to the attack being localised rather than uniform and secondly due to the build-up of internal corrosion products.

Evans and Braddick (1971) also observed that corrosion could penetrate well below the surface, causing swelling and degradation of a carbon-reinforced aluminium MMC. The corrosion occurred by intergranular attack in regions where the matrix was supposedly pure aluminium. They attributed this effect to the dissolution of impurity phases (probably carbon) in the aluminium during heat-treatment. Weight loss measurements were also made and it was noted that the corrosion rates were considerably greater than those previously found elsewhere for a chopped carbon fibre-reinforced aluminium MMC. They attributed this to the presence of an uninterrupted electrically conducting path formed by the continuous fibres in their composite.

Marine exposure, corrosion potential measurements and cyclic polarisation tests were applied by Aylor and Moran (1985) to a graphite-reinforced 6061 (Al-Si) alloy, produced by diffusion bonding of graphite/aluminium wires and 6061 aluminium surface foils. After 1 to 4 months exposure in filtered sea water, the MMC test panels exhibited severe attack. The surface foils had blistered thereby exposing the composite to the environment and exemplifying the accelerated corrosion which follows penetration of the surface foils. This demonstrated that the corrosion resistance of the material was dependent upon the integrity of the surface foils. The average corrosion potential recorded after 30 days immersion in marine water was more electronegative for the MMC than for the corresponding alloy, indicating that the graphite fibres did not polarise the composite in the electropositive direction as might be expected under normal galvanic conditions. In addition, values of the pitting potential recorded for the graphite composite were significantly more negative than values of E_{pit} found for a SiC composite based on the same 6061 alloy. Aylor and Moran proposed that this was due to the

passive film on the graphite-reinforced 6061 alloy being more susceptible to pitting attack. They also suggested, as did Evans and Braddick (1971), that carbon diffused from the fibres into the matrix and consequently formed aluminium carbides at the fibre/matrix interface. Thus the interface was rendered more susceptible to breakdown, and the corrosion potential would be forced to more negative values, as they observed, due to the active dissolution of these sites.

Vassilaros *et al* (1980) adopted a rather different approach when characterising the marine performance of graphite-reinforced 6061 (Al-Si) alloy. The material was assessed by the loss of strength due to corrosion. The material, which was fabricated by diffusion bonding of TiB-coated graphite wires and 6061 aluminium foils, was subjected to mechanical property tests both prior to and following corrosion testing. The corrosion tests involved immersion in natural flowing sea water, tidal immersion and exposure to a marine environment. They found that providing there was no visible evidence of corrosion, the strength of the composite was not affected. The average tensile strength fell in the band 550-670 MPa, which compared favourably with results for unexposed specimens which had strengths of ~10-15% higher. They found, however that for specimens which exhibited visible corrosion (generally those exposed to flowing sea water), there was a substantial decrease in strength to <200MPa. In agreement with Aylor and Moran (1985), they found that the corrosion resistance was dependant upon the integrity of the surface foils; once these were penetrated, the attack occurred at an accelerated rate at the fibre/matrix interface.

Otani *et al* (1989) performed double cyclic polarisation tests on a carbon-reinforced Al-Si-Mg alloy. They discovered that whilst corrosion data from

the DCP test suggested that this material corroded less than the same alloy reinforced with a SiC fibre, initial microstructural observations showed the reverse to be true. However, upon closer examination, they found that much of the microstructural damage was in the form of extensive cracking caused by mechanical stresses generated during the formation of internal corrosion products. They concluded that the cracking, which occurred at the fibre/matrix interface was due to galvanic corrosion caused by the electrochemical potential difference between the aluminium and carbon.

Friend *et al* (1990) applied potentiodynamic polarisation to 99.99% aluminium reinforced with high modulus carbon and high strength carbon fibres. The results showed that the two composites had almost the same value of the pitting potential and also that the breakdown to pitting attack occurred at lower potentials for the composite than for the aluminium. They observed that enhanced attack occurred within the MMC compared to the aluminium, and this they attributed to galvanic corrosion caused by the electrochemical difference between the carbon fibres and the aluminium matrix.

2.4.3 CORROSION OF BORON-REINFORCED ALUMINIUM

An investigation into the corrosion susceptibility of boron-reinforced aluminium was conducted by Evans and Braddick (1971). From microstructural examinations they observed that a fairly uniform dissolution of aluminium had occurred across the surface, with some instances of pitting. Severe attack was found, however, at the fibre/matrix interface, which they believed to be a consequence of the formation of aluminium boride at the interface. This formed during the hot pressing

process employed during manufacture. Examination of the boron fibres suggested that some attack of the fibres themselves may have occurred, but they noted that this may also have been a consequence of damage incurred during manufacture.

Sedriks *et al* (1971) offered an alternative explanation for the interfacial corrosion. They studied the corrosion behaviour of a boron fibre-reinforced 2024 (Al-Cu) alloy by measuring the loss of strength as a result of corrosion. It was discovered that the loss of strength of the composite was greater than that of the unreinforced alloy. This was due to a larger reduction in load bearing area as a result of localised corrosion. The attack occurred preferentially at the fibre/matrix interfaces and at the diffusion bonds between the metal foils. This behaviour they attributed to an increase in the number of anodic sites at the interfaces due to the presence of crevices.

A further explanation for preferential corrosion at the fibre/matrix interface was put forward by Pohlman (1978), who studied the environmental corrosion of boron-reinforced 2024 (Al-Cu) and 6061 (Al-Si) alloys. They suggested that the enhanced attack, which they found in the interfacial regions could be a result of either (i) a lower corrosion resistance of the aluminium boride which they found at the filament surface (as also suggested by Evans and Braddick, 1971), or (ii) a galvanic action between fibre and matrix, or (iii) a combination of (i) and (ii).

Batrakov *et al* (1979) performed anodic polarisation tests on aluminium alloys reinforced with steel or carbon in addition to boron-reinforced aluminium alloys. From a comparison of polarisation curves they suggested that the corrosion behaviour of the composite materials was

limited by cathodic processes occurring on the surface of the reinforcements, due to the fibres having a more positive potential and acting as the cathode in a galvanic cell. It followed that the corrosion of the matrix depended upon the nature and relative area of the reinforcement; the smaller the area of the reinforcement, the lower the cathodic current and consequently the corrosion of the matrix would be reduced.

2.5 AIMS OF THE PRESENT INVESTIGATION

It is apparent from the preceeding literature survey that the corrosion behaviour of MMC is by no means well understood and that the limited number of corrosion tests applied to these materials to date have only met with varying degrees of success. Thus the present study focuses attention particularly upon:

(a) establishing a suitable corrosion test by which the susceptibility of MMC to corrosion may be assessed, and

(b) elucidating the mechanism of corrosion in aluminium-based MMC.

The experimental work investigates corrosion characteristics in de-aerated 3.5wt% NaCl solution of aluminium alloys containing a number of ceramic reinforcements which have a range of electrical conductivities. The reinforcements include continuous carbon and Nicalon fibres (conducting and semi-conducting respectively), short alumina (Saffil) fibres (non-conducting) and silicon carbide particulate (semi-conducting). The matrix metals consist of pure aluminium, an Al-7Si-0.5Mg alloy, well known for its good casting characteristics, and a Al-4Cu-1.5Mg alloy with

the potential for precipitation hardening. Composites were fabricated by liquid metal infiltration (LMI), squeeze casting or powder metallurgy.

The corrosion studies have been carried out using simple immersion of the samples in the corrosive solution and employing accelerated corrosion test methods in which the specimens were forced to corrode by an applied potential. In particular, the double cyclic polarisation (DCP) test has been used for predicting the susceptibility of MMC to pitting attack.

Examination of the corroded surfaces and sections through the corroded material has been carried out using a variety of microstructural techniques. Optical and scanning electron microscopy (SEM) have been applied to the characterisation of the sites of corrosion attack. This has been coupled with energy-dispersive spectrometry (EDS) of the X-ray emission in order to obtain related chemical composition data. Transmission electron microscopy (TEM) has been used for the study of much finer microstructural details such as the nature of the fibre/matrix interface. In addition to elucidating the role of the reinforcement and of the matrix composition, the studies have also permitted the effect of fabrication route to be explored.

CHAPTER 3

EXPERIMENTAL DETAILS

3.1 MATERIALS

3.1.1 MATRIX METALS

The metal matrix composites selected for investigation were based upon three matrix metals:

(i) super pure aluminium,
(ii) aluminium - 7wt% silicon - 0.5wt% magnesium alloy, designated 357, a popular casting alloy owing to its high fluidity in the molten state, and
(iii) aluminium - 4wt% copper - 1.5wt% magnesium, a precipitation hardening alloy, designated 2124.

The matrix metals were studied in the unreinforced condition to provide a comparison for the composite materials. In the case of the super purity aluminium matrix, commercial purity aluminium was studied in the unreinforced condition as a control. The chemical compositions of the matrices are given in Table 3.1.

Some experiments designed to evaluate the performance of the corrosion test apparatus were made using a 430 stainless steel, the chemical composition of which is also given in Table 3.1.

3.1.2 REINFORCEMENTS

The reinforcements studied included continuous and short fibres and particulate. The continuous fibres were carbon and Nicalon, a fibre composed essentially of silicon carbide, the short fibre was Saffil, a δ-

alumina fibre, and the particulate reinforcement was silicon carbide. Nicalon and Saffil are trade names for products of Nippon Carbone Co. Ltd and ICI plc, respectively. Data relating to the reinforcements are given in Table 3.2.

The carbon fibre was produced by the pyrolysis of a polyacrylonitrile (PAN) precursor, the final product consisting of multifilament tows with fibres being ~8μm in diameter.

The Nicalon fibre was developed by Yajima *et al* (1978) as a silicon carbide fibre. The production of the fibre involves a series of complicated operations, illustrated schematically in Fig.3.1 (from Anderson and Warren, 1984) and ends with the pyrolysis of a polycarbosilane fibre to form what was originally thought to be a silicon carbide fibre, although it has been more recently shown (Porte and Sartre, 1989) to consist of silicon carbide together with carbon and an intermediate silicon oxycarbide phase SiO_xC_y. The molar ratios of the components give;

$$SiC: SiO_xC_y:C: SiO_2 = 1: 0.5: 0.75\pm0.25: 0.08.$$

The δ-alumina fibres were produced by a spinning process which controls the fibre diameter within tight limits around a mean value of 3μm. The mean length of the fibres is ~100μm. A fine-grained microstructure was developed by the addition of ~4% silica. This is effective in controlling the level of porosity and acting as a crystal growth inhibitor during the heat-treatment. The δ-alumina fibres were then made into a porous, block-like preform by mixing the fibres in a slurry containing an in-organic binder and a fugitive organic binder, the latter of which is burnt off during firing.

3.1.3 METAL MATRIX COMPOSITES

The corrosion characteristics of seven metal matrix composites were investigated. The composites were fabricated by a variety of routes which included, squeeze casting (made at the Royal Military College of Science, Shrivenham, Wiltshire), liquid metal infiltration (supplied by the DRA (Maritime Division) Admiralty Research Establishment, Holton Heath, Dorset, and Cray Advanced Materials Systems, Yeovil) and powder metallurgy (supplied by BP). Table 3.3 is a summary of the MMC systems, their method of manufacture and the form in which the composite was received.

3.1.4 FABRICATION OF MMC BY SQUEEZE CASTING

The composites listed in Table 3.3 which were fabricated by squeeze casting, were manufactured using equipment at the Royal Military College of Science, Shrivenham, Wiltshire, with their kind permission. The procedure followed will now be described.

Firstly a fibre preform of unidirectional carbon fibres was constructed by a filament winding process. Tows containing ~2000 carbon fibres were wound by hand around two plates of steel placed back to back, the edges of the steel being bent to prevent the fibres sliding off, Fig.3.2(a). Steel caps were placed over each side of the preform, as illustrated in Fig.3.2(b), and then the whole assembly clamped between steel plates, see Fig.3.2(c), to prevent the fibres from floating during casting. Finally the fibres were de-sized in a furnace at a temperature of ~800°C for 15 minutes.

Prior to casting the fibre preform was heated to 750°C and placed in the die, which was also heated to ~ 370°C. The metal (1kg mass), was heated

to 1000°C in the crucible, before being poured from the bottom of the crucible via a launder into the die. A dovetail ram, which was located directly above the die, was lowered onto the molten cast, until a pressure of ~30MPa was attained. This was maintained for 1 minute. The pressure was then allowed to fall back to zero. The die and cast were cooled to ~250°C before the ram was raised, bringing with it the cast which was interlocked in the dovetail. After further cooling the composite could be cut from the cast.

3.2 PREPARATION OF TEST SPECIMENS

3.2.1 UNREINFORCED MATRIX METALS

Samples of unreinforced metals were cut on a Struers Discotom cutting machine, fitted with a hard-bonded abrasive cutting wheel. An Aquicut cutting fluid acted as a lubricant and coolant. Specimens for corrosion tests were required to be either unmounted or mounted in resin. Those for mounting were cut into ~10x10x5mm^3 blocks and mounted in Struers Epofix cold-setting resin, whilst the unmounted specimens were larger, typically 20x15x5mm^3.

A high quality metallographic finish was required for microstructural analysis. To achieve this, specimens were firstly ground until flat on 200 grit silicon carbide paper on a Beuhler Motopol 12 machine. This was followed by grinding on a perforated Texmet* cloth using 6μm diamond slurry and then polishing on a Metlap 1* cloth and a 1μm diamond slurry, (the latter 1μm stage was omitted in the case of aluminium). The final stage involved polishing on a Mastertex* cloth with colloidal silica. After

* Beuhler UK Ltd.

washing with Teepol detergent, the samples were rinsed with distilled water, dried and stored in a dessicator until required.

Unmounted specimens were ground on all faces using successively finer grades of silicon carbide paper, down to 500 grit. All edges and corners were rounded to prevent charge concentration effects during the corrosion experiments. A 3mm hole drilled towards the top of the specimen enabled it to be suspended in the electrolyte, the hole being masked off with Lacomit varnish to prevent charge concentration effects.

3.2.2 METAL MATRIX COMPOSITES

Specimens of MMC were cut from the bulk using a Struers Acutom precision cutting machine fitted with a Bakelite bonded abrasive wheel. An Aquicut cutting fluid was once again used for lubrication and cooling. Composites containing unidirectional fibres were cut to expose transverse sections whilst the two-directional material (carbon fibre-reinforced 357 alloy) was cut to expose fibres in both directions simultaneously. The Saffil reinforced material was not cut to any particular fibre orientation, and the particulate reinforced specimens were cut to expose surfaces containing the hot-rolling direction.

Mounted MMC specimens were once again prepared using a Beuhler Motopol 12 machine. They were firstly ground using a Metlap 10* grinding wheel with 45μm diamond slurry until the specimens were flat. This was followed by two stages on Perforated Texmet cloth using 15μm diamond and then 6μm diamond slurries. A Metlap 1 with 1μm diamond slurry and finally a Mastertex cloth with colloidal silica completed the

metallographic preparation. Samples were then cleaned, rinsed and stored in a dessicator.

Unmounted MMC specimens were prepared in the same way as the unmounted metals described in the previous section.

3.2.3 TRANSMISSION ELECTRON MICROSCOPY SPECIMENS

Composite specimens for examination in the transmission electron microscope (TEM) were prepared by cutting thin (~0.2mm) slices from the bulk composite. Discs of 3mm diameter were prepared from the wafers using a coring drill and the discs ground on silicon carbide paper to a thickness of 100μm. The central thickness of a disc was further reduced to ~25μm by mechanical dimpling each face of the disc in turn with a VCR model 500 dimpling machine. This was followed by ion beam thinning in a Gatan Duomill for several hours at 5KV and a beam angle of 15° until perforation occurred. The region around the perforation was then thin enough for TEM studies.

3.2.4 ALUMINIUM SINGLE CRYSTAL SPECIMENS

Single crystals of aluminium were cut along specific crystal planes for assessment of the polarisation test method. The back-reflection Laue method was employed to orientate the crystals prior to cutting.

The single crystal specimen was mounted on a goniometer which allowed three mutually perpendicular axes of rotation. The X-ray beam was switched on and an X-ray diffraction pattern was produced consisting of an array of spots characteristic of the orientation of the crystal. The specimen was then orientated by means of the goniometer until a spot

pattern to the desired orientation was achieved. Without disturbing the crystal, the goniometer was removed from its track and transferred to a similar track on a cutting device. The crystal was then cut to the required orientation whilst still mounted on the holder.

3.3 CORROSION TESTING

3.3.1 CORROSION TEST ENVIRONMENT

A 3.5wt% NaCl solution, prepared from reagent grade NaCl and distilled water, was used for all corrosion tests, this solution being close to the concentration of sea water. The solution was maintained at a constant temperature of 25±0.5°C and de-aerated for all tests by bubbling oxygen-free nitrogen gas through the solution for 1 hour prior to and constantly during the test. Measurement of the residual oxygen content with an oxygen meter after de-aerating for 1 hour, showed the solution to be fully de-aerated within the sensitivity of the meter (0.1ppm). The reasons for de-aeration, as noted by Syrret (1976), are essentially;

(a) to enable the anodic characteristics of a metal to be determined over a wider potential range in the absence of oxygen, and

(b) to remove the effect that the dissolved oxygen may have on the cathodic reactions occurring on the metal surface.

3.3.2 GRAVIMETRY

For determining the weight change of a material with time, an unmounted specimen was suspended in solution for increasing lengths of time ranging from 1 day to 3 weeks. The surface area of the specimen and its mass was recorded prior to immersion. After immersion the specimen

was scrubbed with a soft bristle brush and immersed in nitric acid for 10 minutes in an ultrasonic bath to remove all corrosion product. The specimen was then weighed. The cleaning procedure was repeated until a constant weight was achieved, indicating that all corrosion product had been removed. The mass loss was then calculated with respect to the exposed area.

3.3.3 OPEN CIRCUIT POTENTIAL TESTS

The open circuit potential of a freely corroding specimen was monitored over a 3 week period. A mounted specimen was fitted into the working electrode holder, Fig.3.3. This consisted of a cap, stem, screw and holder fabricated from PTFE containing rods and a plate of copper to provide an electrically conducting path to the specimen. The assembly is based upon the design of Otani *et al* (1988) but incorporated improved sealing arrangements between the specimen cap and specimen in order to prevent water ingress. It involved machining away a small part of the cap so as to create a lip at the edge of the opening which exposed the specimen, Fig.3.3, and a small amount of silicone rubber sealant introduced between the cap and specimen. When assembled, a $1cm^2$ circular area of the specimen was exposed to the solution. When, however, thin mounted sections of the material were used, exposure of some of the resin mount and the interface between the specimen and resin reduced the area of the sections to ~$30mm^2$. Lacomit varnish was used to seal specimen/mount interfaces from the solution in order to avoid the possibilities of crevice corrosion being generated.

The working electrode, containing the specimen, was immersed in the solution and the potential monitored using a saturated calomel electrode

(SCE). All data were recorded as a function of time by a data logger, the potential data sampling period being varied as the test progressed. Starting at 1 minute for the first hour, the sampling time was increased to 10 minutes for the next 3 hours. Measurement intervals were then set at 30 minutes for the remainder of the first day, hourly for the second day and finally 2 hourly until the test reached completion. After each data interval, the data was transferred to floppy disc.

3.3.4 POTENTIODYNAMIC POLARISATION

(a) Apparatus

The equipment used for polarisation tests is illustrated in Fig.3.4. It consisted of an ACM RS-232 Computerstat (Applied Corrosion Monitoring Ltd) which was controlled by an Amstrad PC-1512 computer. The ACM-232 Computerstat was a potentiostat which could be controlled via a computer to measure current-potential or current-time relationships for a variety of materials. The results were plotted out during the course of the test and stored on floppy disc. The choice of sampling interval (potential and current) was dependant upon the method of polarisation since it is a function of the memory of the computer. Typically data were sampled at 5mV intervals during potentiodynamic polarisation experiments.

A coaxial glass cell was used for all polarisation studies, Fig.3.5, which consisted of three compartments. The outer jacket contained water at a constant temperature which was continually circulated from a water bath. This maintained the test solution, contained in the middle and inner compartments, at a constant temperature throughout the test. The middle compartment contained the test solution and also a glass frit, through

which the nitrogen was bubbled to minimise turbulence in the inner compartment The inner compartment, also filled with test solution, contained a working electrode, a counter electrode and a standard reference electrode. Holes in the walls of the inner compartment allowed interchange of the solution with the middle compartment. Fig.3.6 shows the polarisation cell fitted with the three electrodes.

The same working electrode assembly as adopted for open circuit potential studies, section 3.3.3, was used.

A reference electrode, a saturated calomel electrode (SCE), was included to provide a stable reference potential against which the potential of the working electrode could be measured. All potentials reported in this investigation were recorded with reference to the SCE which has a potential of +242mV (with respect to the standard hydrogen electrode, SHE). Some experiments were conducted using the Luggin capilliary technique as described by McGill and McEnaney (1978). The method is useful for avoiding errors caused by contamination of the test solution with chloride ions from the reference electrode and by the uncompensated solution resistance. However, the results obtained with and without the Luggin technique were almost identical, probably because the high concentration of ions present in the solution provided good conductivity and off-set any contamination. Most of the tests carried out did not, therefore, include the Luggin probe.

The auxilliary electrode, a platinum mesh of ~30mm^2, was employed to supply the current required by the working electrode response of the cell.

(b) Anodic Polarisation

Preliminary anodic polarisation studies were conducted in accordance with the ASTM G5-78 (1978) standard recommended practice to assess the performance of the cell. This involved producing anodic polarisation curves for 430 stainless steel immersed in de-aerated 1.0N H_2SO_4 at 30°C. The potential scan, which commenced at ~50mV below the natural corrosion potential, was swept at a scan rate of 10mV/min up to ~1600mV. Graphs of the potential *vs* current density were recorded for experiments both with and without the Luggin probe.

(c) Double Cyclic Polarisation

The double cycle polarisation (DCP) test was employed for determining pitting, protection and corrosion potentials for all alloys and MMC. The limits of each potential cycle were (i) a potential of 500mV more negative than the free corrosion potential on immersion for the start of each cycle and (ii) a maximum current density of 5mAcm^{-2} for the reversal of potential at the end of each forward scan. The specimen was immersed in the solution for ~10 minutes prior to polarisation, by which time a steady potential had been achieved. Each test was carried out at least three times and the mean values of the pitting, protection and corrosion potentials and hysteresis area calculated. The experimental scatter for each potential was also recorded from the tests.

Preliminary tests were conducted on silicon carbide-reinforced 2124 alloy to characterise the DCP curve. In addition, some experiments were carried out on single crystals of aluminium of different crystallographic orientations to assess the sensitivity of the DCP technique.

Some tests were conducted on materials based upon the 357 alloy at the slow scan rate of 2mV/min, to investigate the effect of scan rate upon the DCP curve, but a scan rate of 20mV/min was mostly adopted.

3.3.5 POTENTIOSTATIC POLARISATION

Potentiostatic polarisation tests were carried out on silicon carbide-reinforced 2124 alloy to investigate the definition of a protection potential. The equipment employed for these experiments was the same as that for the preceeding polarisation tests. The experiment involved holding the specimen at a predetermined potential and monitoring the current response over a period of 3 hours. The potentials at which the specimen was polarised were selected so as to explore in more detail the electrochemical characteristics in the region of the protection potential from the DCP curve.

3.3.6 GALVANIC COUPLES

Galvanic tests were performed between unreinforced metal and bare fibres in order to determine the galvanic current flowing between them and hence the corrosion rate of the metal in such a couple. The mounted metal specimen was placed in the working electrode assembly and immersed in the solution (which was not de-aerated in this case). Tows of carbon or Nicalon fibres, which had been desized by immersion in dilute HNO_3 for ~10 minutes, were stuck down onto copper plates using silver paint in order to provide a conducting path to the fibres. The fibres were then immersed in the solution together with the working electrode assembly. After allowing the system to stabilise (taking ~10 minutes), the galvanic current flowing between the metal and fibres was monitored over

a 2 hour period using a computer-controlled zero resistance ammeter and the results stored on floppy disc.

3.4 MICROSTRUCTURAL STUDY

3.4.1 OPTICAL MICROSCOPY

Metallographically prepared specimens were studied using a Zeiss ICM 405 optical microscope both before and after corrosion testing. The optical microscope was also used to investigate the corrosion morphology of specimens which had been corroded for times ranging from a few hours to 3 weeks.

3.4.2 QUANTITATIVE MICROSCOPY

The volume fractions of fibres present in the MMC were measured by image analysis using a Joyce-Loebl Magiscan 2A coupled to a Zeiss Ultraphot microscope. The principal stages of image analysis are as follows.

The image formed by the microscope, of polished and mounted specimens is collected by a real time video camera. The analogue camera image is then digitised and treated as a set of points (pixels), arranged in a matrix of 512 x 512 square pixels. Each pixel is assigned one of 64 grey levels from black to white. The grey image may be manipulated in a number of ways, the "edge operator" being the only one used in this study. This defined more clearly the edge of an object by finding regions of rapid change of grey level, for example a fibre edge, and sharpening this region

whilst smoothing the others, thereby improving the contrast between the two areas.

The regions of interest within the image were separated from the background by a process of segmentation giving a binary image of white regions and black background. This was achieved by setting a threshold level, where all levels of grey below a selected one were treated as white and all above the level were treated as black. In the case of a composite, the threshold was set so that the fibres appeared black and the matrix regions and second phases were white.

The final stage of image analysis, object detection, involved counting all the pixels which appeared black in the image.

3.4.3 SCANNING ELECTRON MICROSCOPY

The scanning electron microscope (SEM), Fig.3.7, provided an excellent means for studying the corrosion of MMC owing to its greater depth of field and greater resolution (~5nm) when compared with the optical microscope.

The principle of the technique is as follows. An electron gun produces a monochromatic beam of electrons with the energy range 5KV and 40KV and condenser lenses demagnify the beam into a finely focused spot (~5nm) on the specimen. When the electrons strike the surface, various interaction processes occur as summarised in Fig.3.8. The secondary and back-scattered electrons are collected to form a picture upon a cathode ray tube (CRT), which gives point-to-point correspondence with the area of specimen scanned by the electron beam.

A JEOL T330 and a JEOL 35C scanning electron microscope were used in this investigation. The latter was fitted with an energy-dispersive spectrometer (EDS) which was used to determine the chemical composition of microstructural features. The principle of operation of an EDS system will be described in section 3.4.5.

3.4.4 TRANSMISSION ELECTRON MICROSCOPY

The transmission electron microscope (TEM), Fig.3.9, allows the resolution of microstructural details <1nm in size. The TEM used in this investigation was a JEOL 2000FX instrument to which was attached a LINK high-angle thin window EDS detector and AN1000 analyser. The operation of the TEM is as follows.

A beam of electrons is emitted from the electron gun at an accelerating voltage of up to 200keV. Below the gun are condensor lenses which control the diameter of the electron beam as it hits the specimen, which is located in a chamber directly beneath the condensor lenses. The specimen holder can be moved in two directions in the horizontal plane and it can also be tilted to an angle of up to 45° in order that different features of the specimen can be brought into view. The objective lens, which is situated below the specimen chamber, forms an intermediate image which, by controlling the current, is focused upon a plane containing a set of apertures. These apertures, known as diffraction apertures, enable the area of the field of view to be selected for the purposes of forming an electron diffraction pattern. The intermediate image is viewed on a fluorescent screen after passing through several projector lenses which enlarge the image to its final magnification.

The TEM can provide electron diffraction patterns, from which information may be obtained regarding the crystallographic structure of the material under investigation. A schematic illustration of the formation of a diffraction pattern is given in Fig.3.10. When the electron beam strikes the specimen, some of the electrons are transmitted without interaction, whilst others are diffracted. The electrons which have been diffracted through the same angle are refracted by the objective lens and brought to a point in the back focal plane, as illustrated in Fig.3.10. This forms the diffraction pattern.

From the diffraction pattern, the spacing of lattice planes within the crystal may be found as follows. Fig.3.11 illustrates a beam of electrons of wavelength λ, which have been diffracted through an angle θ, by a crystal whose interplanar spacing is d. According to Bragg's Law:

$$n\lambda = 2d\sin\theta$$

and, as θ is very small, this approximates to:

$$n\lambda \sim 2d\theta$$

From Fig.3.11 we can see that the angle through which the electrons are diffracted, is related to the distance between the spot from the central spot on the diffraction pattern, r, and the distance between the specimen and the pattern, L, (otherwise known as the camera length). Thus

$$2\theta \sim \frac{r}{L}$$

$$n\lambda = \frac{dr}{L}$$

$$\therefore\ d = \frac{n\lambda L}{r}$$

Hence the interplanar spacing may be found from measurement of r from the diffraction pattern. Having obtained the interplanar spacings, the material may be identified by reference to ASTM charts, which lists the

d-spacings of many materials. For a cubic lattice the relationship is as follows, where a is the unit cell parameter and h,k and l are the indices of the diffracting plane;

$$d_{hkl} = \frac{a}{\sqrt{(h^2 + k^2 + l^2)}}$$

Having indexed the diffraction pattern, the zone axis [uvw] is defined by the vector product of two different diffracting planes, $(h_1k_1l_1)$ and $(h_2k_2l_2)$;

$$[uvw] = (h_1k_1l_1) \wedge (h_2k_2l_2)$$

3.4.5 ELECTRON-PROBE MICROANALYSIS

When a specimen is bombarded with high energy electrons a spectrum of X-rays are produced which consists of background radiation and characteristic X-ray emissions. Each element present will emit X-rays of a particular ("characteristic") energy and measurement of these X-ray energies will allow the elements present to be identified. Furthermore, the intensity of the X-ray energies gives a measure of the amount of element present. This X-ray spectrochemical technique is referred to as electron-probe microanalysis and there are two distinct experimental techniques for analysing the spectra. These are known as energy-dispersive spectrometry (EDS) and wavelength-dispersive spectrometry (WDS). With EDS, the X-rays are detected with a Si(Li) semiconductor held at liquid nitrogen temperature. A thin window is positioned in front of the detector in standard EDS systems, to protect the device from surface contamination. The detector used in this study could detect elements down to boron (atomic number 5) as it had an ultra-thin plastic window.

Within the semiconductor junction, electron-hole pairs are generated, the number of pairs being proportional to the X-ray energy. The total charge is collected, amplified and the pulses separated by a multi-channel analyser according to their amplitude (energy). The resulting spectrum, an example of which is given in Fig.3.12, may be displayed on a screen, stored on a magnetic disc or printed out as a hard copy. EDS systems were employed in this study to establish the composition of second phases and other microstructural features.

WDS has a number of advantages over EDS in that it is more sensitive to light element detection and it has improved energy resolution and element detection sensitivity. Generally, EDS is more suitable for quantitative analysis of chemical compositions.

A WDS system uses a crystal of known interplanar spacing to diffract the X-rays emitted from a specimen. Measurement of the diffraction angle allows the X-ray wavelength, λ, to be calculated by Bragg's law:

$$n\lambda = 2d\sin\theta$$

where "d" is the known interplanar spacing of the analysing crystal. The spectrometer can be set at the appropriate angle to receive X-rays from a selected element and these are then be detected by a gas proportional counter and the intensity measured.

A JEOL 8000S superprobe instrument fitted with four WDS systems was used to determine the thickness of the oxide film on corroded specimens by the following technique.

3.4.6 MEASUREMENT OF OXIDE FILM THICKNESS

Although the measurement of oxide film thickness proved to be a minor part of the research on corroded materials, the method of measurement used, together with the results obtained, were considered to be of sufficient general interest to be reported in some detail. It involves the use of electron-probe microanalysis to analyse chemically the surface regions of the corroded material, and then to apply a correction routine to convert the measured X-ray intensities into film thickness measurements. A description of the underlying principles now follows.

When a specimen is bombarded with electrons in the range 5 to 50kV, X-rays are produced from a volume of approximately $1\mu m^3$ in the specimen. The manner in which the X-ray intensity varies with depth in the target is a function of its atomic number and the accelerating voltage of the electron beam. It may be represented by a distribution known as a $\phi(\rho z)$ curve, see Fig.3.13. Various analytical formulae have been developed to describe the $\phi(\rho z)$ function, but the equations, in general, are fairly complicated. Love and Scott (1978), however, adopted a simple approach which was first proposed by Bishop (1974). They assumed that the X-ray distribution $\phi(\rho z)$ with mass depth ρz was a rectangular function, see Fig.3.14, where a constant $\phi(\rho z)$ was assumed until a value of twice the mean depth of X-ray generation ($\overline{\rho z}$) was reached whereupon it fell to zero. The term $\overline{\rho z}$ is defined as follows;

$$\overline{\rho z} = \frac{\int_0^\infty \phi(\rho z).\rho z.d(\rho z)}{\int_0^\infty \phi(\rho z).d(\rho z)}$$

Love and Scott showed that the rectangular function could be used in quantitaive microanalysis, provided that an accurate expression for ρz was available. The total intensity of generated X-rays is thus given by $\phi(0).2\rho z$, where f(0) is the surface ionisation function. An X-ray absorption term (χ) must be included to take into account the X-rays which are absorbed as they leave the specimen and thus the emitted X-ray intensity is;

$$\int_0^{2\rho z} \phi(0).\exp(-\chi.\rho z).d(\rho z)$$

where $\chi = \mu/\rho.\mathrm{cosec}\psi$ and ψ is the X-ray take-off angle. Since $\phi(0)$ is a constant,the expression may be written as follows;

$$\phi(0) \int_0^{2\rho z} \exp(-\chi.\rho z).d(\rho z)$$

which becomes

$$\phi(0) \quad \left[\frac{\exp(-\chi.\rho z)}{-\chi}\right]_0^{2\rho z}$$

$$= \frac{\phi(0)}{\chi} [\, 1 - \exp(-2\chi.\rho z)]$$

In quantitative analysis the oxygen X-ray intensity from the oxide film are compared with that from a standard of pure alumina. Assuming the X-ray distribution functions are similar in oxidised aluminium and alumina, $\phi(0)$ and χ are the same and the X-ray intensity for an oxide film, thickness t, is given by

$$I_{film} = \frac{\phi(0)}{\chi}.[\, 1 - \exp(-\chi.\rho t)]$$

and we may write

$$\frac{I_{film}}{I_{std}} = \frac{1-\exp(-\chi\rho t)}{1-\exp(-2\chi\rho z).}$$

Thus t is calculated from the above equation by measurement of the two respective X-ray intensities in an electron probe microanalyser, the mean depth of X-ray generation, ρz being determined from an expression developed by Sewell *et al* (1985);

$$\rho z = \rho s_m \quad \frac{\ln U_0}{2.4 + 0.07Z + (1.04 + 0.48\eta)}$$

where ρs_m, the electron range, is given by

$\rho s_m = A/Z[\ (0.733 \times 10^{-5}\ J^{1/2}\ E_0^{3/2}) + (0.735 \times 10^{-6} E_0^{2})\ ]$.

Z is the atomic number; A is the atomic weight; η is the backscatter coefficient (dependant upon the composition of the specimen); U_0 is the overvoltage ratio, E_0/E_c, the ratio of the energy of incident electrons, E_0, to the critical excitation potential of the target atom, E_c; J is the ionisation potential, expressed by 0.0135Z.

CHAPTER 4

RESULTS

4.1 ASSESSMENT OF THE POLARISATION TECHNIQUE

This section describes corrosion experiments which were conducted to assess the performance of the polarisation apparatus. The sensitivity of the DCP technique will be discussed as well as the determination of characteristic potentials from a double cycle polarisation curve. Particular reference will be made to the definition of a protection potential.

4.1.1 ASSESSMENT OF THE POLARISATION APPARATUS

Anodic polarisation studies conducted on 430 stainless steel in de-aerated 1.0N H_2SO_4 produced curves of potential versus current density which were in good agreement with the ASTM G5-78 (1978) data. Fig.4.1(a) shows results obtained by the standard test (represented by the shaded region) and Fig.4.1(b), the experimental curves, A and B, obtained from tests conducted with and without a Luggin capilliary reference electrode. The curves show that the tests are in good agreement with each other and with the ASTM data and that the Luggin probe offers no advantage over the SCE; the Luggin technique was therefore not adopted in the majority of polarisation tests. The data confirm also that the polarisation apparatus, comprising computer-controlled potentiostat, glass polarisation cell, PTFE working electrode assembly and SCE, performs satisfactorily.

4.1.2 THE DOUBLE CYCLIC POLARISATION METHOD

(a) Definition of a Protection Potential

The determination of a pitting potential and corrosion potential from cyclic polarisation curves is well established and is universally agreed upon. The definition of a protection potential, E_{prot}, is, however, a source of controversey amongst a number of authors as mentioned in section 2.3.3(a)(ii). It has been described as the intersection between forward and reverse scans, E_x, (Pourbaix *et al*, 1963) or the potential at which there is an inflection in the reverse scan, E_{infl}, (Otani *et al*, 1988).

To determine an accurate definition of a protection potential, potentiostatic tests were conducted upon specimens of 2124-SiC in order that the current density in the vicinity of the E_{infl} and E_x might be studied. The principle was to establish pitting upon the specimen prior to applying a constant potential. The level of the current density in the sample following polarisation at the preselected potential could then be monitored. If the potential was above the true protection potential, pitting should continue and a high current density would be maintained. If, however, the potential was below E_{prot}, pits should be rendered inactive and the current density would correspondingly decrease to passive values.

It was found by optical microscopy of the corroded surface, that pitting corrosion had occurred on samples of 2124-SiC which were immersed in the salt solution for a period of ~15 minutes. Therefore, in the case of all potentiostatic tests the specimens were immersed in the solution 15 minutes prior to testing.

A DCP curve for 2124-SiC is given in Fig.4.2(a). From this the values of E_{pit}, E_{infl} and E_x could be determined, E_{pit} being recorded from the

second cycle and E_{infl} and E_x from the first cycle. The potentials selected for potentiostatic tests lay in the ranges $E_{pit}>E>E_{infl}$, $E_{infl}>E>E_x$ and $E<E_x$, and were -732mV, -800mV and -1000mV respectively. Results of holding specimens at these potentials for 3 hours are illustrated in Fig.4.2(b), which shows the variation in current density with time. The data indicate that high anodic current densities are recorded for potentials greater than E_x, and that these fluctuate slightly, suggesting that pitting is continuing at these potentials. The pitting is confirmed by the microstructure, Fig.4.3(a). Below E_x the current density is cathodic throughout the test and no fluctuations are seen, indicating that pitting has stopped. Fig.4.3(b) shows that the extent of pitting is similar to that which occurs during immersion prior to testing, Fig.4.3(c), indicating that no further pitting had occurred. It was therefore concluded that the protection potential is best described by the intersection between the forward and reverse potential scans, shown in Fig.4.2(a) as E_x.

(b) Definition of the Characteristic Potentials from a DCP Curve

The DCP curve obtained from SiC particulate-reinforced 2124 alloy (2124-SiC) composite was chosen to characterise the pitting, protection and corrosion potentials, because of the uniform distribution of reinforcement and pore-free microstructure in this material.

Fig.4.4(a) is a typical curve obtained using a potential scan rate of 20mV/min. The curve may be characterised by the potentials E^1_{corr} and E^1_{prot} for the first cycle and E^2_{corr}, E^2_{pit} and E^2_{prot} for the second cycle. The mean values from three DCP tests on 2124-SiC are listed in Table 4.1, together with the experimental scatter of results.

The pitting potential, as illustrated in Fig.4.4(a), was recorded only on the second cycle. During the first cycle, the rapid increase in current density normally associated with E_{pit}, occurred from the corrosion potential. Then during the second cycle, the corrosion potential became shifted to more negative potentials by ~400mV. These observations are shown in the data, Table 4.1; E^1_{corr},which was ~-732±5mV, was close to E^2_{pit}, (-726±5mV). This suggests that the corrosion potential is in the vicinity of E_{pit} during the first cycle and therefore masks the pitting potential. In the second cycle the corrosion potential becomes depressed, thereby producing a clear passive range and allowing a pitting potential to be distinguished. On the basis of this, it was decided to adopt E_{pit} and E_{corr} values from the second cycle where they were more clearly defined.

Regarding the protection potential, the results showed that the second cycle produced slightly more positive values than the first cycle (-946±5mV compared with -965±10mV respectively). To determine whether the movement to more positive values was a feature of repeated cycles, a triple cycle polarisation test was performed on the 2124-SiC specimen. The results, illustrated in Fig.4.4(b), show that the protection potential does indeed become slightly more positive with repeated cycles. Hence it could be concluded that the protection potential was sensitive to repeated polarisation scans and that the first cycle produced the most accurate value for the protection potential.

Another corrosion parameter which may be derived from polarisation curves relates to the area swept out during the scan. This we term the hysteresis area. Table 4.1 shows that the area for the second cycle is slightly smaller than the first, but the range of values for each cycle overlap. The hysteresis area is seen to be different for each cycle,

Fig.4.4(a), as a result of the shift in E_{corr} to more negative potentials and the appearance of a pitting potential on the second cycle. As both E_{corr} and E_{pit} are more accurately represented by the second cycle and are responsible for the shape of the hysteresis loop, it was decided that the hysteresis area would also be better defined from the second cycle.

Thus, all values of the pitting and corrosion potentials and the hysteresis area recorded in this investigation were taken from the second cycle unless otherwise stated. The protection potential, however, was taken from the first cycle.

(c) Sensitivity of the DCP Technique

The sensitivity tests for the DCP method were performed on single crystals of aluminium which had been cut to expose surfaces of four crystallographic orientations (211), (111), (110) and (100) planes.

The results of DCP tests are illustrated by Fig.4.5(a),(b),(c)&(d) and the data are collated in Table 4.2. As the curves in Fig.4.5 show, no major differences can be seen between the samples. All crystals produced well-defined pitting potentials on both cycles, whilst examination of the Epit data, Table 4.2, shows that they were in good agreement between cycles and between orientations if errors are taken into account, (-782±8mV).

The protection potential on the first cycle is similar for all specimens except for the (211) orientation. However, on the second cycle, E_{prot} for the (211) orientation is in much closer agreement with the (111) and (110) samples, (-845mV compared with -860mV). The (100) surface produced a very low value of E_{prot} on the second cycle, although E_{prot} from the first

cycle is in close agreement with the other orientations. The differences in the values of the protection potentials for the (211) plane on the first cycle and the (100) plane on the second cycle can be explained by very slight differences in the current density exhibited by the crystals during the passive region on the forward and reverse scans. The current density of the first forward scan on the (211) plane was slightly higher than that exhibited by other planes and hence the intersection between the forward and reverse scans for (211) was at a slightly higher potential. Regarding the (100) plane, the difference between the current density of the forward and reverse scans on the second cycle were fractionally greater than for the other planes, and hence the intersection between the scans occurred at a lower potential. For both (100) and (211) planes, however, the differences observed were not consistent between cycles

The recorded corrosion potential appeared to be similar for the different crystals, bearing in mind its inherent variability as it represents the potential at which cathodic and anodic reactions are equal but opposite upon the specimen surface.

The results from these tests indicate that whilst slight differences were found between characteristic potentials in one or two cases, these were not consistenet between cycles. It may be concluded, therefore, that the DCP technique, or cyclic polarisation tests in general, are not sensitive to differences in crystallographic orientation under the experimental conditions used.

4.2 CHARACTERISATION OF AS-RECEIVED MATERIALS

Prior to corrosion testing, optical and electron microscopy were employed to characterise the microstructure of the as-fabricated materials.

Specimens were prepared by the metallographic procedures described in sections 3.2.1 and 3.2.2 for unreinforced metals and MMC respectively.

4.2.1 MATERIALS BASED UPON Al-Si-Mg (357) ALLOY

(a) 357 Alloy

An optical micrograph of the 357 alloy, Fig.4.6(a), illustrates a microstructure which is typical of that for a cast alloy with a eutectic structure. It consists of primary aluminium dendrites surrounded by a large amount of eutectic phase which EDS analysis showed was comprising elemental silicon (the darker grey phase) and aluminium. The dendrites were essentially pure aluminium.

Two phases, one of which was almost white in appearance and the other which was light grey, were interspersed within the eutectic phase. They appeared in a "script" form and were more readily visible in the scanning electron microscope, Fig.4.6(b). EDS analysis showed the light grey phase contained aluminium, silicon magnesium and iron, Fig.4.6(c). These results accord with previous studies of a "script" phase in Al-Si casting alloys, and indicate a composition of $Al_8Si_6Mg_3Fe$, as reported in the ASM Metals Handbook (1972). EDS analysis of the white phase showed it was composed of aluminium, silicon and iron, Fig.4.6(d). Another "Chinese-script" phase is reported by Mondolfo (1976) as being a possible micro-constituent of aluminium alloys, the phase having a composition of Fe_2SiAl_8, sometimes called α-(AlFeSi) . This description agrees with our findings and it is therefore likely that the white phase in Fig.4.6(b) is Fe_2SiAl_8.

A notable feature of the cast material was the presence of pores, Fig.4.7(a), which were dendritic in form. They appeared in greater numbers towards the centre of the ingot and probably amounted to several percent of the total volume of the material.

The 357 alloy produced by the liquid metal infiltration route, without fibres, Fig.4.7(b), had a modified eutectic structure. The silicon particles were coarser than in the cast material and more evenly dispersed, giving rise to uniform grains of aluminium rather than a dendritic structure. Within the eutectic, the same intermetallic phases of Fe_2SiAl_8 and $Al_8Si_6Mg_3Fe$ were found.

(b) Carbon-reinforced 357 Alloy Fabricated by Liquid Metal Infiltration

An optical micrograph taken of carbon-reinforced 357 alloy produced by liquid metal infiltration (357-C_L) is illustrated in Fig.4.8(a). The original tows which constituted the fibre preform are evident, with fibres of 8μm in diameter being orientated in the 0° and 90° directions. Fairly extensive regions of matrix metal separate the tows, within which may be seen weft fibres. The overall fibre volume fraction was 50%, but image analysis measurements showed that locally this could rise to 62% in a fibre-rich region. Porosity arising from poor infiltration of the closely packed fibres was apparent, especially at the edge of fibre tows.

The matrix microstructure was much altered by the presence of fibres. The silicon particles were coarser than those seen in Fig.4.7(a), and were more evenly dispersed. In fibre-free regions they were distributed evenly throughout the matrix. In fibre-rich regions only a small amount of Al-Si

eutectic was found, the silicon particles forming on the fibres in the less densely-packed regions; in some cases the particles formed inter-fibre bridges.

In addition to the silicon particles, some second phases were present in the matrix which had a paler appearance, as indicated by A and B in Fig.4.8(a). Phase A has a needle-like morphology, whereas phase B is plate-like in shape. When viewed in the SEM, both phases appeared much whiter than either aluminium or silicon. EDS data from particle A, Fig.4.8(b), shows substantial amounts of aluminium, silicon and iron. Comparison of the X-ray intensities with those reported by Yang and Scott (1991b) for a needle-like phase within the same alloy, indicated that the composition was $FeSiAl_5$. EDS data from phase B, Fig.4.8(c), shows chromium to be present in addition to aluminium, silicon and iron. The height of the aluminium peak from B phase varied considerably from particle to particle when compared with the relative heights of the iron, silicon and chromium peaks. This effect was attributed to differing amounts of excitation of the surrounding aluminium matrix as a result of the electron beam penetrating the thin plate-like particles. This made it difficult to deduce a precise composition. Finally, EDS analysis of the weft, Fig.4.8(d), showed it to contain silicon, calcium and oxygen which confirms it as being glass.

(c) Carbon-reinforced 357 Alloy Fabricated by Squeeze Casting

The fibres, which were 8μm in diameter, were more uniformly distributed in this squeeze cast material, Fig.4.9(a), than in the material produced by LMI. The fibre volume fraction, as deduced by image analysis, was ~63%. As with the LMI composite, the Al-Si eutectic was affected by the presence

of fibres and second phases precipitated preferentially at the matrix-rich regions where fibres had separated during manufacture, Fig.4.9(b). The $FeSiAl_5$ phase was again found in fibre-free regions, Fig.4.9(b). A second intermetallic phase consisting of aluminium, silicon, iron and magnesium was occasionally found, identical to that detected in the unreinforced alloy, see Fig.4.6(c).

(d) Nicalon-reinforced 357 Alloy

The Nicalon-reinforced 357 alloy, (357-Nic) was fabricated by liquid metal infiltration and supplied in two forms; one (material A) contained a fibre weft, Fig.4.10(a), and the other (material B), Fig.4.10(b), contained initially an organic polymer binder which had almost been completely burnt-off during fabrication. The volume fraction of fibres in both materials was ~50%, but image analysis showed that in material A, this was as high as 65% where the fibres remained in closely-packed tows. Evidently with material B, the burning-off of the binder during fabrication allowed the fibres to spread out during infiltration to produce a more homogeneous distribution. The mean diameter of the Nicalon fibres was 15μm.

As noted for 357-C_L MMC, the Al-Si eutectic was modified by the presence of fibres and the silicon particles tended to form preferentially on them. As in material A, the eutectic phase was dispersed evenly throughout the fibre-free regions, with only a small amount of silicon forming at the fibres.

The presence of the needle-like $FeSiAl_5$ intermetallic was detected also in these materials, although there was much less in material B than in

material A. The weft fibre in material A was found by EDS analysis to be glass of similar composition to that found in the 357-C_L material, Fig.4.8(d).

(e) Saffil-reinforced 357 Alloy

The Saffil-reinforced 357 alloy (357-Saf) is illustrated in Fig.4.11(a), and was produced by liquid metal infiltration. The Saffil short fibres, which were 3μm in diameter comprised a volume fraction of 20% and were uniformly distributed about a planar random orientation.

Once again the Al-Si eutectic was modified by the presence of a reinforcement, the coarser silicon particles forming preferentially at the fibres and sometimes forming bridges between fibres. Porosity between fibres is clearly visible in the SEM back-scattered electron image (BEI) image as well as the white, needle-like $FeSiAl_5$ phase, Fig.4.11(b).

4.2.2 MATERIALS BASED UPON Al-Cu-Mg (2124) ALLOY

(a) 2124 Alloy

The 2124 alloy was supplied in the T851 condition, *i.e.* solution teated, cold-worked by stretching to ~2% permenant strain to relieve stresses and then artificially aged. Fig.4.12 shows the microstructure consists of small precipitates aligned in the direction of cold-work. EDS analysis showed the alloy regions to consist of aluminium, with a small amount (<2%) of dissolved copper and magnesium. Second phases are present and these were found to consist of two types, Fig.4.13(a)&(b). Both phases appear white in the scanning electron micrographs, and are therefore only

distinguishable by slight differences in their morphology. One phase, Fig.4.13(a), is small and rounded and contains aluminium, copper and magnesium, Fig.4.13(c). The composition of the phase is thought to be Al_2CuMg, an intermetallic compound which is reported by Polmear (1981) as being the most commonly found precipitate in Al-Cu-Mg alloys. The other phase, Fig.4.13(b), is larger and slightly more irregular in shape compared with the Al_2CuMg precipitate. EDS studies on this phase, Fig.4.13(d), showed it to contain aluminium, copper, iron and manganese. A comparison of these findings with those reported in the ASM Metals Handbook (1972) for a 2024 alloy (which is of an almost identical composition to the 2124 alloy), showed that this phase is likely to be $(CuFeMn)Al_6$.

(b) Carbon-reinforced 2124 Alloy

The carbon-reinforced 2124 alloy was fabricated by squeeze casting using a facility available at RMCS Shrivenham. A mostly uniform distribution of fibres, which were 8μm in diameter, was found, the microstructure at low magnification appearing very similar to that for the 357-C_S MMC, also fabricated by squeeze casting, see Fig.4.9(a). The volume fraction of fibres as measured using an image analyser, was ~63%. As with the 357-C_S material, also fabricated by squeeze casting, a few fibre-free regions were found where the fibres had separated during fabrication and it was here that preferential precipitation of second phases occurred. This is illustrated in the scanning electron micrograph, Fig.4.14(a). As with the 2124 alloy, two phases were found, one containing aluminium, copper and magnesium and the other aluminium, copper, manganese and iron. However, the morphology of the phases in the composite material was very different. Fig.4.14(b), a matrix-rich area, shows dendrites which

consist of essentially aluminium with some copper and magnesium, surrounding the dendrites is a mixture of large particles (up to 10 μm in diameter) and a much finer dispersion, see Fig.4.14(b). The fine dispersion consisted of aluminium, copper and magnesium, whereas the larger phase was found to consist of aluminium, copper, manganese and iron. EDS analysis showed the phases to be of the same composition as those found in the unreinforced 2124 alloy, *i.e.* Al_2CuMg and $(CuFeMn)Al_6$, illustrated by the EDS results, Fig.4.13(c)&(d).

(c) Silicon Carbide-reinforced 2124 Alloy

The 2124 alloy reinforced with silicon-carbide particles, Fig.4.15(a), was fabricated by a powder metallurgy process. The particles were found by image analysis to occupy a volume fraction of ~20%. The average diameter of the particles is 3μm and they are homogeneously dispersed, appearing to be orientated in the direction of hot-rolling given to the hot isostatically pressed material. Second phases of less than 3μm diameter were clearly visible as white particles in the scanning electron microscope, Fig.4.15(b). Their small size made EDS analysis difficult, but results showed the presence of two phases with either an aluminium-copper or an aluminium-copper-manganese-iron composition. It is likely that the latter phase is the same as that found in the unreinforced alloy, $(CuFeMn)Al_6$, whilst the other is probably $CuAl_2$, a well-established precipitate in aluminium-copper alloys. The absence of magnesium in this phase compared with the Al_2CuMg in the unreinforced alloy is possibly related to the hot-rolling process. In the process of rolling the 2124-SiC material into a thin sheet magnesium may have been leached from the surface as a result of oxidation at the high temperatures involved in the process.

4.2.3 MATERIALS BASED UPON ALUMINIUM

(a) Commercial Purity Aluminium

The commercial purity aluminium was 99.5% pure, the remaining 0.5% being essentially accounted for by the presence of impurity elements, mainly iron and silicon. Consequently, as illustrated by the microstructure, Fig.4.16, a second phase was present which EDS analysis confirmed was composed of aluminium, iron and a small amount of silicon. This is consistent with the ASM Metals Handbook (1972), where it is reported that phases in unalloyed aluminium contain impurity elements such as iron and silicon, generally in the form $Al_{12}Fe_3Si$.

(b) Carbon-reinforced Super Purity Aluminium

The carbon-reinforced aluminium material was fabricated using the squeeze casting facility at RMC Shrivenham. As for the other MMC fabricated by squeeze casting, the 8μm fibres were uniformly distributed throughout the matrix. No evidence of second phases within the matrix was found.

Analysis of the fibre/matrix interface was carried out in the transmission electron microscope (TEM). Fig.4.17(a) is a transmission electron micrograph of the specimen showing the carbon fibre, the aluminium matrix and a reaction zone containing lath-like crystals situated at the fibre/matrix interface. The crystals, which appeared to have grown into the matrix in a variety of directions, were found to have lengths of up to ~300nm long and widths of up to ~100nm. Analyses of the fibre, matrix and the interfacial crystals were made by selected area diffraction (SAD). The carbon fibre gave a SAD pattern of diffuse rings, Fig.4.17(b),

indicating a polycrystalline structure. The aluminium matrix produced a SAD pattern composed of a regular array of spots, Fig.4.17(c), analysis revealing this region to be orientated along a <114> zone axis. A SAD pattern of a needle-like crystal at the interface Fig.4.18(a)&(b), revealed a row of strong reflections. EDS showed that the crystals were composed of carbon and aluminium, whilst analysis of the diffraction spot pattern showed that the strong reflections corresponded exactly to the 0003, 0006, 0009, 000,12 planes of an aluminium carbide crystal, Al_4C_3. Fig.4.18(c) is a TEM micrograph showing lattice fringes in a crystal, which have a spacing of 0.84nm and lie parallel to the crystal axis. These correspond to the basal planes of the carbide lattice. Diffraction patterns of the carbide crystals and the aluminium grain in which the crystal was situated showed little evidence of an orientation relationship between their structures.

4.3 CORROSION STUDIES ON 357 ALLOY

4.3.1 GRAVIMETRY

Weight changes for 357 alloy specimens corroded for times of up to 3 weeks are recorded in Table 4.3. The experimental scatter in the results represents an estimated error of ~20% probably incurred from measurements of mass loss and exposed area. As the data in Table 4.3 show, a weight loss was recorded for all specimens. The table also includes values of corrosion rates, which were obtained by dividing the weight loss by the time period of the test. Fig.4.19, which illustrates the variation of corrosion rate with immersion time, shows that the corrosion rate decreased from 0.05 to 0.012g.m^{-2}.h^{-1} during 3 weeks immersion.

4.3.2 OPEN CIRCUIT POTENTIAL

The changes in open circuit potential (OCP) of a freely corroding specimen of 357 alloy over a period of 3 weeks, Fig.4.20(a), may be characterised by the following features. During the first hour of immersion the potential was at its highest, fluctuating around an almost constant value of -760mV. After 1 hour, the potential decreased rapidly, until after ~6 hours it reached a minimum of -1080mV. Then followed a slight increase over the next 4 days, after which there was a return to the high potential seen at the beginning of the test and this was maintained throughout the remainder of the experiment. The other specimens of 357 alloy exhibited similar behaviour with the exception that for one specimen, the return to high potential at the later stages of the test was not seen, see Fig.4.20(b); once the potential had reached a minimum value, it remained there for the rest of the experiment. The average values of the initial maximum corrosion potential, E_{init}, and the minimum potential, E_{min}, recorded

over three tests are given in Table 4.4. The results illustrate that E_{init} experienced only a small variation (±5mV) between tests on different samples, whereas larger deviations (±40mV) were found for E_{min}.

4.3.3 DOUBLE CYCLE POLARISATION

(a) 20mV/min Potential Scan Rate

A curve obtained from a DCP test conducted on 357 alloy at a potential scan rate of 20mV/min is shown in Fig.4.21(a). The average data recorded over three tests are given in Table 4.5. As Fig.4.21(a) illustrates, the pitting potential was not clearly defined during the first forward scan. The sudden increase in current density, which is normally associated with E_{pit}, occurred from the corrosion potential. An inflection point was observed on both reverse scans. Two unusual features may be noted. Firstly, a "double hysteresis loop" was formed during the first cycle owing to the pronounced inflection in the reverse scan intersecting the forward scan on two occasions prior to reaching the protection potential. Secondly, the protection potential occurred below the corrosion potential.

Table 4.5 lists the mean values of E_{pit}, E_{prot}, E_{corr} and the hysteresis area (HA). Values recorded for E_{pit} were in excellent agreement - 743±5mV. The reproducibility of the corrosion potential and protection potentials was, however, much less, giving values of -995±150mV and -1079±80mV for E_{corr} and E_{prot} respectively. The hysteresis area gave a value of 213±45μC.

A typical microstructure taken after the DCP test on 357 alloy, Fig.4.21(b) shows that corrosion took the form of pitting, with preferential attack occurring at the Al-Si eutectic regions between the aluminium dendrites.

It was evident that the pits in the eutectic areas contained light grey intermetallic phases, which EDS analysis confirmed were of the same composition as the phases in the uncorroded material, *c.f.* Fig.4.6(c)&(d), *i.e.* $Al_8Si_6Mg_3Fe$ and Fe_2SiAl_8 respectively. Corrosion, in the form of numerous small pits, was visible within the aluminium dendrites

(b) 2mV/min Potential Scan Rate

A DCP curve obtained at a scan rate of 2mV/min on 357 alloy is given in Fig.4.22(a) and the corresponding data recorded in Table 4.5. As the results illustrate, the pitting potential (-751±5mV) and the protection potential (-1030±5mV) are in reasonable agreement with the data from tests performed at 20mV/min (-743±5mV and -1079±80mV respectively). The hysteresis area gave a value of 220±60μC which was only 7μC more than that found for the faster rate. The corrosion potential, E_{corr}, is more positive at the slower rate, -854±25mV compared with -995±150mV at the faster rate. If, however, the large scatter in results is considered, the difference between the results for each test overlap.

The DCP curve, Fig.4.22(a), illustrates that the shape of the first cycle is different from that seen at the faster scan rate, see Fig.4.21(a). It shows a well-defined value of E_{pit} and the double hysteresis effect, which was apparent at the faster rate has disappeared. The second cycle is also different such that the pitting potential, which was clearly marked at the faster scan rate, appears as only a small step in the curve.

The microstructure following corrosion, Fig.4.22(b), shows more severe attack than that for the 357 alloy at the faster scan rate, see Fig.4.21(b). The corrosion pits situated at the eutectic regions between the dendrites

are larger and within the eutectic regions where pits had not developed, attack occurred around the silicon particles and the intermetallic phases. The aluminium dendrites were more severely attacked than at the faster rate and where the tiny pits within the dendrites had propagated and merged, the dendrites took on a dimpled appearance.

4.3.4 CORROSION MORPHOLOGY

The development of corrosion over increasing periods of immersion ranging from 1 hour to 3 weeks was investigated using a different specimen for each immersion period. After 1 hour, small pits were visible with regions of darkness and brightness surrounding them, Fig.4.23(a). High magnification showed that most pits formed around the intermetallic phases confirmed by EDS analysis as being the $Al_8Si_6Mg_3Fe$ and Fe_2SiAl_8 phases, the latter phase being associated with a greater number of pits. A few pits only had formed at silicon rods.

The rings of brightness (A) and darkness (B) surrounding a pit suggested that these may represent a different oxide film thickness. To verify this, measurements of the oxide thickness were made using the technique described in section 3.4.6. This involved measuring the oxygen X-ray intensity from the oxide film over the sample by WDS analysis and comparing it with the intensity from an alumina (Al_2O_3) standard analysed under the same conditions. Firstly a line scan was carried out across a pit, commencing and finishing ~40μm either side of the pit. The sampling interval was 1μm and the sampling time at each interval was 20 seconds. The results of the line scan are illustrated in Fig.4.23(b) as variation in oxygen X-ray intensity versus distance across a pit. The oxygen X-ray intensity is approximately constant away from the pit region

(C). Within the pitted region (A) large changes in the intensity were found due to differences in geometry resulting from corrosion and the presence of intermetallic phases inside the pit. From three scans, the mean oxygen X-ray intensity beyond the pit (region C) was found to be 1020 counts and the maximum value (region B) was 1800 counts. From these data, the thickness of oxide was calculated using the method detailed in section 3.4.6. This gave a thickness near the pit edge (B) of ~200Å, whilst the average thickness away from the pit (C) was ~50Å.

The size of the corrosion pits did not appear to increase after an immersion period of 1 day. After 3 days, however, the microstructure, Fig.4.24(a), showed that more general attack had taken place, with corrosion occurring preferentially around the silicon rods within the eutectic regions and around the intermetallic phases. The aluminium dendrites suffered corrosion in the form of small pits.

The extent of attack remained little changed after immersion for the following week, but after 3 weeks, Fig.4.24(b), the eutectic regions were severely attacked and the dendrites experienced a more general form of corrosion. The silicon rods were no longer distinguishable, although some of the intermetallic particles could still be seen in the corroded regions.

An indication of the depth of corrosion after 3 weeks was found from microscopy of cross-sections made through the corroded surface of the specimens. An example is given in Fig.4.24(c). The pits were mostly hemispherical and often followed regions of the eutectic phase which contained the silicon rods and intermetallic phase. The depth of pitting measured from microstructures ranged from 10-45μm, to give an average value of 15μm.

4.4 CORROSION STUDIES ON CARBON REINFORCED 357 ALLOY FABRICATED BY LIQUID METAL INFILTRATION

4.4.1 GRAVIMETRY

Weight changes for 357-C_L specimens immersed for periods ranging from 1 day to 3 weeks are listed in Table 4.6. The results illustrate, that the samples gained rather than lost weight after each immersion period despite attempts to remove surface corrosion products by mechanical and chemical cleaning. No change in the weight was found after repeating the cleaning procedure. The rate of weight gain (see Table 4.6) is plotted with respect to time in Fig.4.25. The graph shows that the rate decreases with immersion time, reaching an almost constant rate of weight gain of $8x10^{-3}$ $g.m^{-2}.h^{-1}$ after several days.

4.4.2 OPEN CIRCUIT POTENTIAL

The change in OCP with time for a sample of 357-C_L, Fig.4.26, was similar to that of the unreinforced alloy during the early stages of immersion, the potential fluctuating slightly about a value of ~-735mV, before suddenly decreasing after 1 hour immersion to a value of ~-880mV. The OCP varied around the minimum over the following few days, until a sudden increase in potential occurred after 10 days and a value of -760mV was reached, which was slightly more negative than the initial potential. This remained constant for the remainder of the test. The mean values and deviations of E_{init} and E_{min} found over three tests are given in Table 4.4.

4.4.3 DOUBLE CYCLE POLARISATION

(a) 20mV/min Potential Scan Rate

The results of DCP tests on samples of 357-C_L, Fig.4.27 and Table 4.5, illustrate that the pitting potential was once again not recorded during the first cycle. It was, however, clearly visible on the second cycle. Unlike the curve for 357 alloy, Fig.4.21(a), no point of inflection is visible on the reverse scan of either cycle. The protection potential occurred below E_{corr} on the first cycle, but on the second cycle, it is recorded at more positive potentials than E_{corr}, owing to a shift in the corrosion potential to more negative potentials. The values of E_{pit} (-752±10mV), E_{prot} (-850±15mV), E_{corr} (-919±10mV) and hysteresis area (191±5μC) all showed good reproducibility between tests.

The microstructure following a DCP test on the 357-C_L MMC shows that corrosion took the form of pits which occurred preferentially at the edge of the fibre tows often being associated with light grey platelet and needle-like phases, Fig.4.28(a), or the glass fibre weft, Fig.4.28(b). EDS analysis confirmed the needle phase to be the intermetallic $FeSiAl_5$ found in the uncorroded composite, see Fig.4.8(b). The platelet phase was of the same composition as that found during analysis of the polished material, see Fig.4.8(c), and contained aluminium, silicon, iron and chromium. Where attack occurred around the fibres, the silicon particles which formed at the fibres remained unattacked and could be seen to be attached to the fibres, Fig.4.28(c). This picture illustrates well the formation of silicon rods at the fibre surfaces during the LMI fabrication process. An example of a pit extending into the composite is given in Fig.4.28(d), a micrograph

of a cross-section through the corroded surface. The micrograph shows that the attack extends along the fibres and around the (AlSiFeCr) platelet and $FeSiAl_5$ needle-like phases. The pits were generally very narrow, and their growth was channelled along the fibres into the composite. The depth of pits as measured from microscopy, varied considerably across the surface from ~30-400μm, with an average value of 150μm.

(b) 2mV/min Potential Scan Rate

A DCP curve from a test conducted at a 2mV/min scan rate on 357-C_L, Fig.4.29(a), shows that a pitting potential was not recorded on either the first or second cycles and that the rapid increase in current density normally associated with E_{pit}, occurred at the corrosion potential. The corrosion data are listed in Table 4.5. The corrosion potential(-749±5mV), although vastly different from that recorded at the faster scan rate (-919±10mV), was very close to the value of the pitting potential at the 20mV/min rate (-752±10mV). The protection potential (-837±5mV) was also in good agreement with E_{prot} at the faster rate (-850±15mV). The hysteresis area, however, had a value of 104±20μC, which was almost 90μC less than that for the faster rate.

A typical microstructure after the DCP test is shown in Fig.4.29(b). The corrosion is more severe than that seen after the faster scan rate, see Fig.4.28(a)&(b). Discrete corrosion pits are less visible, the attack extending over most of the composite surface. Where less severe attack of the matrix had taken place, pits had initiated around the second phases, identified by EDS analysis as $FeSiAl_5$ and (AlSiFeCr), see Figs.4.8(c)&(d).

The depth of corrosion pits was estimated from polished cross-sections through the corroded surface. The morphology of the pits was the same as that seen at the faster scan rate, but the extent of penetration was more severe. In one instance, however, the corrosion had extended to a depth of ~2000μm, Fig.4.29(c). The mean pit depth measured was ~300μm. The pitting attack in nearly all cases was concentrated at the edge of the fibre tows, as evidenced by Figs.4.29(c).

4.4.4 GALVANIC COUPLE

The galvanic current flowing between a specimen of 357 alloy and several tows of fibres immersed in the corrosion solution remained almost constant at ~465μA over a period of 2 hours. From the galvanic current a corrosion rate was calculated using Faraday's law:

$$\text{Corrosion rate } (mm.yr^{-1}) = \frac{315ki}{A\rho}$$

where: i = current (μA)

ρ = density ($g.cm^{-3}$)

A = area of anode (cm^{-2})

k = electrochemical equivalent ($g.Coulomb^{-1}$)

$$= \frac{\sum \text{atomic weight fraction of each element} \times \text{atomic weight of each element}}{\text{valency} \times 96500}$$

In the case of alloys, the equivalent weight is calculated using the atomic fractions of each component element. It therefore assumes that each element present corrodes at a uniform rate. The value of k calculated for 357 alloy was $0.0917g.C^{-1}$.

The corrosion rate for 357 alloy coupled to carbon fibres was 5.0mm.yr^{-1}. Table 4.7 records the galvanic current data and the corrosion rates for this couple.

4.4.5 CORROSION MORPHOLOGY

Preliminary "interrupted" tests were conducted upon a sample of 357-C_L immersed in the corrosive solution for a total of 1 day. The sample was removed at intervals so that the corrosion morphology of a particular area could be followed. Fig.4.30(a),(b)&(c) are micrographs of an area before immersion, after 6 hours and after 1 day respectively. The uncorroded area shows the edge of two carbon fibre tows, some silicon particles, light grey needles of $FeSiAl_5$ and a (AlSiFeCr) platelet. After 6 hours immersion, there is evidence of attack at the $FeSiAl_5$ needles and around the fibres. Small corrosion pits are just visible within the matrix and also at the interface of a few silicon particles. After immersion for 1 day, the corrosion at the $FeSiAl_5$ needles was quite severe and there was now visible attack around the (AlSiFeCr) platelet. Corrosion at the fibre-matrix interface had also extended further into the matrix and more small corrosion pits had developed within the matrix region between the fibre tows.

Another set of experiments involved the immersion of a number of specimens, each for a prescribed length of time ranging from 1 day to 3 weeks. The corrosion morphology after 1 day was essentially the same as that described above for the specimen in the interrupted tests with the exception of cracks within the fibre tows which ran along the fibre-matrix interface, Fig.4.31(a). After 3 days the attack was more severe, Fig.4.31(b),

much of the matrix surrounding the fibres and intermetallic phases being corroded away.

Following immersion for 3 weeks the microstructure showed evidence of extensive attack at the carbon fibre-matrix and at the glass-fibre weft/matrix interfaces, Fig.4.32(a), the matrix having been corroded almost completely away. At the fibre-free regions the attack was concentrated mostly at the $FeSiAl_5$ needles. The cracks in the fibre tows were more widespread than in the 1 day specimen and they had opened up to form large crevices of ~30-40μm wide, Fig.4.32(b).

Examination of cross-sections through the specimen corroded for 3 weeks showed that most of the matrix had been corroded to a depth of ~45μm, leaving bare fibres protruding at the surface, Fig.4.32(c). However, in some instances the attack was more severe. One case in particular, Fig.4.32(d), showed the attack had penetrated through a ~6mm thick specimen, causing corrosion to occur at the rear of the composite. The attack was concentrated at the edge of a fibre tow. Other cases of extensive attack also showed that the edge of the fibre tows appeared to act as a preferential site for this type of attack, with much of the corrosion product being retained within the specimen.

4.5 CORROSION STUDIES ON CARBON-REINFORCED 357 ALLOY FABRICATED BY SQUEEZE CASTING

4.5.1 OPEN CIRCUIT POTENTIAL

The OCP characteristics exhibited by samples of 357-C_S immersed in the corrosive solution for 3 weeks were similar to those of 357 alloy, see Fig.4.20(a); the results are listed in Table 4.4. A potential of ~-784±60mV occurred during the first hour of immersion and again during the later stages of the test, with a minimum potential of -934±60mV being recorded after ~4 hours.

4.5.2 DOUBLE CYCLE POLARISATION

DCP tests performed on samples of 357-C_S employed a 20mV/min scan rate, an example of a DCP curve being given in Fig.4.33(a). Unlike the curve for 357-C_L, an inflection is apparent in both reverse scans. The protection potential occurs below E_{corr} once more, and the pitting potential is seen clearly only during the second cycle. The data are summarised in Table 4.5. The values of E_{pit} and the hysteresis area were very reproducible (-763±5mV and 119±10μC respectively) in contrast to values for the protection and corrosion potentials, -896±45mV and -880±60mV respectively.

Microstructural examination following DCP tests showed that pitting had taken place, Fig.4.33(b), preferential sites for attack being the silicon rods and the needle-like intermetallic phase in matrix-rich regions. EDS analysis confirmed the needle-like phase to be $FeSiAl_5$.

Cross-sections through the corroded surface showed the pit morphology to be similar to that described for the same MMC system fabricated by LMI *i.e.* narrow pits which propagated down into the composite along the fibres. The depth of pitting was considerably less than in the 357-C_L material and the pit depth did not vary as much. The average pit depth was measured as ~100μm with pits ranging from ~40-220μm.

4.5.3 CORROSION MORPHOLOGY

The corrosion morphology of 357-C_S was investigated by immersing different samples for increasing periods of time from 1 day to 3 weeks. After 1 day the corrosion was slight. Only a few pits were visible across the specimen surface and these were mostly situated at the edge of fibre-rich regions, Fig.4.34(a), and at the $FeSiAl_5$ needles and silicon rods. Following 3 days immersion, many small corrosion pits had developed and again these occurred in matrix-rich regions at the second phases, Fig.4.34(b).

Corrosion at the fibre-matrix interface became more evident after immersion for 1 week. Pits were surrounded by large circular regions which were apparently unattacked, Fig.4.35(a). Around the uncorroded regions, the matrix surrounding the fibres had been attacked, exposing the bare fibres and the silicon rods. This is illustrated by Fig.4.35(b), which shows the edge of an uncorroded region surrounding a pit and the neighbouring region which has suffered more extensive attack. The silicon rods and intermetallic phases were the sites of preferential attack within the matrix, Fig.4.35(c), whilst the aluminium grains contained small, shallow pits, which gave the grains a dimpled appearance.

After 3 weeks corrosion, most of the matrix at the fibre-matrix interfaces had been corroded away, Fig.4.36(a). This exposed the fibres and also the silicon particles which had formed inter-fibre bridges, Fig.4.36(b). Cross-sections made through the composite confirmed that the matrix had been corroded extensively in fibre regions, Fig.4.36(c). The depth of attack varied between 25-300μm across the surface, the mean depth being ~95μm.

4.6 CORROSION STUDIES ON NICALON-REINFORCED 357 ALLOY

4.6.1 GRAVIMETRY

The weight losses for periods of up to 3 weeks for type A specimens of 357-Nic (with glass binder) are recorded in Table 4.8. Corrosion rate data (Table 4.8) showed that the rate of attack diminished over the first week of immersion until an almost constant rate of ~$5x10^{-3}$ $g.m^{-2}.h^{-1}$ was reached.

4.6.2 OPEN CIRCUIT POTENTIAL

The behaviour of the OCP for type A specimens (with glass binder), see Table 4.4, during 3 weeks corrosion was similar to that for other 357-based materials, *e.g.* Fig.4.20(a). During the first hour, a high OCP of -778±15mV was recorded. This was followed by a sharp decline to more negative potentials, where a minimum of -1085±45mV was reached. The OCP then recovered to potentials of, or a little less than, E_{init}.

4.6.3 DOUBLE CYCLE POLARISATION

(a) 20mV/min Potential Scan Rate

DCP characteristics for type A 357-Nic were similar to 357-C_L, see Fig.4.27, except that the protection potential occurred above rather than below the corrosion potential. The data, Table 4.5, show that E_{pit} and E_{prot} were reproducible between tests, with values of -751±5mV and -810±10mV respectively. Regarding the corrosion potential and the hysteresis area, the results were somewhat more variable, values of -969±65mV for E_{corr} and 283±70μC for the hysteresis area being recorded.

Examination of the corroded microstructure showed that pitting had once again occurred at the matrix-rich regions and in particular along the glass fibre weft, Fig.4.37(a). Some of the pits had developed around the needle-like $FeSiAl_5$ phase, Fig.4.37(b). Very little corrosion had taken place within the fibre tows, and no general corrosion was found.

(b) 2mV/min Potential Scan Rate

The curves produced from DCP tests performed at a scan rate of 2mV/min on type A samples of 357-Nic were almost identical to those recorded for 357-C_L, see Fig.4.29(a). There was no evidence of a pitting potential on either the first or second cycles; the increase in current density occurred once more from the corrosion potential on each cycle. The mean data obtained from three tests are given in Table 4.5. As noted for the 357-C_L material, the corrosion potential at the slow scan rate (-742±20mV), was very close to the pitting potential obtained from tests at the faster rate (-751±5mV). The protection potential at the 2mV/min scan rate (-863±15mV), was ~50mV more negative than E_{prot} at the 20mV/min rate.

However, the hysteresis area (237±10μC) was in reasonable agreement with that obtained from tests at the faster rate (283±70μC), taking the scatter of results into account.

A typical microstructure after a DCP test at the slower scan rate, Fig.4.38(a), shows that the attack, though of a similar nature to that at the faster scan rate, is much more extensive, with most of the matrix-rich regions and areas containing the glass-fibre wefts being severly corroded. Fig.4.38(b) shows that some matrix regions surrounding silicon rods, $FeSiAl_5$ needles and fibres have been corroded away.

4.6.4 GALVANIC COUPLE

The galvanic current flowing between a sample of 357 alloy and several tows of Nicalon fibres was measured as 72μA using a zero resistance ammeter. The current remained constant over a period of two hours. From the current a corrosion rate of 0.8 $mm.yr^{-1}$ was calculated. These data are listed together with data from other galvanic couples in Table 4.7.

4.6.5 CORROSION MORPHOLOGY

The corrosion behaviour of 357-Nic was assessed by immersing different samples for various periods of time ranging from 1 hour to 3 weeks. Both type A (with glass binder) and type B (without binder) specimens were studied. After immersion for 1 day, a few areas of corrosion were found. In material A, these were mostly sited at the glass binder weft and to a lesser extent around the fibres, as illustrated in Fig.4.39(a). In type B, the attack occurred preferentially at the fibre-matrix interface in a few areas only, Fig.4.39(b).

The extent of attack did not increase greatly over 3 days immersion. After 1 week, however, corrosion of material A was more severe, occurring as corrosion pits adjacent to fibres and the glass binder. On closer examination of the pitted regions, Fig.4.40(a), it became evident that white needles at the fibres were present. These were the $FeSiAl_5$ intermetallics found in the uncorroded material. Regarding material B, the corrosion was found to have attacked most fibre/matrix interfaces as well as regions around the silicon particles and intermetallic needles, Fig.4.40(b).

After immersion for 3 weeks, material A had experienced severe corrosion at the glass binder but to rather less extent at the fibre/matrix interface, Fig.4.41(a). Material B was found to have been extensively attacked in some regions, with most of the matrix having been corroded away, Fig.4.41(b). In other regions the corrosion was less severe, Fig.4.41(c), and most of the matrix remained between the fibres. There was also evidence in these areas of corrosion around the silicon rods and intermetallic needles. Examination of cross-sections through the corroded material revealed that the attack in the type A material was concentrated at the binder phase. The mean depth of corrosion was found to be ~85μm, the depth ranging up to ~350μm. Regarding material B, the attack followed the fibre/matrix interface, the depth of corrosion also extending up to ~350μm.

4.7 CORROSION STUDIES ON SAFFIL-REINFORCED 357 ALLOY

4.7.1 GRAVIMETRY

As found for the 357-C_L MMC, specimens of 357-Saf gained weight during immersion also, but to a larger extent. Weight gains and corresponding rates of weight gain for immersion times of up to 3 weeks are recorded in Table 4.9. Further cleaning did not reduce these values. The rate of weight gain decreased from ~1.0 $g.m^{-2}.h^{-1}$ to 0.2 $g.m^{-2}.h^{-1}$ over the test period but the rate did not appear to approach a steady value seen in the case of 357-C_L.

4.7.2 OPEN CIRCUIT POTENTIAL

The variation in the OCP on 357-Saf was similar to that recorded on other 357-based materials. The mean values of E_{init} and E_{min}, Table 4.4, were -763±5mV and -990±70mV respectively.

4.7.3 DOUBLE CYCLE POLARISATION

(a) 20mV/min Potential Scan Rate

A typical DCP test performed at a scan rate of 20mV/min on 357-Saf is illustrated in Fig.4.42(a). An unusual feature of the curve, was the appearance of a pitting potential on the first cycle, visible as only a slight inflection. E_{pit} was more clearly revealed on the second cycle owing to the shift of the corrosion potential to more negative values. The pitting potentials from both cycles were closely similar.

Values of E_{pit}, together with the other DCP data, are recorded in Table 4.5. Once again, excellent reproducibility was found for E_{pit}, (-761±5mV). The protection and corrosion potentials showed rather more scatter, however, having values of -947±45mV and -938±50mV respectively, whilst the hysteresis area was 85±15μC.

The microstructure after a DCP test, Fig.4.42(b), shows random corrosion pits of ~100μm or more in diameter. Microscopy of cross-sections through the corroded surface showed that the pits were different in shape to those seen in the carbon fibre-reinforced composites described in the previous sections, Fig.4.42(c). There was little restriction on the pits propagating laterally as was noted in the other MMC, and hence the pits were wider, shallower and hemispherical in appearance. The pit depths across the specimen surface ranged from ~30-120μm, with an average of 65μm.

(b) 2mV/min Potential Scan Rate

DCP tests performed at this scan rate (2mV/min) on 357-Saf gave slightly different results compared to those on other materials. Fig.4.43(a), shows that E_{pit} is visible on both cycles, being most clearly defined by the second cycle. The results, Table 4.5, show that E_{pit} (-770±5mV) and E_{corr} (-939±80mV), accord with those at the faster scan rate (-761±5mV and -938±50mV repectively). The protection potential (-1006±30mV), was ~60mV more negative than that at the faster rate but the large deviation in E_{prot} at the 2mV/min and 20mV/min rates (±30mV and ±45mV respectively), meant that the results for each rate in fact overlapped. The hysteresis area (132±10μC) was found to be ~50μC larger than for the faster scan rate.

The microstructure of the specimen after testing at the 2mV/min scan rate, Fig.4.43(b), showed once again that the corrosion was more severe than with the faster rate, although the nature of attack was the same. The pits were more extensive, and in many cases had merged together.

4.7.4 CORROSION MORPHOLOGY

After immersion for 1 day, SEM revealed that there was very little corrosion of 357-Saf material. Slight attack of the matrix had occurred around white phases, Fig.4.44(a), identified by EDS analysis as $FeSiAl_5$. The extent of corrosion did not appear to change with immersion times up to 3 days although after 1 week the attack around $FeSiAl_5$ was more severe and now took the form of corrosion pits, Fig.4.44(b).

Following immersion for 3 weeks, corrosion had occurred at the fibre/matrix interfaces, at the intermetallic and silicon phases, Fig.4.45(a) and in some areas corrosion pits had developed, Fig.4.45(b). Examination of corroded cross-sections showed that the depth of attack varied between ~10-35μm, the mean depth of pits being ~15μm. Corrosion pits often contained needles of $FeSiAl_5$, Fig.4.45(c). The pits were hemispherical in form and there was no evidence of retained corrosion products within them.

4.8 CORROSION STUDIES ON 2124 ALLOY

4.8.1 GRAVIMETRY

The weight losses measured on 2124 alloy are given in Table 4.10 for immersion times of up to 3 weeks. The corrosion rates, also recorded in

Table 4.10, show that the rate of attack decreased most quickly during the first 3 days of immersion from ~20x10^{-3} g.m^{-2}.h^{-1} to ~10x10^{-3} g.m^{-2}.h^{-1} but between 1 and 3 weeks, the rate reached a fairly constant level.

4.8.2 OPEN CIRCUIT POTENTIAL

Samples of 2124 alloy exhibited a variation in OCP typified by the 357-based materials, see Figs.4.20 & 4.26. The mean values of the initial and minimum potentials, Table 4.4, were -772±5mV and -985±30mV.

4.8.3 DOUBLE CYCLE POLARISATION (20mV/min)

The DCP curve produced at a scan rate of 20mV/min on 2124 alloy, Fig.4.46(a), was similar to that observed for other materials. An inflection was visible in both reverse scans and the protection potential occurred well above the corrosion potential on the second cycle due to the fact that E_{corr} moved to more negative values, (by ~300mV). This produced a clearly defined passive range and pitting potential on the second forward scan, which did not appear on the first cycle. The characteristic potentials are reported in Table 4.5. Good reproducibility may be seen between values for E_{pit}, E_{prot} and E_{corr}, -748±10mV, -902±5mV and -1047±20mV respectively. The hysteresis area was very large, being 375±45μC.

The microstructure following DCP testing is illustrated in Fig.4.46(b). There are small corrosion pits which are elongated in the direction of cold-work. The pits have developed around the second phases, identified by EDS as Al_2CuMg and (CuFeMn)Al_6 (see Fig.4.13(c)&(d)). Evidence of attack at the grain boundaries is also apparent.

4.8.4 CORROSION MORPHOLOGY

After corrosion for 1 day, there was little evidence of attack on 2124 alloy. However, following 3 days immersion, the corrosion became more evident and was associated with (CuFeMn)Al_6 second phases, Fig.4.47(a). The Al_2CuMg phase was rarely attacked. After immersion for 1 week, the specimen surface was covered with small corrosion pits, Fig.4.47(b). The pits had grown around the second phases, thereby loosening and causing them to fall away. The remainder of the surface had a dimpled appearance. After 3 weeks, the pits had become larger and the specimen surface appeared to have been grooved in the direction of cold-work, Fig.4.47(c). Examination of cross-sections made through the material after 3 weeks immersion showed that the corrosion pits had propagated to between 15-35μm with an average depth of 25μm, Fig.4.47(d).

4.9 CORROSION STUDIES ON CARBON-REINFORCED 2124 ALLOY

4.9.1 OPEN CIRCUIT POTENTIAL

The changes in the OCP for samples of 2124-C were similar to those seen for the materials previously described. The initial potential of ~-749±20mV was maintained for a little less than 1 hour, before declining to a minimum potential of ~-923±25mV. The values of E_{init} and E_{min}, are recorded in Table 4.4.

4.9.2 DOUBLE CYCLE POTENTIAL (20mV/min)

The DCP data for specimens of 2124-C were similar to those produced for the unreinforced alloy, see Fig.4.46(a), and are listed in Table 4.5. With

the exception of E_{corr}, which had values of -958±40mV, E_{pit} (-705±10mV), E_{prot} (-854±10mV) and the hysteresis area (190±5μC), gave excellent reproducibility between tests.

The microstructure showed that most corrosion had occurred at the fibre-free regions, Fig.4.48(a), where the second phases of Al_2CuMg and $(CuFeMn)Al_6$ were present, Fig.4.48(b). The micrograph illustrates that part of the Al_2CuMg phase has become loosened by the surrounding corrosion and has fallen away. Areas of attack around the fibres were found, and this was further evidenced by microscopy of cross-sections through the corroded material, Fig.4.48(c). The depth of the attack was found to range from ~25-140μm, the mean depth across the surface being 70μm.

4.9.3 GALVANIC COUPLE

The galvanic current flowing between a specimen of 2124 alloy and several tows of carbon fibres was measured over a period of 2 hours. The results are reported in Table 4.7. During this time a constant current of 320μA was attained. Using the equation in section 4.4.4, the corrosion rate, was calculated assuming an electrochemical equivalent, k, of $0.1004 g.C^{-1}$ for 2124 alloy. The rate was $3.6 mm.yr^{-1}$.

4.9.4 CORROSION MORPHOLOGY

The 2124-C specimen which had been corroded for 1 day showed that the fibre regions had not experienced much corrosion, with only a few small corrosion pits forming between the fibres. This is illustrated by Fig.4.49(a), which also shows large circular areas of corrosion film

deposited on the surface. Preferential attack occurred at the intermetallic phase identified as (CuFeMn)Al_6, Fig.4.49(b), see ED results, Fig.4.32(b). The Al_2CuMg phase was not attacked.

After 3 days corrosion there was still no evidence of attack at the Al_2CuMg phase, but more small corrosion pits were visible in the matrix regions, Fig.4.50(a). In some fibre-rich regions, the matrix had been corroded slightly and a white phase at the fibre-matrix interface was evident, Fig.4.50(b). This phase was too small for an accurate determination of its composition but EDS analysis, Fig.4.50(c), showed the presence of aluminium and copper only.

Following immersion for 1 week, most corrosion still occurred around the second phases, including the Al_2CuMg phase, in the fibre-free regions. As Fig.4.51 shows the corrosion had loosened the phases and most of them had fallen away from the material. The fibre regions were relatively unattacked in most areas and they were similar in appearance to the 3 day corroded samples.

The corrosion after 3 weeks had become more extensive and much of the matrix had been removed to expose bare fibres, Fig.4.52(a). No evidence of the second phases in the matrix remained due to the degree of attack. The matrix regions surrounding the white phase at some of the fibre regions had also been severely attacked. EDS analysis, Fig.4.52(b) of the phase with most of the surrounding matrix corroded away, showed that only copper was present; the gold resulted from the coating process prior to SEM examination. Microscopy was conducted to determine the depth of corrosive attack. A depth of penetration ranging slightly between ~30-50μm was found.

4.10 CORROSION STUDIES ON SILICON CARBIDE-REINFORCED 2124 ALLOY

4.10.1 GRAVIMETRY

Weight loss measurements made upon 2124-SiC specimens are recorded in Table 4.11, together with corrosion rates. The data show a decrease in the rate of corrosion over the first week of immersion. During the remainder of the test however, the rate increased to a value of $12x10^{-3}$ $g.m^{-2}.h^{-1}$, which was comparable to the rate of attack following the first day of immersion.

4.10.2 OPEN CIRCUIT POTENTIAL

The OCP characteristics for two specimens of 2124-SiC were the same as for the 357-based materials and for the 2124 alloy *e.g.* Fig.4.20(a). A third specimen, however, produced a variation in OCP, Fig.4.53, where the high potential found during the initial stages persisted throughout most of the test. Towards, the later stages of immersion, there was a steady decline towards slightly more negative values, but no minimum was reached during the test. The mean initial and minimum potentials from the three tests are -729±20mV and -984±40mV respectively, Table 4.4.

4.10.3 DOUBLE CYCLE POLARISATION (20mV/min)

DCP test data on samples of 2124-SiC at a scan rate of 20mV/min are given in Table 4.5. The DCP curves followed the same pattern as other 2124-based materials, see Fig.4.46(a). The reproducibility between tests was excellent regarding E_{pit} (-726±5mV) and E_{prot} (-965±10mV). The

hysteresis area (332±35μC) and the corrosion potential (-1147±40mV), however, exhibited more variability.

The microstructure after DCP testing, Fig.4.54, shows a uniform distribution of corrosion pits encompassing a large number of the small (3μm) SiC particles. As a result of this corrosion many of the SiC particles and second phases ($CuAl_2$ and $(CuFeMn)Al_6$) had become loosened from the matrix and subsequently fallen away.

4.10.4 CORROSION MORPHOLOGY

After immersion of 2124-SiC for 1 day the corrosion was very slight. Examination in the SEM, Fig.4.55(a) revealed tiny corrosion pits at the silicon carbide particles and the second phase particles of $CuAl_2$ and $(CuFeMn)Al_6$. The degree of attack did not change visibly over 3 days, but after 1 week the corrosion pits had increased in size, Fig.4.55(b). The greatest change occurred between 1 and 3 weeks immersion. Much of the matrix surrounding the particles and second phases had been corroded away, Fig.4.55(c), although some particles and second phases still remained held by the matrix below. In regions where large corrosion pits had developed, the particles had fallen away. Measurement of cross-sections of corroded specimens after 3 weeks immersion showed that the average pit depth was ~25μm with a variation of depths between 10-40μm being found. Fig.4.55(d) is an example of a cross-section through a pitted region.

4.11 CORROSION STUDIES ON COMMERCIAL PURITY ALUMINIUM

4.11.1 GRAVIMETRY

Weight loss and corrosion rate data on aluminium specimens are given in Table 4.12. These show that the rate of attack diminishes with immersion time, the corrosion rate reaching an almost constant level of 4.0×10^{-3} $g.m^{-2}.h^{-1}$ after 1 week.

4.11.2 OPEN CIRCUIT POTENTIAL

Commercial purity aluminium experienced variations in potential during natural immersion similar to that illustrated in Fig.4.20(a) for 357 alloy. The mean values of E_{init} and E_{min}, Table 4.4, were found to be -787±15mV and -1143±10mV respectively.

4.11.3 DOUBLE CYCLE POLARISATION (20mV/min)

The DCP curves were of the same form as those recorded on aluminium single crystals, Fig.4.5, and had similar features to those observed for 357-Saf, Fig.4.42(a). In particular E_{pit} was recorded on the first cycle also, being closely similar to the pitting potential on the second cycle.

The corrosion potential was found to be the most reproducible between tests, with a value of -854±10mV. The pitting potential (-770±20mV) and hysteresis area (145±20μC) gave reasonable agreement, whilst the protection potential was more variable, with a value of -858±45mV.

Corrosion occurring as a result of the DCP test took the form of large corrosion pits up to ~100μm in diameter, thereby encompassing a large

number of the (AlSiFe) phases, Fig.4.56. Evidence of small corrosion pits around the particles may also be seen.

4.11.4 CORROSION MORPHOLOGY

The nature of the attack during the first week of immersion was similar to that for the 2124 alloy, *i.e.* it was mostly located around the second phases. However, in aluminium, the phases (AlSiFe) were not loosened by the attack and remained visible after 1 week, as Fig.4.57(a) illustrates.

Following corrosion for 3 weeks, the surface was covered in small pits, some of which contained tiny particles of the second phase. Larger particles of the second phase remained held by the aluminium, as shown in Fig.4.57(b).

4.12 CORROSION STUDIES ON CARBON-REINFORCED SUPER PURITY ALUMINIUM

4.12.1 OPEN CIRCUIT POTENTIAL

Changes in OCP recorded over 3 weeks for Al-C, were similar to those reported for a sample of 357 alloy, see Fig.4.20(b), *i.e.* the potential, once it had reached a minimum, remained there for the rest of the experiment. Values of the initial potential (-772±5mV) and the minimum potential (-1088±50mV) for the three samples tested, are recorded in Table 4.4.

4.12.2 DOUBLE CYCLE POLARISATION (20mV/min)

The DCP curve obtained on Al-C MMC, Fig.4.58(a), shows considerable difference between the shape of the hysteresis loop in the first and second cycles. During the first cycle the current density increases dramatically from the corrosion potential. At the second cycle, E_{corr} becomes depressed and a marked passive range and well-defined E_{pit} become evident. The increase in current density then occurs at E_{pit} as would normally be expected. The pitting potential (-775±5mV) was very reproducible between tests but the corrosion and protection potentials were rather more variable, with values of -1054±65mV and -900±90mV respectively. The hysteresis area was 145±30μC.

The microstructure after the DCP test, Fig.4.58(b) showed that pitting had occurred, mainly in the matrix-rich regions. SEM examination illustrated that the aluminium had been attacked in a crystallographic fashion to expose "steps" which were perpendicular to each other. Microscopy of cross-sections through the material indicated that the corrosion pits ranged from ~20-200μm across the section, with a mean value of 80μm.

4.12.3 GALVANIC COUPLE

The galvanic current measured over a 2 hour period between a sample of commercial purity aluminium and several tows of carbon fibres, was 260μA. The corrosion rate calculated using the equation in section 4.4.4, was 2.8mm.yr^{-1}, assuming an electrochemical equivalent, k, of 0.093gC^{-1} for aluminium. The results of corrosion rate and galvanic current are listed in Table 4.7.

4.12.4 CORROSION MORPHOLOGY

Following immersion for 1 day, the Al-C material exhibited little corrosion, pits only becoming evident after 3 days. The pits formed in the matrix-rich areas, Fig.4.59(a), the rest of the surface remaining unattacked. After immersion for 1 week, there was clear evidence of corrosion around the fibres and in some regions the attack had taken a crystallographic form, Fig.4.59(b).

Corrosion after 3 weeks immersion was more severe showing extensive attack of the aluminium around the fibres, Fig.4.60(a). The fibre-free regions were also slightly attacked, the corrosion taking the form of shallow pits. In some fibre areas, a large amount of internally trapped corrosion products were present, Fig.4.60(b). Examination of cross-sections showed that corrosion of the aluminium between fibres had occurred to a mean depth of ~80μm, the depth varying between 50-150μm across the surface.

CHAPTER 5

DISCUSSION

This chapter begins with an assessment of the various corrosion techniques which we have applied to metal matrix composites (MMC) and unreinforced alloys. A comparison of the electrochemical methods is made in section 5.2 and this is followed by a discussion of the usefulness of a double cycle polarisation (DCP) test for predicting the corrosion behaviour of MMC materials. A treatment of the corrosion characteristics of the materials are given in section 5.3, with reference to the type of reinforcement, the role of second phases, the composition of the matrix and, finally, the effect of the composite fabrication route.

5.1 GENERAL OBSERVATIONS OF THE CORROSION TESTS

5.1.1 GRAVIMETRY

The usefulness of applying gravimetric (weight loss) tests to the unreinforced metals and a selection of the MMC materials in this investigation was limited. Whilst all unreinforced metals and two MMC (357-Nic and 2124-SiC) produced weight losses, two other composites (357-C_L and 357-Saf) gave weight gains (see Tables 4.3, 4.6 & 4.8-4.12).

In general, weight losses recorded on unreinforced alloys, which ranged between ~2 to 6$g.m^{-2}$ for the various alloys, were in good agreement with those found by Nisancioglu and Holtan (1979) for a number of aluminium alloys immersed for times of up to 50 days.

The fact that the 357-C_L composite experienced a weight gain rather than a weight loss may be explained by reference to microstructural studies of

corroded specimens. This indicated that the volume expansion which accompanies the formation of internal corrosion products, causes stresses to be developed in the material. Thus the stresses initiate cracking (see Figs.4.31(a) & 4.32(b)), the fibre/matrix interface being the path of least resistance for the propagation of the cracks. The build-up of corrosion products within the crack, therefore, off-sets any weight loss due to corrosion. Indeed, microstructural investigations of cross-sections through the corroded material, Fig.4.32(d), showed evidence of corrosion together with the retention of corrosion products deep within the composite. This was noted also by Aylor *et al* (1984) and Evans and Braddick (1971) in corrosion studies of carbon-reinforced aluminium alloys, who reported that degradation of the composites resulted from internal stresses created by the corrosion products. The progressive decrease in the rate of weight gain observed over a three week period, (Fig.4.25), was probably due to an increasing thickness of corrosion product acting as an increasingly effective barrier to ingress of the corrosive solution.

The weight gain observed on corroded 357-Saf composite could not, however, be related to the presence of internal corrosion product, since the pits which formed on the surface were hemispherical and the corrosion products within them easily removed by the cleaning process. It is our contention that the fibres may have absorbed the corrosive solution during immersion, as noted by Nath and Namboodhiri (1988) for mica particles in an aluminium alloy. Support for this view was obtained by immersing specimens of 357-Saf in distilled water, a liquid in which the matrix would not be susceptible to pitting, but in which the fibres would still be able to hydrate. A substantial weight gain was noted after 24 hours immersion (~45g.m^{-2}) for specimens of 357-Saf, Fig.5.1. In contrast, 357-Nic used as a control experienced only a very small weight gain

(~5g.m^{-2}), possibly due to traces of water being trapped in pores and crevices within the material. This experiment confirmed that Saffil fibres will hydrate on immersion in an aqueous solution and it is feasible that with longer immersion time the extent of internal hydration due to a "wicking" effect in the fibres will be greater and make it more difficult for the fibres to dry out.

Returning to the materials which produced weight losses, the most notable feature was that the 357-Nic composite gave a smaller weight loss than the unreinforced 357 alloy (2.53g.m^{-2} compared with 6.15 g.m^{-2}), see Tables 4.3 & 4.8. A contributory factor to the apparent low weight loss of the composite was that the total area of the specimen exposed during the test was used in calculating the weight loss rather than the true area of exposed matrix. Hence taking the volume fraction of fibres (~50%) into account, the weight loss for 357-Nic becomes ~5g.m^{-2}, which is slightly less than the weight loss of the alloy. In addition, microstructural studies of cross-sections through the corroded materials showed that the MMC had undergone more extensive attack than the alloy indicating that its measured weight loss must be lower due to the entrapment of internal corrosion debris.

This argument cannot explain the higher weight loss of 2124-SiC composite (5.98g.m^{-2}) compared with the corresponding unreinforced alloy (5.07g.m^{-2}), although it is possible that the difference in weight loss is insignificant considering the error involved in their measurement (~±1g.m^{-2}). However, the microstructure of the corroded 2124-SiC could be related to the weight loss data. Corrosion attack was initiated around the SiC particles and led to the eventual detachment of the reinforcement in pitted regions, Fig.4.55(c). These observations are in accord with the

rate of weight loss for the 2124-SiC, Table 4.11, which shows a reduction in corrosion rate over the first week of immersion, but a doubling between 1 and 3 weeks, consistent with the growth of large pits and subsequent loss of reinforcing particles.

In summary, the success of gravimetric tests on the composite materials was limited, 2124-SiC being the only MMC which did not appear to retain either corrosion products or corrosion solution after removal and cleaning.

5.1.2 OPEN CIRCUIT POTENTIAL

The results of open circuit potential (OCP) measurements showed that all materials followed essentially the same trends. A high initial potential was found in all cases, and this lasted for ~1 hour, fluctuating around an almost constant potential. After the first hour, there was generally a sudden decline in the OCP to more negative values, a minimum potential being reached after ~4-6 hours. These first stages of the test were quite reproducible, although the latter stages were less so with the OCP attaining a potential between the initial and minimum potential value.

Changes in the OCP have been characterised by Nisancioglu and Holtan (1978a & 1979), as consisting of four distinct regions, as discussed in Chapter 2 and illustrated in Fig.2.4. Region I, pit initiation, corresponds to the first minute of immersion, where the potential reaches a value above the pitting potential. This region was not recorded in tests conducted during this study because it lasted for less time than the data sampling period of 1 minute.

Following initiation a quasi-stationary potential was reached in region II, which Nisancioglu and Holtan (1979) related to pit propagation. Hence this must be the pitting potential, E_{pit}, which corresponded to the initial potential, E_{init}, recorded during our tests. As with our findings, Nisancioglu and Holtan noted potential oscillations in region II, as did Richardson and Wood (1970) and Wood *et al* (1974), who attributed the oscillations to a constantly changing ratio of the anode to cathode area. As a pit initiated, it would expose fresh metal which is anodic in nature. This would be accompanied by a surge of potential in the negative direction and as cathodic activity rapidly established itself, the potential would become more positive again. As more pits initiate, the fluctuations in potential would continue but the OCP would decline as the ratio of the anodic to cathodic area increased. The decline in potential corresponds to region III in the model of Nisancioglu and Holtan (1978a & 1979). They attributed the downward trend of potential to the reduction in cathodic area, which is consistent with our findings where a minimum potential was reached approaching the bare metal potential of aluminium, -1.2V (SHE) as reported by Lepin and Kadek (1966). The presence of active pits would polarise the surface to more negative potentials. The area of pits would thus increase and the cathodic area, which supports the anodic reactions would correspondingly decrease. Eventually, the cathodic current would be reduced to zero and, therefore, the anodic reactions could no longer be sustained. At this point repassivation of the pits would occur. Hence we conclude that the potential at which anodic reactions cease must relate to the protection potential, below which pitting cannot occur. The minimum potential E_{min}, must, therefore, be the protection potential, E_{prot}.

During the later stages of immersion (region IV), the OCP was found to increase slightly and maintain a constant voltage for the remainder of the test. Nisancioglu and Holtan (1978a & 1979) identified this potential as the protection potential. However, we believe it to be more likely that passivation occurs at the minimum potential in region III, where pitting stops and, that in region IV, the potential moves to a constant value generally within the passive range, *i.e.* between the pitting and protection potential. In accord with this, our study showed that the latter stages (region IV) were rather less reproducible, a feature also noted by Wood *et al* (1974) and, although a constant potential was usually attained following region III, its position was variable. Generally, the potential did one of three things;

(i) it remained at the minimum potential (E_{prot}), or
(ii) it returned to the high initial potential exhibited during the first hour of the test (E_{pit}), or
(iii) it attained a potential between the initial and minimum potential (within the passive range).

These differences in behaviour are not surprising considering the statistical nature of pitting. Indeed, the values of the OCP recorded by a variety of authors on super-pure aluminium and collected by Nisancioglu and Holtan (1979) show that for immersion times ranging from 100 minutes to 32 days, the OCP can attain a value anywhere between -810mV and -1200mV.

To summarise this section of the work on electrochemical measurements, it has been clearly demonstrated that both pitting potentials and

protection potentials can be determined from a study of OCP characteristics.

5.1.3 DOUBLE CYCLE POLARISATION

The results of double cyclic polarisation (DCP) tests showed that, with two exceptions, the pitting potential was much more clearly defined during the second polarisation cycle than during the first. For most materials, a rapid increase in current density occurred at the corrosion potential in the first cycle, indicating that the material was freely pitting at the corrosion potential. This feature has been noted also by Nath and Namboodhiri (1988) in studies on a mica-reinforced aluminium alloy and it led them to consider the corrosion potential as representing the pitting potential. Furthermore, Szklarska-Smialowska (1986) reported that in solutions which were aggressive to the material, pitting often occurred at potentials scarcely more positive than the corrosion potential. This was exhibited by our materials, such that when the potential was increased above E_{corr}, the current also increased. Measurements showed also that the OCP (or free corrosion potential) varied substantially for all materials, (*e.g.* from ~-720 to -1150mV over a few hours) and that a rapid increase in the current density at the corrosion potential should not be assumed to represent the pitting potential.

However, as demonstrated with the double cycle polarisation test, the corrosion potential was depressed on the second cycle, thereby allowing the pitting potential to be clearly defined on the second cycle. The general features of the DCP test may be summarised as follows;

(i) the corrosion potential was always depressed on the second cycle,

(ii) there was a clear passive range in the anodic part of the second cycle and a clearly defined E_{pit},

(iii) the anodic part of the reverse scans on the first and second cycles were similar and for some materials, an inflection was found, and finally

(iv) the cathodic part of the reverse scans on the first and second cycle was always depressed (*i.e.* the current density at a given potential was lower during the first cycle than on the second).

The different features of the DCP curve may be explained with reference to the schematic representation, potential versus current density, shown in Fig.5.2.

On immersion the pits were active, as shown by the initial high OCP measurements, and the corrosion potential was therefore close to the pitting potential. Hence, specimens became freely pitting during initial immersion prior to polarisation. During the first forward cathodic scan (AB), the pits, although cathodically polarised, were not rendered inactive due to their occluded nature. Thus during the anodic part of the first anodic scan (CD), the already established pits were actively driven by being anodically polarised. On reversal of the potential through DEF, the pits were first cathodically polarised and then deactivated by formation of a passive film inside the pits. The cathodic part of the first reverse scan (FGH) was at a higher current density than the cathodic part of the first forward scan (AB), indicating that the anodic component of the net current in FGH was less than that in AB. This implies that the pits which were active in AB were now passivated.

During the forward scan of the second cycle (HIJK), the corrosion potential became substantially depressed because the material was now passivated, to give a clearly defined passive range (JK). At K, film breakdown occurred leading to pitting. The second reverse scan (LMNOP) was similar to the first reverse scan (DEFGH), implying that the mechanism of pit passivation is the same.

Hence with MMC materials, the presence of many pores and crevices will provide an abundance of sites at which pitting can initiate. These pits will continue to grow during the forward cycle of the first polarisation scan, which is why a clearly defined pitting potential is not visible on the first cycle. This demonstrates the usefulness of the DCP test for those materials where the pitting potential cannot be determined from a simple cyclic polarisation test.

(a) Sensitivity of the DCP Test

DCP tests conducted on single crystals of aluminium cut at a variety of orientations illustrated that the technique was not sensitive to changes in the crystallographic orientation and the values of pitting, protection and corrosion potentials did not vary between samples beyond the normal scatter expected in tests on the same material, Table 4.2. This result may be explained by considering the mechanism of pit initiation and propagation. Whilst the mechanism of pit initiation is not well understood, there is evidence that pitting is associated with the breakdown of the passive film. If, therefore, the film is not epitaxially related to the crystallographic orientation of the underlying aluminium, no effect of orientation would be expected. With regard to pit propagation,

this would be controlled by processes occurring within the pit, *e.g.* mass transfer within the corrosive solution. Hence, pit propagation would also be expected to be insensitive to the crystallographic orientation of the aluminium. Nevertheless, the DCP method was sufficiently sensitive to detect effects due to the alloying elements, reinforcement type and manufacturing process and thus provided a means for comparing potential data of different MMC materials.

(b) Effect of Scan Rate

The effect of applying a slow (2mV/min) scan rate to the 357-based materials instead of the generally adopted 20mV/min rate highlighted a number of interesting features. The most obvious difference related to the pitting potential. Firstly, for 357 alloy (Fig.4.22a) and 357-Saf MMC (Fig.4.43a), the pitting potential was found to be ~9mV more negative than that recorded at the faster scan rate, see Table 4.5. Secondly, 357-C_L and 357-Nic materials did not exhibit a pitting potential on either the first or second potential cycles, a rapid increase in current density occurring at the corrosion potential in both cases, see Fig.4.29(a).

Regarding 357 and 357-Saf materials, the higher value of the pitting potential at the faster rate was due to the "lag" in potential associated with the faster potential scan, *i.e.* potentials were recorded at more positive values than those at which they actually occurred. This is in agreement with Broli and Holtan (1973), who reported that the pitting potential for aluminium was dependant upon the scan rate and became more negative as the scan rate was reduced. Freiman and Khartinova (1972) also reported that pitting potentials measured on steels were affected by the rate of scan in polarisation tests. Indeed, they found that

scan rates of <0.12V/h (2mV/min), gave unreliable values of the pitting potential.

In the case of the 357-C_L and 357-Nic materials, the absence of a pitting potential on either cycle can be related to microstructure. Microscopy of cross-sections through the corroded surface (whether 3 weeks corrosion, Fig.4.32(d) or DCP tests, Fig.4.29(d)), showed that the depth of attack was more severe for these materials than for other systems and was channelled by the fibres to form long, narrow corrosion pits deep within the composite. It is possible that the factors discussed earlier, which cause the corrosion potential to lie close to the pitting potential, may be enhanced at a slower scan rate. Thus pits which were initiated prior to polarisation continue to propagate deep within the composite during the anodic part of the first forward scan. It therefore follows that at the slower rate more extensive internal attack could occur due to the longer time period of the test and that pits would remain active during the cathodic part of the first reverse scan and the second forward scan. In support of this, the DCP curve at the slower scan rate, Fig.4.29(a), showed that the cathodic part of the second forward cycle occurred at higher current densities (~10x) than that for the faster rate, Fig.4.27. Consequently the situation was the same as that normally experienced during the first cycle, *i.e.* pits were active at the corrosion potential on the second cycle, and hence the pitting potential was not defined.

Scan rate effects were noted by Wilde (1972) and Syrett (1977), who suggested that the protection potential was related to the extent of propagation and showed that at slower scan rates E_{prot} moved to more negative values for stainless steels. However, our experiments on composite materials and the parent alloy showed no such relationship,

and the protection and corrosion potentials were not significantly different for the two scan rates, taking into account the scatter in results between tests. Broli and Holtan (1973) also reported a dependance of the protection potential upon the scan rate although the effect was small, the protection potential passing through a maximum at a scan rate of 10mV/min. This may account for the similarity in E_{prot} recorded at the two scan rates in our tests, in that the protection potential at the 2mV/min rate falls on one side of the maximum E_{prot}, whilst the protection potential at 20mV/min falls on the other.

It has also been suggested (Broli and Holtan, 1973) that the scan rate affects the hysteresis area, in this work the area contained within the second cycle. They believe that this was due to the absence of electrochemical equilibrium and they showed that the area was smaller at a slower scan rate and did not occur at all in a stationary polarisation test. Our tests at slower rates showed smaller hysteresis areas for 357-C_L and 357-Nic, and larger areas for 357-Saf and 357, see Table 4.5 (the scatter in results means that the difference between the two rates is not significant), but no relationship between scan rate and hysteresis area could be established.

It is apparent also that a slower scan rate is not always desirable for the purposes of assessing MMC for pitting corrosion using the DCP method, particularly with continuous reinforcements where the pitting potential cannot be obtained from either the first or second polarisation cycle.

(c) The Inflection Potential

An inflection potential occurred in the reverse potential scans of polarisation tests on all materials, with the exception of 357-C_L and 357-

Nic, *e.g.* Fig.4.27. As discussed in the Chapter 2, the point of inflection has been related with the protection potential (Otani 1988), although in Chapter 4 we have shown that the protection potential is more accurately defined as the intersection between the forward and reverse scans, see Fig.4.2(a). Moreover, Nisancioglu and Holtan (1978b) noted during studies on aluminium alloys that the inflection potential was close to the pitting potential. They considered that the pitting potential was associated with changes in the corrosion mechanism such that at high current densities (*i.e.* above E_{pit}), corrosion occurred on a macroscopic front to form large rounded pits, whereas at low current densities (*i.e.* below E_{pit}), corrosion occurred on a microscopic level to produce crystallogaphic facets. Such mechanistic changes at high and low current levels were noted also by Richardson and Wood (1970) and Wood *et al* (1974). Their findings would suggest that the inflection potential in the reverse scan is related to the pitting potential on the forward scan, with E_{infl} being more negative than E_{pit} owing to the "lag" introduced by the potential scan. Thus it is possible that E_{infl} may also correspond to a change in the corrosion mechanism from one of macroscopic attack above E_{infl}, to a slower crystallographic type of attack below.

As noted earlier, materials 357-C_L and 357-Nic did not exhibit an inflection potential, which on the basis of the above theory would suggest that corrosion proceeded on a macroscopic front until passivation of the pits occurred at E_{prot}. This would then account for the extensive internal corrosion which occurred in these materials. However, further work is required to confirm such a relationship between the point of inflection and the change in corrosion mechanism.

5.1.4 GALVANIC COUPLES

Measurement of the galvanic current flowing between the matrix metal and bare fibres revealed that couples containing carbon fibres produced the largest galvanic current and consequently the fastest corrosion rate. The semi-conducting Nicalon fibre coupled to 357 alloy gave a corrosion rate which was an order of magnitude lower than for the carbon fibre. These results are not surprising considering the superior electrical conductivity of the carbon fibre.

Comparison of the corrosion rates with the maximum pit depth produced by simple immersion for 3 weeks (recorded in Table 5.1) showed a different ranking order compared with that provided by the galvanic corrosion rates, 2124/C having the second fastest galvanic corrosion rate but the smallest pit depth. Hence it is evident that other factors other than the galvanic interaction between fibre and matrix are contributing to the corrosion rate of the MMC.

One such factor concerns the presence in some MMC, of a layer of aluminium carbide between the fibre and matrix. Indeed evidence has been presented showing that the incorporation of carbon fibres into an aluminium matrix by squeeze casting frequently results in the formation of aluminium carbide (Figs.4.17 & 4.18), as shown by Yang and Scott (1991a) in their studies on 357-C fabricated by liquid metal infiltration (LMI). Thus 2124-C and 357-C_S, both fabricated by squeeze casting, are also likely to contain aluminium carbide. This phase readily hydrolyses and accelerated corrosion at the fibre/matrix interface would be anticipated, giving more extensive attack than that indicated by measurement of the galvanic current between fibre and matrix.

The extensive pits found in 357-Nic cannot be attributed entirely to the presence of carbide although it may have played some role in the corrosion reaction. In this composite the carbon needed to promote the carbide formation is present in the Nicalon fibre (Chapman *et al*, 1991), but to a much lesser degree than that in carbon-reinforced MMC. Thus we contend that an important factor governing pit depth concerns MMC fabrication, in particular the presence of voids left behind after manufacture. In support of this it was noted that the squeeze cast material was effectively free of voids compared with materials made by LMI, and the maximum pit depth was 50x less in 357-C_S than 357-C_L. Indeed the extensive pits in both 357-Nic and 357-C_L was related to poor infiltration which allowed the ingress of corrosive solution into the composite. Such pores would act as "wicks" for the solution and promote the hydrolysis of aluminium carbide within the MMC.

In addition to the above two factors second phases, in particular the iron-containing intermetallic phases, were seen to affect the corrosion of MMC. For example, the 2124-C MMC experienced attack at the (CuFeMn)Al_6 phase during the first few days of immersion, although corrosion at the fibre/matrix interface was not significant until more than 1 week of immersion. Hence, the depth of corrosion pits was much less in this material than for those materials containing extensive carbide.

It is evident, therefore, that measurements of galvanic current between the constituents of an MMC, matrix and reinforcement, do not by themselves give data from which the corrosion rate of a composite may be derived. Indeed, the presence of interfacial reaction products and matrix second phases, both of which may be affected by the method of fabrication,

will strongly influence the corrosion of the MMC. These secondary effects will be discussed in section 5.3.

5.2 ASSESSMENT OF THE CORROSION TESTS

5.2.1 COMPARISON OF OCP AND DCP TESTS

It has been established that the initial potential, E_{init}, and the minimum potential, E_{min}, derived from open circuit potential tests are equivalent to the pitting potential, E_{pit}, and the protection potential, E_{prot}, from DCP tests. Thus OCP measurements obtained under conditions of natural immersion can be used to assess the value of the DCP test.

Pitting potentials obtained from OCP and DCP tests are collated in Fig.5.3, the straight line representing a one-to-one correlation. For three of the materials, 357-Saf, 2124-SiC and Al-C, there appears to be excellent agreement between the results of the two tests. However, for the other seven materials, pitting potentials from the OCP tests are ~25mV more negative than those obtained from DCP tests. This may be due to the "lag" in potential associated with the DCP scan rate. This was reinforced by tests conducted at the slow rate (2mV/min) which showed that for the two materials exhibiting a pitting potential, the E_{pit} value was nearly 10mV more negative than at the 20mV/min scan rate. Therefore, provided that allowance is made for the effect of a potential scan rate, the DCP test pitting potential data agree reasonably well with those obtained from OCP tests.

With the exception of 2124 alloy, the materials could be separated into three groups according to matrix type. The materials based upon

unalloyed aluminium have the lowest pitting potentials, the 357-based materials and the 2124 alloy have intermediate potentials, and the 2124-based composites have the most positive values of E_{pit}. These differences in behaviour are related to the constitution of the matrix alloy, the effect of reinforcement and the method of fabrication, as will be discussed later.

Comparison of protection potentials from DCP and OCP tests, see Fig.5.4 where the straight line again represents a one-to-one correlation, shows reasonable agreement between data on seven MMC systems. With 357-Nic, Al and Al-C materials, poor correlations were found the OCP protection potential being ~200 to 300mV more electronegative than the DCP value. The more negative potential may be a function of the experimental technique in that it relates to the conditions necessary to repassivate the metal inside the growing pit, a point made previously by Wilde (1972) and by Syrett (1977).

Our results showed that the extent of attack was greatest after OCP tests and it was not surprising therefore to find that these protection potentials were more negative than those obtained from DCP tests. This accords with the findings of Wilde (1972) and Wilde and Williams (1971) who, noted in work on stainless steels that the protection potential was dependent upon the extent of corrosion, with lower values for more extensive attack. If, however, the protection potentials are considered from a materials point of view, the relationship between the degree of corrosion and the protection potential proposed by Wilde and Williams (1971) does not provide a fully consistent explanation. For example, the material which experienced the most extensive attack, 357-C_L, had one of the most positive values of E_{prot} whether derived from DCP or OCP tests.

Thus to progress the argument, we have to consider microstructural characteristics of the different materials, in addition to physical and chemical effects within the pits associated with the presence of corrosion products and chloride ions or hydrogen gas. In turn, these corrosion effects will be influenced by the presence of fibres and intermetallic phases. Indeed, as reported by Wilde and Williams (1971) and Nisancioglu and Holtan (1978c), the protection potential is characteristic of the potential at the bottom of a pit, and this is dependent upon the concentration gradient or ohmic potential inside the pit.

Examination of materials corroded for shorter immersion times showed that the sites of attack were essentially the same in OCP and DCP tests, *i.e.* at fibre/matrix interfaces and at intermetallic or other second phases in the matrix. There were, however, some differences in that the DCP test produced large individual corrosion pits with little corrosion of the surrounding surfaces, whereas specimens subjected to the OCP test experienced corrosion across the whole surface to differing extents which rendered individual corrosion pits less obvious.

The differences may be explained as follows. In the DCP test, the specimen is polarised to potentials which are far more positive than those occurring under conditions of natural immersion. This is evidenced by the maximum potential of ~-700mV reached in OCP tests compared with ~-500mV in the DCP tests. Thus pits, once initiated, are actively driven in the DCP test whereas, under the OCP conditions of natural immersion, pits are constantly being initiated and repassivated (after various degrees of propagation). Hence more corrosion sites are developed over the surface under OCP conditions. This would accord with the observations of Richardson and Wood (1970) who noted that the morphology and

distribution of pits, in the absence of an applied potential, depended upon the changing ratio of cathode-to-anode area, and that this in turn resulted in a more uneven size and distribution of pits. Under applied polarisation, the pits would be more evenly distributed and more uniform in size, as evidenced by the present study.

Thus it may be concluded that whilst the preferred sites of pitting are generally the same in the two tests, the density of active sites and the overall morphology of corrosive attack is different. This was confirmed from an examination of cross-sections through the corroded materials. Comparison of the maximum pit depth measured on a selection of MMC after OCP and DCP tests shows, Fig.5.5, that although the pits were much deeper after OCP tests, the trends were similar for both. This supports our contention that the DCP test is useful for determining the relative corrosion resistance of a variety of materials.

5.2.2 ASSESSMENT OF OTHER PARAMETERS TO CHARACTERISE CORROSION

The difference potential (E_{pit}-E_{prot}) as deduced from cyclic polarisation tests has been suggested by Wilde and Williams (1971) and Wilde (1972) as providing a measure of the extent of corrosive attack. They showed that difference potential values correlated well with the corrosion weight loss of stainless steels under natural immersion conditions. However, with aluminium alloys Nisancioglu and Holtan (1978b & 1979) indicated that the difference potential was not a useful parameter because the protection potential was found not to be a function of the amount of metal dissolution prior to pit passivation.

With regard to our studies on unreinforced aluminium alloys and the 2124-SiC composite (the only materials on which gravimetry was successful), the difference potential showed some correspondence with weight loss data, Fig.5.6, although there was no linear relationship between the two sets of data. Concerning composite materials, difficulties in carrying out sensible a gravimetric measurements precluded any possibility of correlating the data.

Turning to the question of hysteresis area, this is given by the area swept out by the voltage versus current density plot during a single cycle, and has been suggested by Walker and Rowe (1976) as being a measure of the extent of corrosion. The area is related to the power supplied to the specimen during formation of the loop, the larger the loop, the more extensive the corrosion.

Whilst the difference potential is also used as a measure of corrosive attack, the present results showed little correlation between this and the hysteresis area, Fig.5.7. This is not surprising since the hysteresis area is dominated by corrosion at high current densities and, as discussed in section 5.1.3(c), this is probably associated with a different corrosion mechanism from the low current density region associated with the difference potential. Of the two corrosion parameters, our view is that the difference potential is, in general, more useful, since a trend with weight loss data was found for unreinforced and SiC particulate-reinforced materials, (Fig.5.6). However, it is inadvisable to use it for fibre-reinforced metals without additional information, as evidenced by the low difference potential exhibited by the strongly corroding 357-C_L and 357-Nic materials.

5.3 CORROSION OF THE MATERIALS

5.3.1 EFFECT OF REINFORCEMENT

The type of reinforcement was found to play an important role in the corrosion of the metal matrix composites. For all materials studied, corrosion was evident at the reinforcement/matrix interface, some systems experiencing more extensive corrosion than others. The interfacial corrosion could be due to a number of factors. For example, pores and crevices could increase the number of local anodes at the fibre surface as suggested by Sedricks *et al* (1971). Alternatively, as noted by Otani *et al* (1988 & 1989), Friend *et al* (1990) and Pohlman (1978), galvanic currents may be arise between an electrically conductive reinforcement and the matrix. However, the corrosion of aluminium in salt water is caused by the presence of chloride ions and for attack to occur, chloride ions must penetrate through the protective oxide film as discussed in Chapter 2. Interfaces would provide a preferential site for the penetration of the chloride ions due to the impaired passivity of the oxide film in these regions. Once the chloride ions are in contact with the metal, corrosion can occur and this may be accelerated by the formation of a galvanic couple at interfaces between phases or materials of differing electrode potentials. The presence of fibres or particles at the alloy surface is likely to cause such a situation, thereby facilitating attack of the metal adjacent to the fibre where the oxide film is impaired. Thus corrosion at the interfaces between materials of differing electrode potentials may be a combination of firstly, film breakdown and secondly, galvanic corrosion. In support of this mechanism, the least severe attack occurred on Saffil (Al_2O_3) fibre-reinforced 357 alloy. It is possible that the continuity of the oxide film was enhanced across the surface of this material due to the

fibre and the surface oxide film being of similar composition. An additional factor which may account for the less severe interfacial corrosion of 357-Saf material is the absence of any galvanic contribution, owing to the non-conducting nature of the Saffil fibre. Clearly the galvanic effect has made a bigger contribution to the corrosion of the carbon fibre-reinforced materials, as demonstrated by the results of current measurements on fibre-matrix galvanic couples.

Paciej and Agarwala (1988) noted that corrosion in the interfacial regions of the 2124-SiC MMC could be a result of the high dislocation density produced around the particles by the thermal mismatch during fabrication. The dislocations can promote corrosion either because they provide regions of high residual stress or they act as sites for the precipitation of galvanically active phases. As mentioned above, the attack at dislocations and active phases may be initially attributable to defects in the passive film at these sites.

The pitting potential of 2124-SiC was more negative than that for 2124-C (-726mV and -705mV respectively as recorded from DCP curves). This is surprising as the presence of carbon fibres might be expected to render the matrix more susceptible to pitting than the less electrically-conducting silicon carbide particles. A contributory factor to the enhanced pitting susceptibility of 2124-SiC may be its lower volume fraction of reinforcement compared with 2124-C. Thus a larger area of matrix and consequently a larger number of potential pitting sites would be exposed during corrosion of 2124-SiC. In agreement with this, the pitting potential of 2124 alloy which contained no reinforcement (-748mV) was more negative than either of the two 2124-based MMC, indicating that it has a greater susceptiblity to pitting. However, the possibility that differences

in fabrication of the three materials, may have an an affect on the tendancy for pitting to occur should not be overlooked, a point which we shall return to later.

The geometry of the reinforcement also played an important part in the nature of the corrosion. In the case of continuous fibres, corrosion was channelled along the fibre, forming long corrosion pits which, in the case of the 357-Nic and more especially the 357-C_L composite, extended deeply within the material. The short Saffil fibres and silicon carbide particles did not influence the propagation of corrosion pits to such a great extent, since the pits in these materials were hemispherical and shallower than those in the continuous fibre-reinforced MMC. In fact with both 2124-SiC and 357-Saf materials, the pits after 3 weeks corrosion were of similar depths to those in the unreinforced alloys.

Crevices at the fibre-matrix interface also contributed to corrosive attack of the interface, although crevice corrosion is traditionally associated with the presence of oxygen, whereas our solutions were de-aerated. Rosenfeld and Marshakov (1964) reported, however, that the process may occur in corrosive solutions completely free of oxygen, due to changes in the character of the electrolyte within the crevice. They noted that the development of a "macrocouple", with the metal inside the crevice acting as the anode and the metal outside the crevice acting as the cathode, may cause acidification of the solution within the crevice, thereby accelerating corrosion.

One consequence of particular types of reinforcement and liquid metal fabrication processes is the formation of reaction products at the interface. In certain circumstances, this microstructural feature may severely

influence the nature of the corrosive attack. This is exemplified by studies on 357-C_L, where total penetration had occurred for one sample after immersion for only three weeks, due partly to the hydrolyses of aluminium carbide. Such attack was found to cause cracking at the fibre/matrix interface due to a "jacking" affect from the volume expansion of the internal corrosion products. Otani *et al* (1989) also observed cracking in this type of composite, although they attributed the severe internal corrosion to a galvanic action between fibre and matrix since no evidence of aluminium carbide at the interface was found. The less severe interfacial corrosion of the Saffil short fibre and SiC particulate-reinforced materials is due to the absence of aluminium carbide.

5.3.2 EFFECT OF MATRIX ALLOY

The elements present in the aluminium alloys had a pronounced effect upon the corrosion characteristics of the composite material, by not only affecting the alloy composition, but also by influencing the formation of certain intermetallic and second phases. However, the subject of second phases will be discussed in the following section

The most noticeable effect was that upon the pitting potential. Commercial purity aluminium gave an E_{pit} value of -770mV in DCP tests, which was ~15mV more positive than that recorded for single crystals of pure aluminium. The difference is very likely to be due to the presence of impurity phases containing iron since the electrode potential of iron is more positive than aluminium.

The 357 alloy-based materials had pitting potentials which ranged between -743mV to -763mV, all of which were more positive than the

pitting potentials of materials based upon unalloyed aluminium. The shift to more positive potentials is mainly due to the presence of silicon and also to iron found in the intermetallic phases in this material. The differences in the pitting potentials between composites may result from the presence of fibres and also the differences in the amount of iron contamination or, more generally, to a different fabrication route as discussed in the following section.

The 2124-based materials produced more positive pitting potentials than those recorded for 357-based materials. This is due to the presence of copper, a more electropositive metal compared with aluminium, as noted by Mueller and Galvele (1977). The fact that pitting potentials of the three 2124-based materials were significantly different and may again be related to the various manufacturing routes.

5.3.3 EFFECT OF SECOND PHASES

In addition to the aluminium carbide at the fibre/matrix interface, a variety of intermetallic phases were discovered which were found to promote corrosion of the surrounding metal.

The corrosion of the metal adjacent to the intermetallics is generally due to a microgalvanic action, the phase having a more electropositive potential than the surrounding material and thus acting as the cathode in the corrosion process. However, Nisancioglu and Lunder (1986) suggested that other factors had to be considered. In particular, the electrochemical properties of intermetallic and matrix, (such as the surface structure and composition of the matrix and phases) and the composition of the solution adjacent to the anodic and cathodic areas must be borne in mind. Also the

interaction may be affected by the ratio of the cathode/anode area, these being controlled by fabrication and secondary manufacturing processes. Murray *et al* (1967) noted that a contributory factor to the corrosion around intermetallics could be the less protective nature of the oxide film in these regions.

The 357 alloy contained three different phases - the silicon eutectic and the Fe_2SiAl_8 and $Al_8Si_6Mg_3Fe$ intermetallic phases. The silicon eutectic contributed little to the corrosion of the aluminium compared with the two intermetallics, although during longer immersion periods, corrosion was noticeable around the eutectic rods. The intermetallic phases initiated pits from the very early stages of immersion, the Fe_2SiAl_8 phase being the preferred corrosion site. This could be due to differences in the galvanic affect contributed by the two phases. The electrode potential of magnesium according to Polmear (1981) is ~-1.7V (SCE) and hence the $Al_8Si_6Mg_3Fe$ phase would be expected to be more anodic and closer to the electrode potential of aluminium than the Fe_2SiAl_8 phase. Consequently there would be less corrosion adjacent to the $Al_8Si_6Mg_3Fe$ phase.

The $FeSiAl_5$ phase commonly present in the 357-based composites proved to be detrimental to the corrosion properties, causing corrosion of the adjacent aluminium. This was especially evident in the 357-Saf material, where the alumina fibres were relatively passive compared with the Nicalon and carbon reinforcements. This observation would appear to be in contrast to the findings of Otani *et al* (1988 & 1989) who reported that the $FeSiAl_5$ phase in 357-based composites appeared to inhibit pit propagation by acting as a barrier to the development of pits. In the 357-C_L MMC, the $FeSiAl_5$ needles appeared to cause corrosion of the

surrounding metal at a slightly earlier stage of immersion than the coexistent (FeSiAlCr) phase.

Regarding 2124 alloy and 2124-C MMC, the $(CuFeMn)Al_6$ phase located in these materials was found to have a more severe affect on the corrosion of the surrounding matrix than the Al_2CuMg phase. Corrosion occurred at the $(CuFeMn)Al_6$ phase during the first day of immersion, whereas the $CuAl_2Mg$ phase remained relatively inactive as regards the corrosion process until more than 3 days after immersion. In the 2124-SiC MMC however, the $(CuFeMn)Al_6$ and $CuAl_2$ phases were attacked equally which suggests that the magnesium in the Al_2Cu phase renders the intermetallic phase less active. This accords with the reported electrode potentials of -1.00V and -0.53V (SCE) (Polmear 1981) for the $CuAl_2Mg$ and $CuAl_2$ phases respectively. Thus it follows that $(CuFeMn)Al_6$ must also have a electrode potential close to -0.53V and the more cathodic potential in this case is probably due to the presence of iron.

In the case of the 2124-C composites, a white phase appeared around some of the fibres after 3 days immersion, the phase not having been visible prior to corrosion. EDS analysis of the phase was difficult due to its small size, but showed the presence of aluminium and copper. After 3 weeks corrosion, much of the aluminium surrounding the phase had been corroded away and ED results now showed that only copper was present. It is possible, therefore, that the aluminium recorded in the ED spectra after 3 days was picked up from the surrounding aluminium matrix. This suggests that as copper was not found at the fibres in the uncorroded specimens, it must have been deposited during immersion. This accords with the findings of Summerson and Sprowls (1986) who noted that copper ions can be plated-out on an aluminium surface, thereby creating

small galvanic cells and intensifying pitting. This would also explain why the 2124-C did not exhibit extensive attack in the fibre regions until the later stages of immersion.

Regarding commercial purity aluminium, the (FeSiAl) phase also enhanced corrosion of the surrounding aluminium, probably due to a galvanic affect and to discontinuity of the oxide film.

In summary, all intermetallic phases present in the matrix were found to be detrimental to the corrosion resistance of the composite materials. Impurity phases containing iron were found to act as preferential initiation sites, due to their being cathodic to the surrounding aluminium. The magnesium-containing phases caused less severe attack since other their potential was closer to the adjacent matrix than the iron-containing phases. In all cases disruptions in the continuity of the oxide film may have initiated the localised attack, with the ensuing galvanic action causing propagation of the pits.

5.3.4 EFFECT OF FABRICATION

This investigation utilised materials manufactured by liquid metal infiltration (357-C_L, 357-Nic and 357-Saf), squeeze casting (357-C_S, 2124-C and Al-C) and powder metallurgy (2124-SiC). The unreinforced alloys also varied in their method of manufacture; the 357 alloy and aluminium had been conventionally cast and the 2124 alloy was in the T851 heat-treated condition. Some important microstructural features characterised the differences in manufacture and had important consequences with regard to corrosion behaviour.

Concerning the alloys, the corrosion propagated along the direction of stretching in the case of 2124 alloy. The corrosion of 357 alloy, however, followed regions of eutectic and intermetallic phase, this material not having undergone any secondary manufacturing processes which introduced directionality into the material. Pitting in aluminium was also non-directional, being centred around impurity phases.

As noted earlier, 2124-based materials gave widely different values of the pitting potential which may be attributed firstly to differences in the volume fraction of reinforcement and, secondly to the different methods of production. The 2124 alloy experienced intergranular attack and was found to gave the most negative value of E_{pit} (-748mV), indicating that it was the most susceptible material to pitting attack. This accords with the findings of Weisshaus *et al* (1980), who showed that an aluminium-copper alloy was more susceptible to pitting after heat-treatment. Galvele and De Micheli (1970) found that aged aluminium-copper alloys were susceptible to intergranular corrosion and attributed this to the differences in pitting potentials between the grain interior and the grain boundary. They noted that on precipitation-ageing the grain boundaries became depleted in copper and had a lower pitting potential than the grain itself. Also those aluminium-copper alloys which were sensitive to intergranular corrosion, had an overall pitting potential which was greater than that of the depleted zone, but less than that of the grain. Hence our heat-treated 2124 alloy experienced pitting at lower potentials than either of the non-heat-treated composites, 2124-SiC and 2124-C MMC.

The 357-C_L and 357-C_S composites comprised the same fibres and matrix, but were fabricated by liquid metal infiltration and squeeze casting respectively. Taking into account the scatter in results, data from DCP

and OCP tests gave similar values of E_{pit}, E_{prot} and E_{corr} for the two materials. However, studies of the microstructure after corrosion revealed that the 357-C_L MMC had corroded more severely, with cross-sections through the corroded material after 3 weeks corrosion showing the development of pits up to 6000μm deep compared with 300μm in 357-C_S. The nature of attack also differed; corrosion occurred almost uniformly across the 357-C_S material, but was more localised on the 357-C_L material, being located mostly at the edges of fibre tows. This was due to the fibres in the 357-C_L material being held tightly in tows by glass fibre wefts. During liquid metal infiltration the carbon fibres were restrained and consequently regions of poor infiltration resulted, particularly at the outermost regions of carbon fibre tows where the infiltrating metal has pushed the fibres more closely together. This was also observed in a similar composite by Yang and Scott (1991a). The edges of tows were thus regions of high porosity which allowed the corrosion solution to penetrate deeply within the composite to develop occluded pitting. The pores, together with the aluminium carbide at the fibre/matrix interface, had a "wicking" effect and consequently deep corrosion pits grew within the composites over a relatively short period of time.

The 357-Nic material which contained the glass weft experienced similar attack, with the fibre wefts also providing paths followed by the corrosion pits. The depth of attack in the 357-Nic composite was less than in the 357-C_L material which is believed to be due to the orientation of the glass wefts to the exposed surface, see Fig.5.8. Transverse fibre sections of 357-Nic material were studied, which contained glass wefts orientated longitudinally (parallel to the surface), as illustrated schematically in Fig.5.8(a). Hence as the cross-section through an exposed surface shows, Fig 5.8(b), tows of glass wefts exposed at the surface only extend a short

distance into the material, which limits the depth of corrosion at the glass/matrix interface.

The 357-Nic composite which did not contain the glass weft, corroded to the same depth as the 357-Nic material with the glass wefts, the corrosion occurring along the fibre/matrix interface. It is therefore evident that the depth of attack for specimens of 357-Nic containing glass wefts parallel to the exposed surface was controlled by corrosion at the fibre/matrix interface. However, it is reasonable to assume that sections of 357-Nic containing glass weftss perpendicular to the exposed surface would experience more extensive internal attack.

Thus it may be concluded that the presence of binders such as glass-fibre wefts which are not removed during the fabrication of MMC, can have a major influence on the corrosion properties of the MMC. Indeed, the materials which were fabricated by squeeze casting, contained no glass-binder, the reiforcing fibres being free to move during infiltration of the molten metal. This, combined with the higher pressures involved in squeeze casting, permitted the preform to be almost completely infiltrated, with virtually no residual porosity. Consequently, as the MMC based upon the 357 alloy reinforced with carbon fibres showed, the corrosion of the squeeze cast materials was less extensive than the same material fabricated by liquid metal infiltration.

CHAPTER 6

CONCLUSIONS

The conclusions arising from the corrosion test methods are firstly summarised, followed by those relating to the corrosion behaviour of the MMC.

6.1 CORROSION TEST METHODS

Simple immersion corrosion tests were conducted in parallel with an accelerated cyclic polarisation method to investigate the corrosion behaviour of MMC. On immersion, crevices and pores created by the presence of fibres permitted the formation of occluded corrosion pits, as evidenced by the initial high potential recorded in OCP tests. During the forward scan of a single cyclic polarisation test these pits remained active thus masking the pitting potential. During the reverse scan, however, pits became passivated so that if a second cyclic polarisation was performed immediately following the first a well-defined E_{pit} was found at the pitting potential. The double cyclic polarisation (DCP) technique, therefore, proved to be a valuable method of establishing accelerated corrosion data for MMC.

The occluded pitting effects were enhanced during DCP tests at a slow (2mV/min) potential scan rate. The increased time period of the test permitted extensive internal pitting and the pits were not rendered inactive, even by a second cycle. Thus slow scan rates are not always desirable.

The DCP test provided reproducible pitting and protection potentials, the data showing reasonable correlation with open circuit potential measurements.

Potentiostatic tests conducted on MMC showed that the protection potential, which some authors have related to the point of inflection in the reverse scan of a cyclic polarisation test, is better defined at the intersection between the forward and reverse scans.

Gravimetry could not be used as a comparative technique for MMC, as continuous fibre-reinforced MMC developed deep pits which entrapped corrosion products. In addition, the Saffil fibres were shown to hydrate in the solution. Both of these phenomena resulted in off-setting any weight loss occurring in the composites due to corrosion.

The extent of corrosion of fibre-reinforced MMC could not be predicted from polarisation data such as the difference potential (E_{pit}-E_{prot}), or the hysteresis area. This may be due to the differences in corrosion mechanisms which occur during the polarisation test.

Differences in the corrosion morphology were noted between specimens after DCP tests and those corroded during natural immersion for 3 weeks. Although the matrix surrounding the same microstructural features were attacked in both tests, DCP tests produced large individual corrosion pits, whereas OCP specimens experienced corrosion across the whole surface to differing extents. This results from the aggressive nature of the DCP test which polarises the specimen to more positive potentials than those reached under natural immersion.

6.2 CORROSION OF MMC

The microstructure of the MMC played an important role in the corrosion process, with attack being concentrated around features such as second phases or reinforcements. Discontinuities in the surface oxide film at these features may have permitted the ingress of chloride ions which, once in contact with the metal, initiated pitting. In some cases the pitting was enhanced by galvanic interactions between conductive reinforcements or second phases and the matrix. Needle-like $FeSiAl_5$ intermetallic phases were commonly found and these proved to be the most detrimental phase present in the 357-based MMC. The (AlSiFeCr) phase found in 357-C_L material also promoted corrosion but to a lesser extent. The (CuFeMn)Al_6 intermetallic detected in 2124-based MMC was associated with notable corrosion of the surrounding matrix during the first day of immersion, whereas the less active $CuAl_2Mg$ phase, did not result in appreciable galvanic corrosion until more than 3 days had elapsed.

The electrically conducting carbon fibre had the most severe effect on the corrosion of MMC compared with the other reinforcements. This was largely attributed to the presence of aluminium carbide at the carbon fibre/matrix interface, which readily hydrolyses and accelerates corrosion at the interfacial regions. Attack at the fibre/matrix interface within the Saffil-reinforced MMC was much less severe owing to the non-conducting nature of the fibre and also the absence of interfacial aluminium carbide. The Nicalon fibre-reinforced MMC also experienced fairly severe corrosion at the fibre/matrix interface, possibly due to the semi-conducting nature of the fibre, the presence of small amounts of interfacial aluminium carbide and the effect of fabrication.

The 357-C_L and 357-Nic MMC produced by liquid metal infiltration contained residual porosity between closely-packed fibres restrained by glass fibre wefts. The pores allowed ingress of the electrolyte, thereby accelerating internal corrosion. This, combined with a galvanic effect and the presence of aluminium carbide in the 357-C_L caused this material to suffer the most severe attack. The MMC fabricated by squeeze casting contained virtually no remnant porosity owing to the absence of the glass binder and the higher pressures involved. Hence the corrosion experienced by these materials was less severe.

REFERENCES

REFERENCES

Alexander, J.A., Cunningham, A.L. and Chuang, K.E., (1968), *Technical Report, AFML-TR-67-391*, Air Force Materials Laboratory, Wright-Patterson Air Force Base, Ohio.

Anderson, C-H. and Warren, R., (1984), *Composites*, 15, N°.1, pp. 16-24.

ASM Metals Handbook, (1972),*"Atlas of Microstructures of Industrial Alloys"*, 7, 8th edition, American Society of Metals.

ASTM G31-72, (1978), *Standard Recommended Practise for Laboratory Immersion Corrosion Testing of Materials*, pp. 869-880.

ASTM G5-78, (1978), *Standard Recommended Practise: Standard Reference Method for Making Potentiostatic and Potentiodynamic Anodic Polarisation Measurements*, pp. 816-826.

Aylor, D.M. and Kain, R.M., (1985), *Recent Advances in Composites in the United States and Japan,* ASTM STP 864, eds. J.R.Vinson and M.Taya, American Society for Testing Materials, Philedelphia, pp. 632-647.

Aylor, D.M. and Moran, P.J., (1985), *Journal of the Electrochemical Society*, 132, N°. 6, pp. 1277-1281.

Aylor, D.M., Ferrara, R.J. and Kain, R.M., (1984), *Materials Performance*, 23, N°.7, pp.32-38.

Bader. M.G., Clyne, T.W., Cappleman, G.R. and Hubert, P.A., (1985), *Composite Science and Technology*, 23, pp. 287-301.

Barnartt, S., (1976), *"Electrochemical Techniques for Corrosion"*, ed. R.Baboian, NACE, Houston pp. 1-10.

Bishop, H.E., (1974), *Journal of Physics D: Applied Physics*, 7, pp. 2009-2020.

Bond, A.P., Bolling, G.F. and Domian, H.A., (1966), *Journal of the Electrochemical Society*, 113, N°.8, pp. 773-778.

Brennert, S., (1937), *Journal of the Iron and Steel Institute*, 35, pp. 101-111.

Broli, A. and Holtan, H., (1973), *Corrosion Science*, 13, pp. 237-246.

Chadwick, G.A. and Yue, T.M.,(1989), *Metals and Materials*, 5, pp. 6-12.

Chadwick, G.A., (1990), *Proceedings of ECCMIV*, eds. J.Fuller, G.Gruninger, K.Schulte, A.R.Bunsell and A.Massiah,, Elsevier Science, Stuttgart, Germany, pp. 3-13.

Chandler, K., (1985), *"Marine and Offshore Corrosion"*, Butterworths and C°. Ltd., p. 952.

Chapman, A., Scot, V.D. and Yang, M., (1991), *Proceedings of ICCM8*, 19G, eds. S.W.Tsai and G.S.Springer, Sampe, California, pp.1-10.

Chiou, J.M. and Chung, D.D.L., (1991), *Journal of Materials Science*, 26, pp. 2583-2589.

Chou, T.W., Kelly, A. and Okura, A., (1985), *Composites*, 16, N°.3, pp. 187-206.

Clyne, T.W., Bader, M.G., Cappleman, G.R. and Hubert, P., (1985), *Journal of Materials Science*, 20, pp. 85-96.

Das, A.A. and Chaterjee, S., (1981), *The Metallurgist and Materials Technologist*, 13, pp. 137-142.

Dean, S.W., (1976), *"Electrochemical Techniques for Corrosion"*, ed. R.Baboian, NACE, Houston, pp. 52-60.

Evans, J.M. and Braddick, D.M., (1971), *Corrosion Science*, 11, pp. 611-614.

Fontana, M.G., (1987), *"Corrosion Engineering"*, 3rd edition, (1st edition 1967), McGraw Hill, pp. 51-59.

Foroulis, Z.A. and Thubrikar, M.J., (1976), *Electrochimica Acta*, 21, pp. 225-230.

Freiman, L. and Khartinova, L., (1972), *"Zaschita Metallov"*, 8, pp. 693-694.

Friend, C.M., Naish, C., O'Brien, T.M. and Sample, G., (1990), *Proceedings of ECCMIV*, eds. J.Fuller, G.Gruninger, K.Schulte, A.R.Bunsell and A.Massiah, Stuttgart, Germany, Elsevier Science, pp. 307-312.

Galvele, J.R. and de De Micheli, S.M., (1970), *Corrosion Science*, 10, pp. 795-807.

Gehring, G.A. and Peterson, M.H., (1981), *Corrosion*, 37, pp. 232-242.

Harris, S.J., (1988), *"Materials Science and Technology"*, 4, pp. 231-239.

Harris, S.J., (1989), *"Aluminium Alloys - Contemporary Research and Applications"*, 31, eds. A.K.Vasudevan and R.D.Doherty, Academic Press, pp. 255-294.

Hoar, T.P., Mears, D.C. and Rothwell, G.P., (1965), *Corrosion Science*, 5, pp. 279-289.

Hubner, W. and Wranglen, G., (1964), *Scandanavian Corrosion Congress*, Helsinki, pp. 60-69.

Karandikar, P.G. and Chou, T.S., (1991), *Journal of Materials Science*, 26, pp. 2573-2578.

Leckie, H.P., (1970), *Journal of the Electrochemical Society*, 117, pp. 1152-1154.

Lepin, L. and Kadek, V., (1966), *Corrosion Science*, 6, pp. 177-181.

Levi, C.G., Abbaschian, G.J. and Mehrabian, R., (1978), *Metallurgical Transactions A*, 94, pp. 697-711.

Lizlovs, E.A. and Bond, A.P., (1975), *Corrosion* , 31, N^0.6, pp. 219-222.

Lloyd, D.J., (1989), *Composite Science and Technology*, 35, pp. 159-179.

Love, G. and Scott, V.D., (1978), *"Journal of Physics D: Applied Physics"*, 11, pp. 1369-1376.

Mansfeld, F., (1981), *Corrosion*, 36, N^0.5, pp. 301-307.

Mansfeld, F., (1976), *"Electrochemical Techniques for Corrosion"*, ed. R.Baboian, NACE, Houston, pp. 18-26.

Masur, L.J., Mortenson, A., Cornie, J.A. and Flemings, M.C., (1987), *Proceedings of ICCM6 and ECCM2*, 2, London, pp. 320-329.

McGill, I.R. and McEnaney, B., (1978), *Corrosion Science*, 18, pp. 257-259.

Mileiko, S.T., (1989), *"Handbook of Composites"* 4, eds. A.Kelly and S.T.Mileiko, Elsevier Science, p. 289.

Milliere, C. and Suery, M., (1988), *Materials Science and Technology*, 4, pp. 41-51.

Mondolfo, L.F., (1976), *"Aluminium Alloys: Structure and Properties"*, Butterworth and Co. Ltd., pp. 534-537.

Mueller, I.L. and Galvele, J.R., (1977), *Corrosion Science*, 17, pp. 995-1007.

Murray, G.A.W., Lamb, H.J. and Godard, H.P., (1967), *British Corrosion Journal*, 2, pp. 216-218.

Myers, J.R., Gruenler, E.G., and Smulczenski, L.A., (1968), *Corrosion*, 24, N^0.10, pp. 352-353.

Mykura, N., (1988), *International Symposium on Cast Reinforced Metal Composites*, eds., S.G.Fishman, and A.K.Dhingra, ASM International, Pennsylvania, pp. 173-178.

Mykura, N., (1991), *Metals and Materials*, 7, N^0.1, pp. 7-11.

Nath, D., and Namboodhiri, K.G., (1988), *Composites*, 19, N^0.3, pp.237-243.

Nisancioglu, K. and Holtan, H., (1978a), *Corrosion Science*, 18, pp. 835-849.

Nisancioglu, K. and Holtan, H., (1978b), *Corrosion Science*, 18, pp.1011-1023.

Nisancioglu, K. and Holtan, H., (1978c), *Electrochimica Acta*, 23, pp. 251-253.

Nisancioglu, K. and Holtan, H., (1979), *Werkstoffe und Korrosion*, 30, pp. 105-113.

Nisancioglu, K. and Lunder, O., (1986), *International Conference on Aluminium Alloys-Physical and Chemical Properties"*, 2, eds. E.A.Starke Jr. and T.H.Sanders Jr., Charlottesville, Virginia, pp. 1125-1137.

Oldfield, J.W., Lee, T.S. and Kain, R.M., (1987), *"Corrosion Chemistry within Pits, Cracks and Crevices"*, ed. A.Turnball, HMSO Publishers, pp. 89-96.

Otani, T, McEnaney, B. and Scott, V.D., (1988), *International Symposium on Cast Reinforced Metal Composites*, eds., S.G.Fishman, and A.K.Dhingra, ASM International, Pennsylvania, pp. 383-389.

Otani, T., McEnaney, B., and Scott, V.D., (1989), *Proceedings of ICCM7*, 1, eds. W.Yunshu, G.Zhenlong and W.Renjie, International Academic Publishers, Beijing, China, pp. 423-428.

Otani,T., (1988), *"Corrosion Behaviour of Metal Matrix Composites"*, PhD Thesis, University of Bath.

Paciej, R.C. and Agarwala, V.S., (1988), *Corrosion*, 44, N^{o}.10, pp. 680-684.

Paciej, R.C. and Agarwala, V.S., (1985), *Metallurgical Variables Influencing the Corrosion Susceptibility of a PM Aluminium/SiC_w Composite*, Report N^{o}. NADC-86071-60, Naval Air Developement Centre, Warminster, Pennsylvania.

Pessall, N. and Liu, C., (1971), *Electrochimica Acta*, 16, pp. 1987-2003.

Pohlman, S.L., (1978), *Corrosion*, 34, N^{o}.5, pp. 156-159.

Polmear, I.J., (1981), *"Light Alloys"*, eds. R.W.K.Honeycombe and P.Hancock, Edward Arnold Ltd.

Porte, L. and Sartre, A., (1989), *Journal of Materials Science*, 24, pp.271-275.

Pourbaix, M., Klimzack-Mathieiu, L., Mertens, Ch., Meunier, J., VanLeugen-Haghe, A., de Munck, L., Laureys, J., Neelemans, L. and Warzee, M., (1963), *Corrosion Science*, 3, pp. 239-259.

Richardson, J.A. and Wood, G.C., (1970), *Corrosion Science*, 10, pp. 313-323.

Rosenfeld, I.L. and Marshakov, I.K., (1964), *Corrosion*, 20, pp. 115-125.

Schrier, L.L., (1978), *"Corrosion"*, Vol.2, ed. L.L.Schrier, (1st edition 1963), George Newnes Ltd., p 20.12.

Sedriks, A.J., Green, J.A.S. and Novak, D.L., (1971), *Metallurgical Transactions*, 2, pp.871-875.

Sewell, D.A., Love, G. and Scott, V.D., (1985), *Journal of Physics D: Applied Physics*, 18, pp. 1245-1268.

Sherif, K.P. and Narayan, R., (1989), *British Corrosion Journal*, 24, N^{o}.3, pp. 199-203.

Smallman, R.E. and Ashbee, K.H.G., (1969), *"Modern Metallography"*, 2nd edition, (1st edition 1966), Permagon Press, p. 109.

Summerson, T.J. and Sprowls, D.O., (1986), *"International Conference on Aluminium Alloys-Physical and Chemical Properties"*, 3, eds. E.A.Starke Jr. and T.H.Sanders Jr., Charlottesville, Virginia, pp.1575-1631.

Syrett, B.C., (1976), *"Electrochemical Techniques for Corrosion"*, ed. R.Baboian, NACE, Houston, pp. 112-113.

Syrett, B.C., (1977), *Corrosion*, 33, N°.6, pp.221-224.

Szklarska-Smialowska, J., (1986), *"Pitting Corrosion of Metals"*, NACE, p. 58.

Szklarska-Smialowska, Z. and Janik-Czachor, M., (1971), *Corrosion Science*, 11, pp. 915-927.

Trzaskoma, P.P., (1990), *Corrosion*, 46, N°.5, pp.402-409.

Trzaskoma, P.P., McCafferty, E. and Crowe, C.R., (1983), *Journal of the Electrochemical Society*, 130, N°.9, pp. 1804-1809.

Vassilaros, M.G., Davies, D.A., Stecke, G.L., Gudas, J.P. and Taylor, D.W., (1980), *Proceedings of the Tri-Srevice Conference on Corrosion*, 2, U.S. Air Force Academy, Colarado, pp. 335-352.

Walker, M.S. and Rowe, L.C., (1976), *"Electrochemical Techniques for Corrosion"*, ed. R.Baboian, NACE, Houston, pp. 79-82.

Ward, C.M., Close, and Partridge, P.G., (1989), *Institute of Metals; Metal Matrix Composites Conference Proceedings*, London, pp. 8.1-8.3.

Weisshaus, I., Gal-Or, L. and Kaufman, A., (1980), *Corrosion Science*, p. 1119.

White, J. and Willis, T.C., (1989), *Materials and Design*, 10, N°.3, pp. 121-127.

Wilde,B.E. and Williams, E., (1971), *Electrochimica Acta*, 16, pp. 1971-1985.

Wilde, B.E., (1972), *Corrosion*, 28, N°.8, pp.283-291.

Wood, G.C., Sutton, W.H., Richardson, J.A., Riley, T.N.K. and Malherbe, A.G., (1974), *"Localised Corrosion"*, NACE-3, pp. 526-539.

Yajima, S., Hasegawa, Y., Hayashi, J. and Iimura, M., (1978), *Journal of Materials Science*, 13, pp. 2569-2576.

Yang, M. and Scott, V.D., (1991a), *Journal of Materials Science*, 26, pp. 1609-1617.

Yang, M. and Scott, V.D., (1991b), *Journal of Materials Science*, 26, pp. 2245-2254.

Zhu, Z., (1988), *International Symposium on Cast Reinforced Metal Composites*, eds., S.G.Fishman, and A.K.Dhingra, ASM International, Pennsylvania, pp. 93-99.

TABLES

ALLOY	COMPOSITION (wt%)
357	7Si; 0.5Mg; rem. Al
2124	4.0Cu; 1.5Mg; 0.6Mn; rem. Al
Super purity aluminium	99.99% Al; rem impurity elements
Commercial purity aluminium	99.5% Al; rem impurity elements (Fe,Si)
430 stainless steel	16.5Cr; 0.49Si; 0.4Mn; 0.27Ni; 0.07Cu 0.05C; rem. Fe

Table 3.1 Chemical compositions of the alloys.

REINFORCEMENT	LENGTH	DIAMETER (μm)
Carbon fibre	continuous	8
Nicalon fibre	continuous	15
Saffil fibre	~100μm	3
SiC particulate	-	3

Table 3.2 Details relating to the geometry of the reinforcements.

MATRIX	REINFORCEMENT	COMPOSITE NAME	FABRICATION METHOD	FORM RECEIVED
357	Carbon	357-C_L	LMI	~10mm plate
357	Carbon	357-C_S	SC	~10mm plate
357	Nicalon	357-Nic	LMI	~3mm sheet
357	Saffil	357-Saf	LMI	~10mm plate
2124	Carbon	2124-C	SC	~10mm plate
2124	SiC	2124-SiC	PM	~2mm sheet
Al	Carbon	Al-C	SC	~10mm plate

SC = Squeeze cast
LMI = Liquid metal infiltration
PM = Powder metallurgy

Table 3.3 Details relating to the metal matrix composites.

CHARACTERISTIC POTENTIAL	MEAN VALUE
E^1_{corr}	-732±5 mV
E^1_{prot}	-965±10 mV
HA^1	322±35 μC
E^2_{corr}	-1147±40 mV
E^2_{pit}	-726±5 mV
E^2_{prot}	-946±5 mV
HA^2	279±60 μC

Table 4.1. The DCP test results for 2124-SiC MMC.

	ORIENTATION			
	(211)	(111)	(110)	(100)
E^1_{pit} (mV)	-785	-785	-790	-780
E^2_{pit} (mV)	-780	-775	-780	-780
E^1_{prot} (mV)	-1140	-1230	-1215	-1215
E^2_{prot} (mV)	-845	-860	-860	-1290
E^1_{corr} (mV)	-970	-1087	-1040	-1065
E^2_{corr} (mV)	-1175	-1215	-1252	-1270
HA^1 (μC)	89	91	86	76
HA^2 (μC)	96	91	79	85

Table 4.2 DCP test data for single crystals of aluminium.

IMMERSION TIME (days)	WEIGHT LOSS ($g.^{m-2}$)	CORROSION RATE ($g.m.^{-2}.h^{-1}$)
1	1.20±0.2	0.005
3	1.87±0.4	0.026
7	3.56±0.7	0.021
21	6.15±1.2	0.012

Table 4.3 Results of gravimetric tests conducted on 357 alloy.

MATERIAL	E_{init} (mV)	E_{min} (mV)
357	-764±5	-1044±40
357-C_L	-774±40	-938±60
357-C_S	-784±60	-934±60
357-Nic	-778±15	-1085±45
357-Saf	-763±5	-990±70
2124	-772±5	-895±30
2124-C	-749±20	-923±25
2124-SiC	-729±20	-984±40
Al	-787±15	-1143±10
Al-C	-772±5	-1088±50

Table 4.4 Open circuit test results

MATERIAL	SCAN RATE (mV/min)	E_{pit} (mV)	E_{prot} (mV)	E_{corr} (mV)	HA (μC)
357	20 2	-743±5 -751±5	-1079±80 -1030±5	-995±150 -854±25	213±45 220±60
357-C_L	20 2	-752±10 *	-850±15 -837±5	-919±10 -749±5	191±5 104±20
357-C_S	20	-763±5	-896±45	-880±60	119±10
357-Nic	20 2	-751±5 *	-810±10 -863±15	-969±65 -742±20	283±70 237±10
357-Saf	20 2	-761±5 -770±5	-947±45 -1006±30	-938±50 -939±80	85±15 132±10
2124	20	-748±10	-902±5	-1047±20	375±45
2124-C	20	-705±10	-854±10	-958±40	149±5
2124-SiC	20	-726±5	-965±10	-1147±40	322±35
Al	20	-770±20	-858±45	-854±10	145±20
Al-C	20	-775±5	-900±90	-1054±65	145±30

* Epit not recorded on either cycle

Table 4.5 The polarisation data from DCP tests.

IMMERSION TIME (days)	WEIGHT GAIN ($g.m^{-2}$)	RATE OF WEIGHT GAIN ($g.m^{-2}.h^{-1}$)
1	1.53±0.3	0.064
3	2.08±0.4	0.029
7	2.83±0.6	0.017
21	3.94±0.8	0.008

Table 4.6 Results of gravimetric tests on 357-C_L MMC.

COUPLE	**CURRENT μA**	**CORROSION RATE $mm.yr^{-1}$**
357-C	465	5.0
357-Nic	72	0.8
2124-C	320	3.6
Al-C	260	2.8

Table 4.7 The results of galvanic couple tests.

IMMERSION TIME (days)	WEIGHT LOSS ($g.m^{-2}$)	CORROSION RATE ($g.m^{-2}.h^{-1}$)
1	0.67±0.1	0.028
7	0.77±0.2	0.005
21	2.53±0.5	0.005

Table 4.8 Results of gravimetric test on 357-Nic MMC.

IMMERSION TIME (days)	WEIGHT GAIN ($g.m^{-2}$)	RATE OF WEIGHT GAIN ($g.m^{-2}.h^{-1}$)
1	25±5	1.0
3	78±15	1.1
7	120±24	0.7
21	97±20	0.2

Table 4.9 Results of gravimetric tests on 357-Saf MMC.

IMMERSION TIME (days)	WEIGHT LOSS ($g.m^{-2}$)	CORROSION RATE ($g.m^{-2}.hr^{-1}$)
1	0.50±0.1	0.020
3	0.87±0.2	0.012
7	1.70±0.3	0.011
21	5.07±1.0	0.010

Table 4.10 Results of gravimetric tests on 2124 alloy.

IMMERSION TIME (days)	WEIGHT LOSS ($g.m^{-2}$)	CORROSION RATE ($g.m^{-2}.h^{-1}$)
1	0.33±0.07	0.013
3	0.75±0.15	0.010
7	0.99±0.2	0.006
21	5.98±1.2	0.012

Table 4.11 Results of gravimetric tests on 2124-SiC MMC.

IMMERSION TIME (days)	WEIGHT LOSS ($g.m^{-2}$)	CORROSION RATE ($g.m^{-2}.h^{-1}$)
1	0.19±0.03	0.013
3	0.80±0.15	0.011
7	0.73±0.15	0.004
21	2.13±0.43	0.004

Table 4.12 Results of gravimetric tests on commercial purity aluminium.

COUPLE	GALVANIC CORROSION RATE ($mm.yr^{-1}$)	MAXIMUM PIT DEPTH (μm)
357/C	5.0	6000 (LMI) 300 (SC)
357/Nic	0.8	350
2124/C	3.6	50
Al/C	2.8	150

LMI; MMC fabricated by liquid metal infitration
SC; MMC fabricated by squeeze casting

Table 5.1 Comparison of the galvanic corrosion rate and the measured between matrix/fibre couple with maximum pit depth recorded in the corresponding MMC

FIGURES

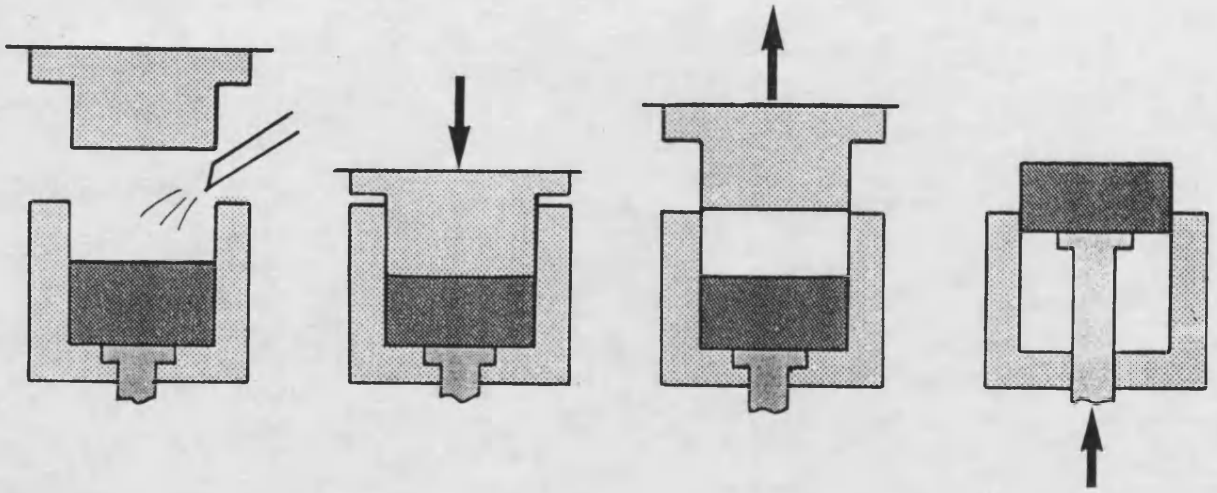

Fig.2.1 Schematic illustration of the squeeze casting process (taken from Chadwick and Yue, 1989).

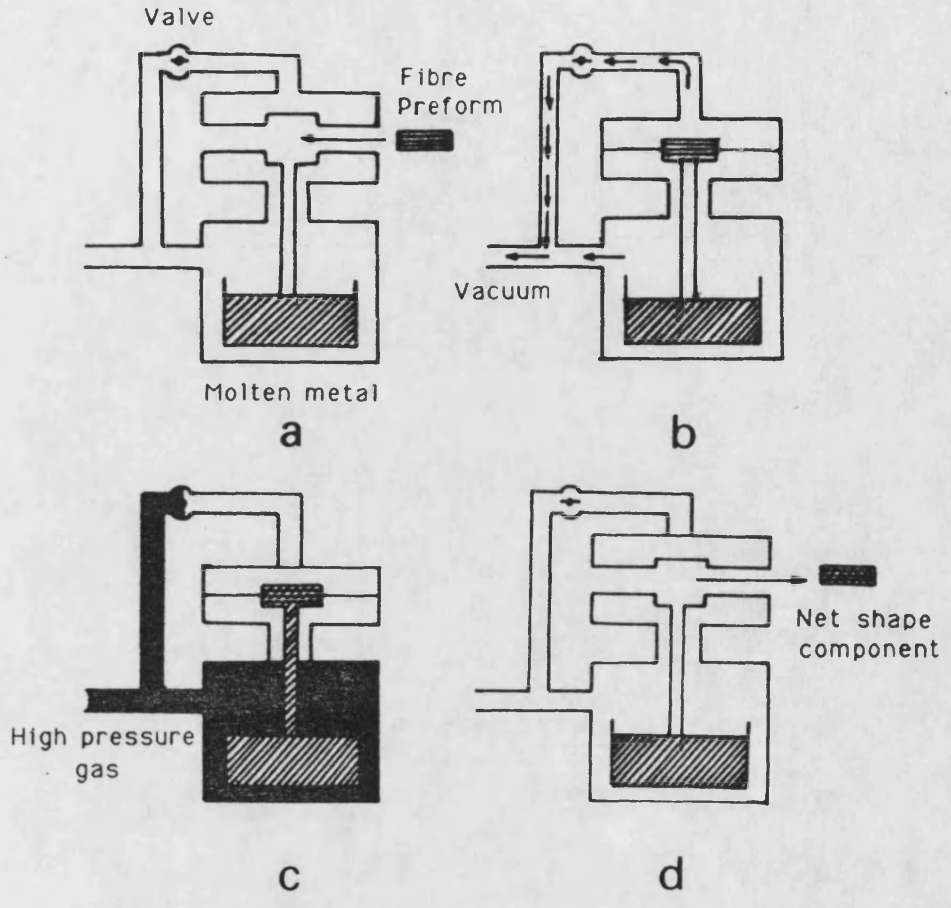

Fig.2.2 Schematic illustration of the liquid metal infiltration process.

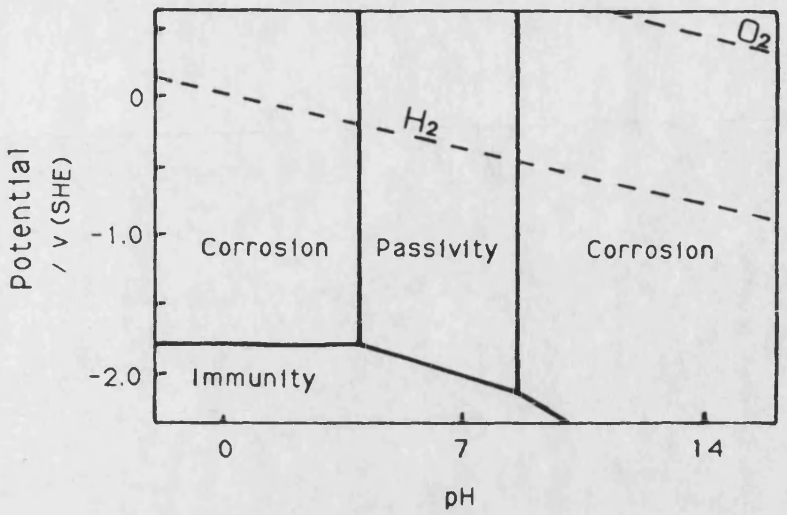

Fig.2.3 The Pourbaix diagram for aluminium in water.

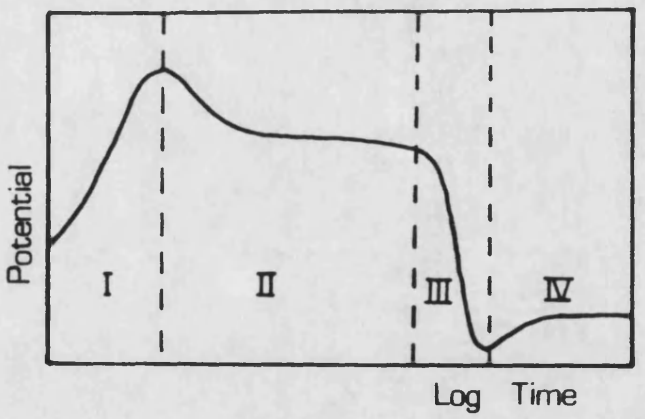

Fig.2.4 An illustration of the variation in open cicuit potential with time proposed by Nisancioglu and Holtan (1978a and 1979)

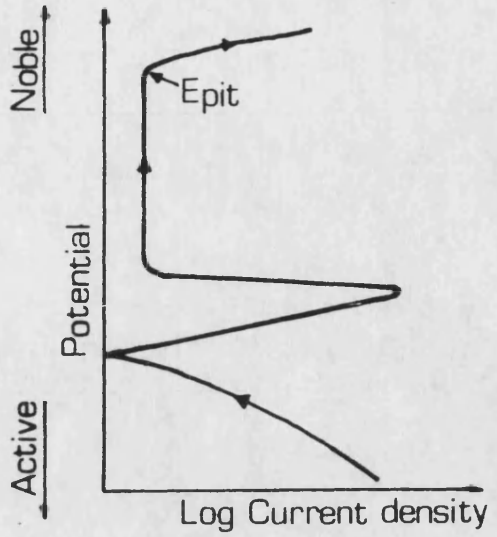

Fig.2.5 A schematic of an anodic polarisation curve

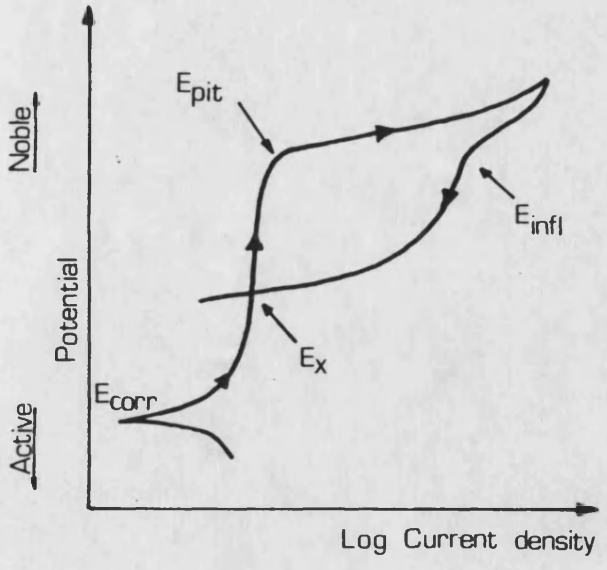

Fig.2.6 A schematic of a cyclic polarisation curve

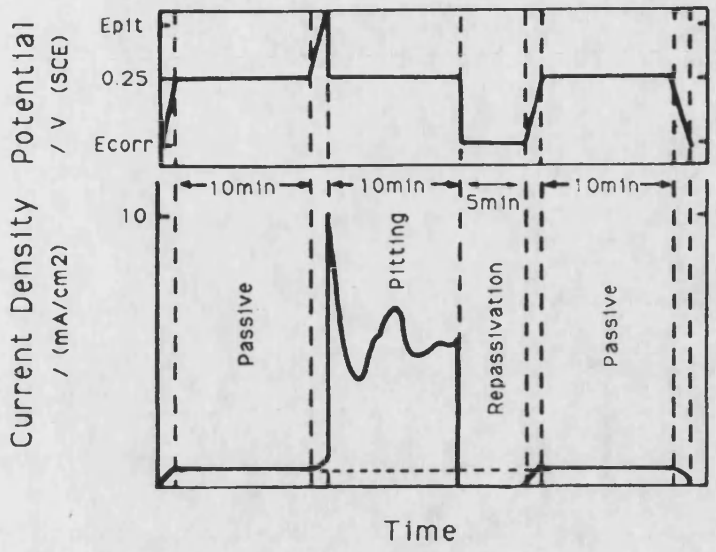

Fig.2.7 An example of the variation in current with time of a specimen taken through an anodic cycle (from Syrett, 1977).

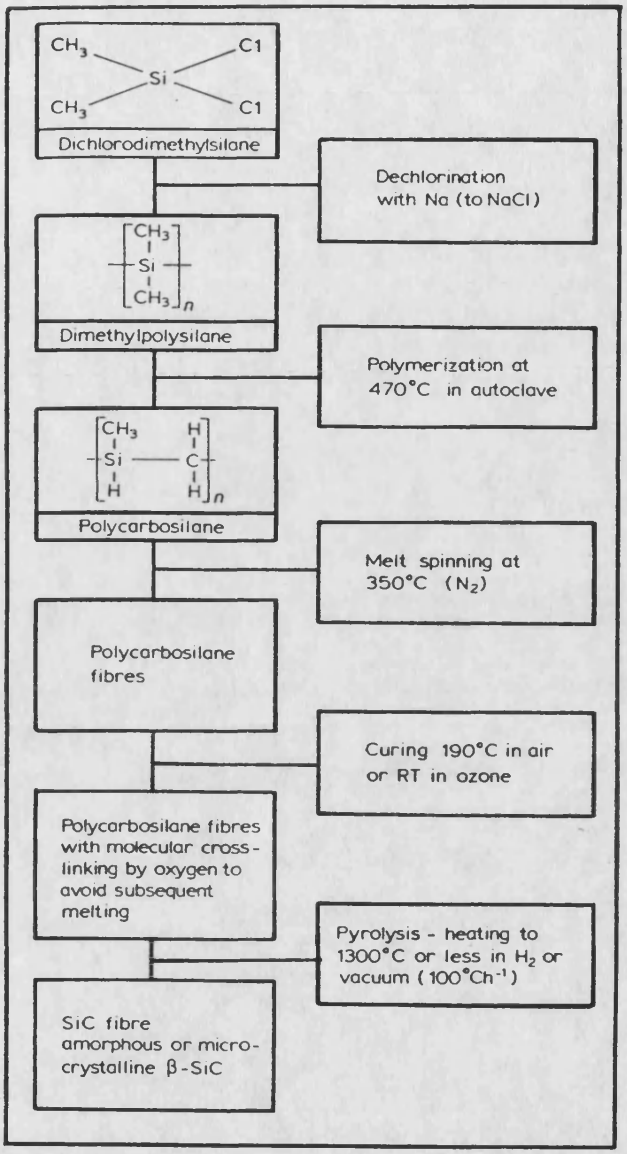

Fig.3.1 A flow diagram illustrating the main stages in the preparation of Nicalon fibres (taken from Anderson and Warren 1984)

(a)

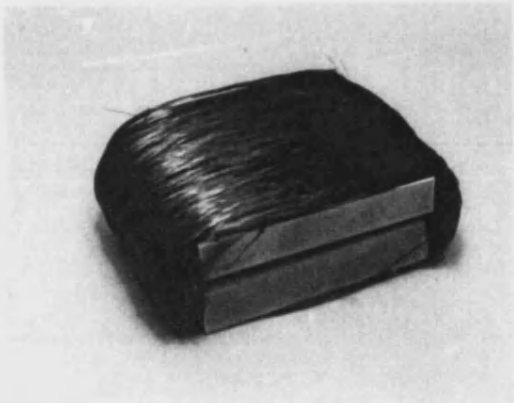

(b)

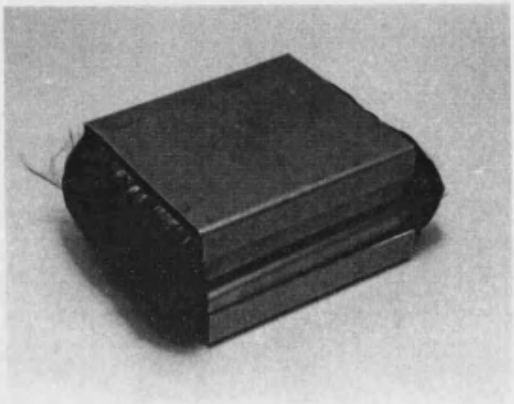

(c)

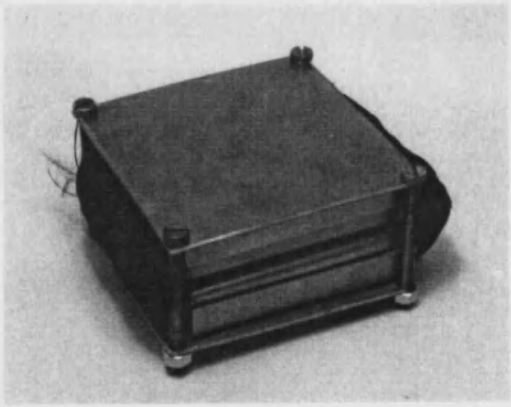

Fig.3.2 The stages in the preparation of a fibre preform for the squeeze casting process
(a) fibres wound around steel plates
(b) steel caps placed over the fibres to hold them in place
(c) preform clamped between steel plates to prevent the fibres from separating during infiltration of the molten metal

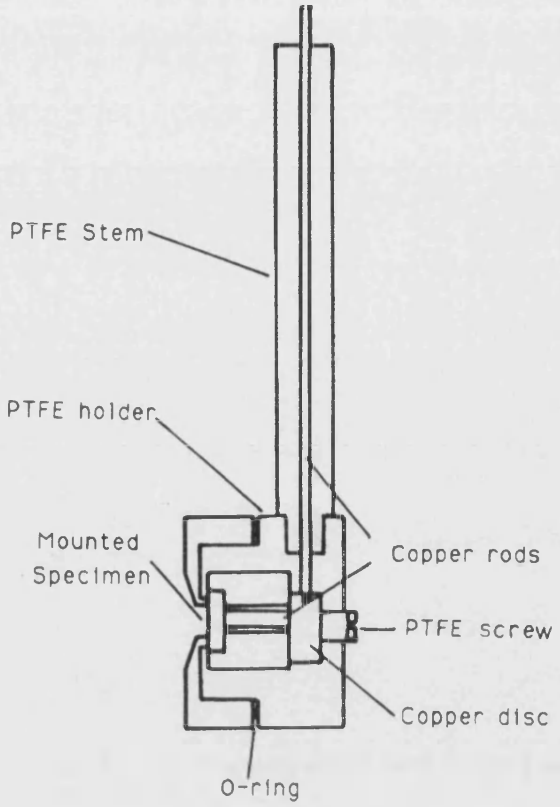

Fig.3.3 A schematic of the PTFE working electrode holder

Fig.3.4 The computer-controlled polarisation equipment

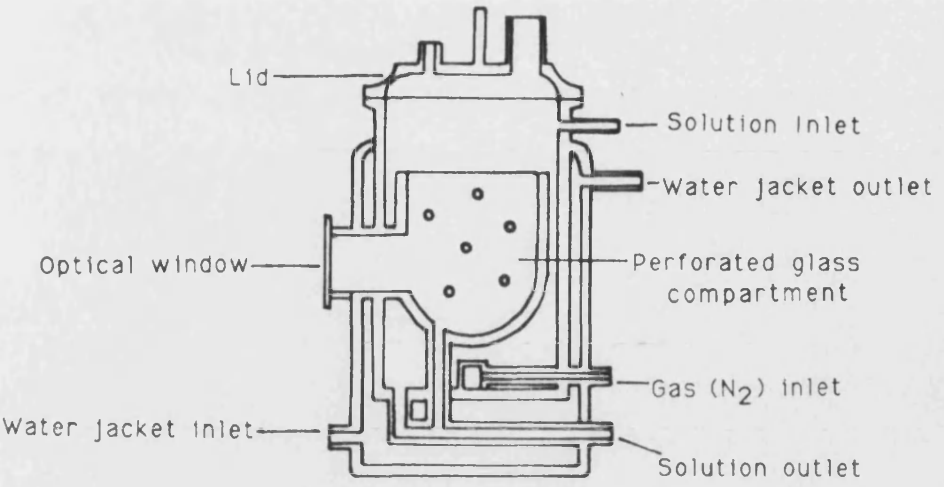

Fig.3.5 A schematic of the coaxial glass cell

Fig.3.6 The glass cell equipped with the working, reference and auxilliary electrodes

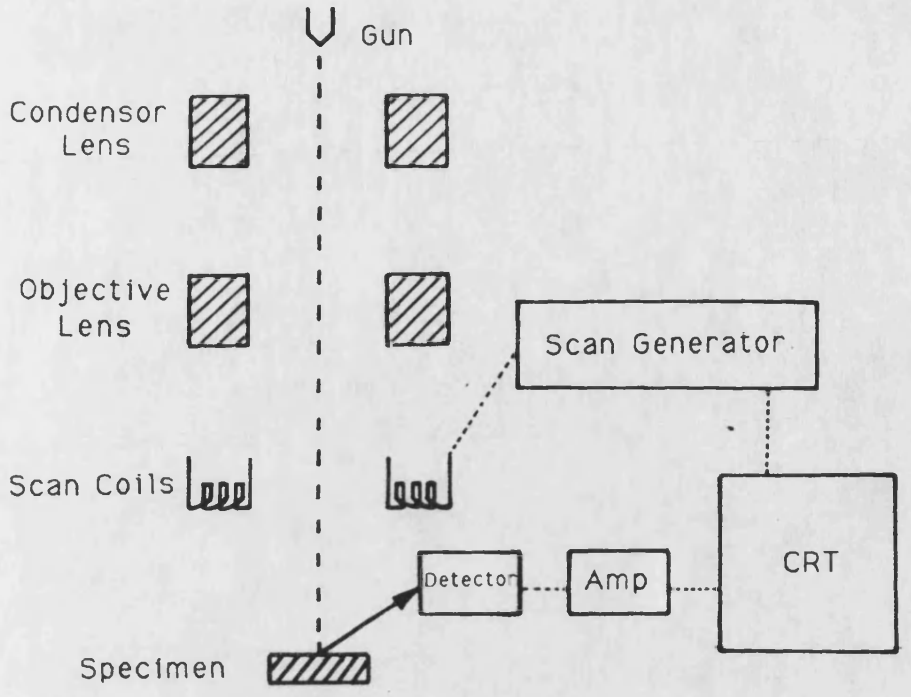

Fig.3.7 A schematic showing the operation of a scanning electron microscope

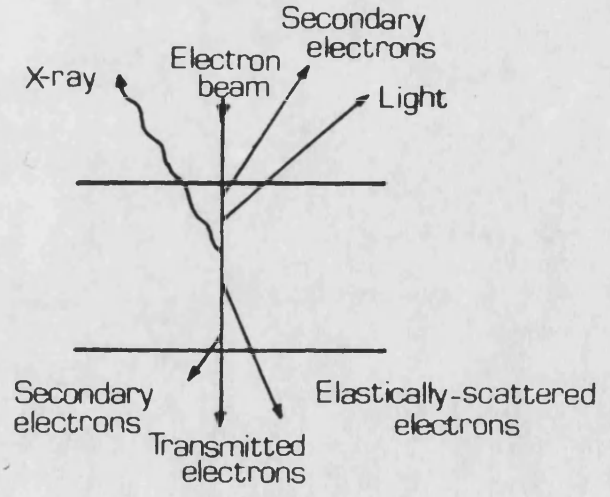

Fig.3.8 A summary of the secondary effects which may be excited when a beam of primary electrons hits the surface

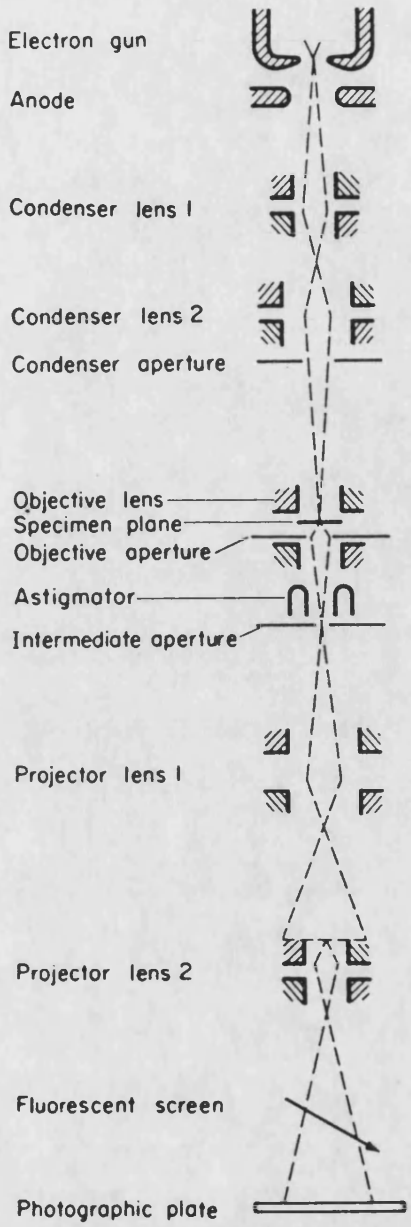

Fig.3.9 A schematic showing the operation of a transmission electron microscope (from Smallman and Ashbee, 1969)

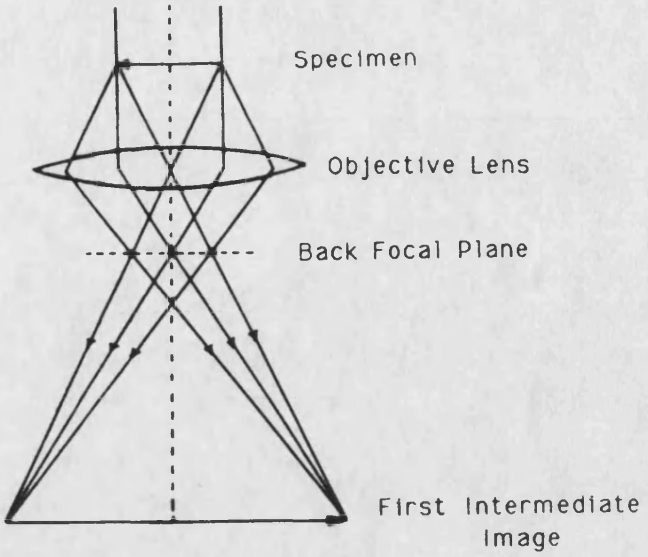

Fig.3.10 A schematic illustrating the formation of a diffraction pattern in the transmission electron microscope

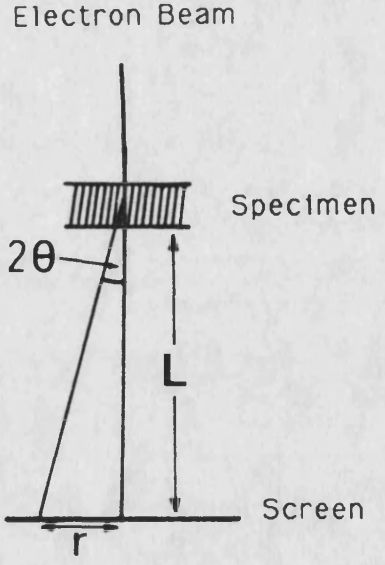

Fig.3.11 An illustration of a beam of electrons of wavelength λ, which have been diffracted through an angle θ, by a crystal whose interplanar spacing is d

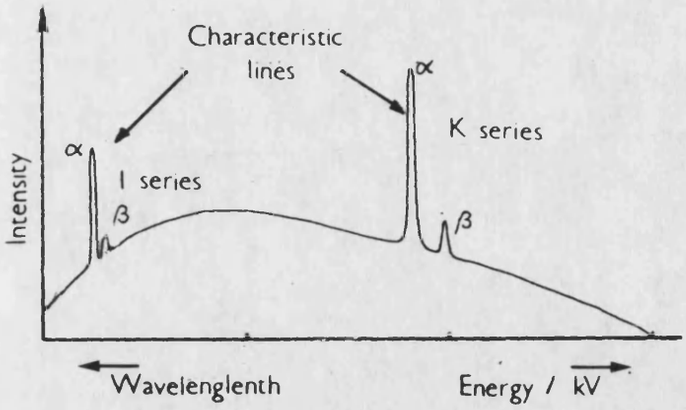

Fig.3.12 An example of a spectrum obtained from EDS analysis

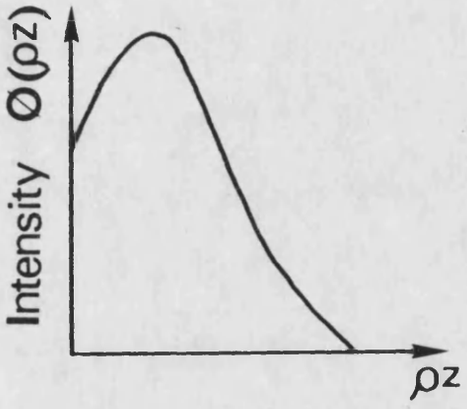

Fig.3.13 The variation of X-ray intensity with mass depth

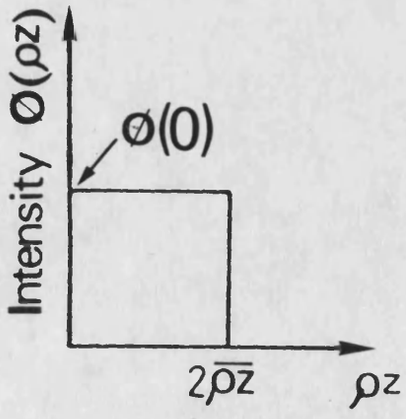

Fig.3.14 Rectangular model for X-ray generation

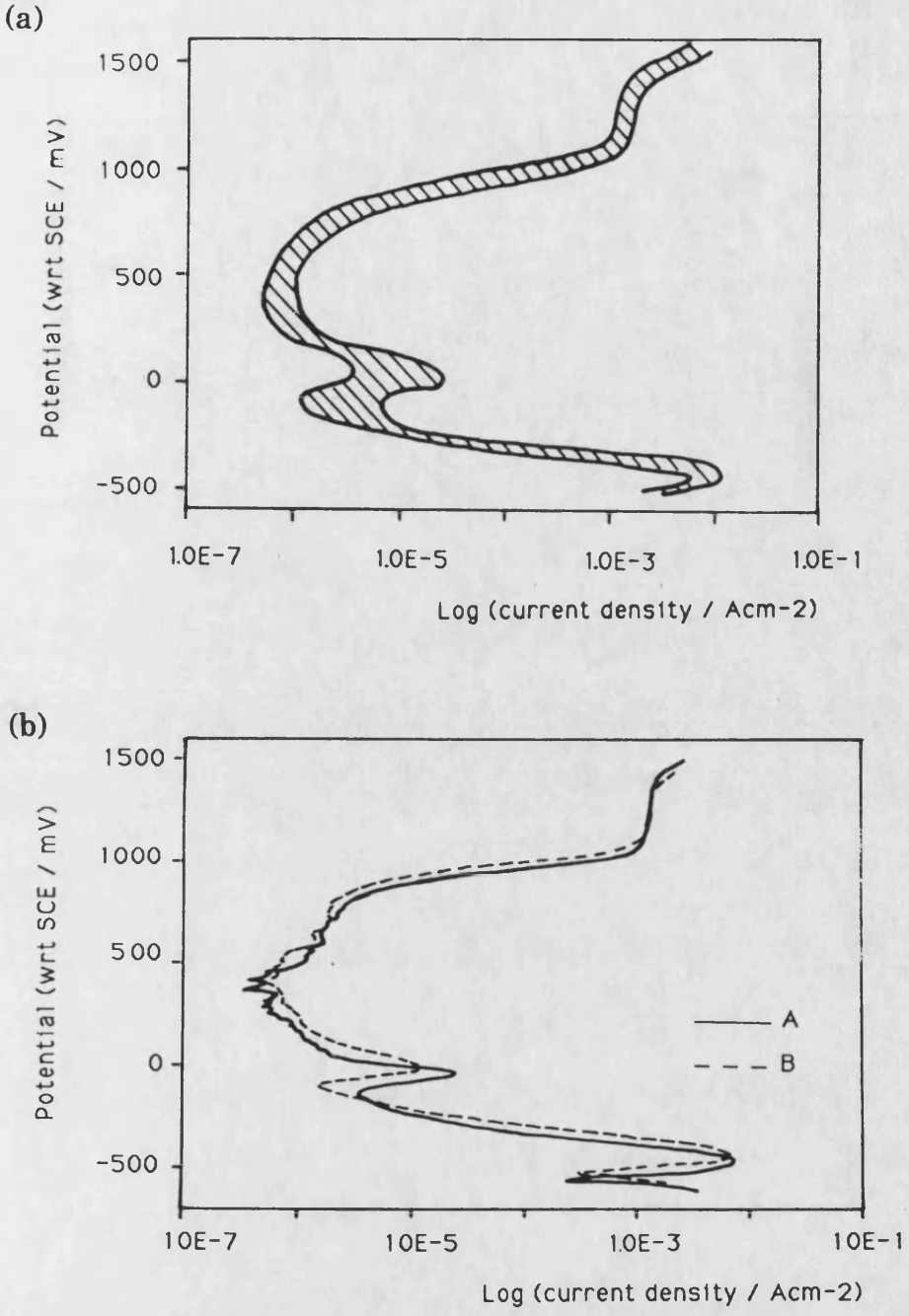

Fig.4.1 Anodic polarisation curves for 430 stainless steel
(a) The range of results from the ASTM standard test
(b) Results from our tests conducted with (A) and without (B) a Luggin probe

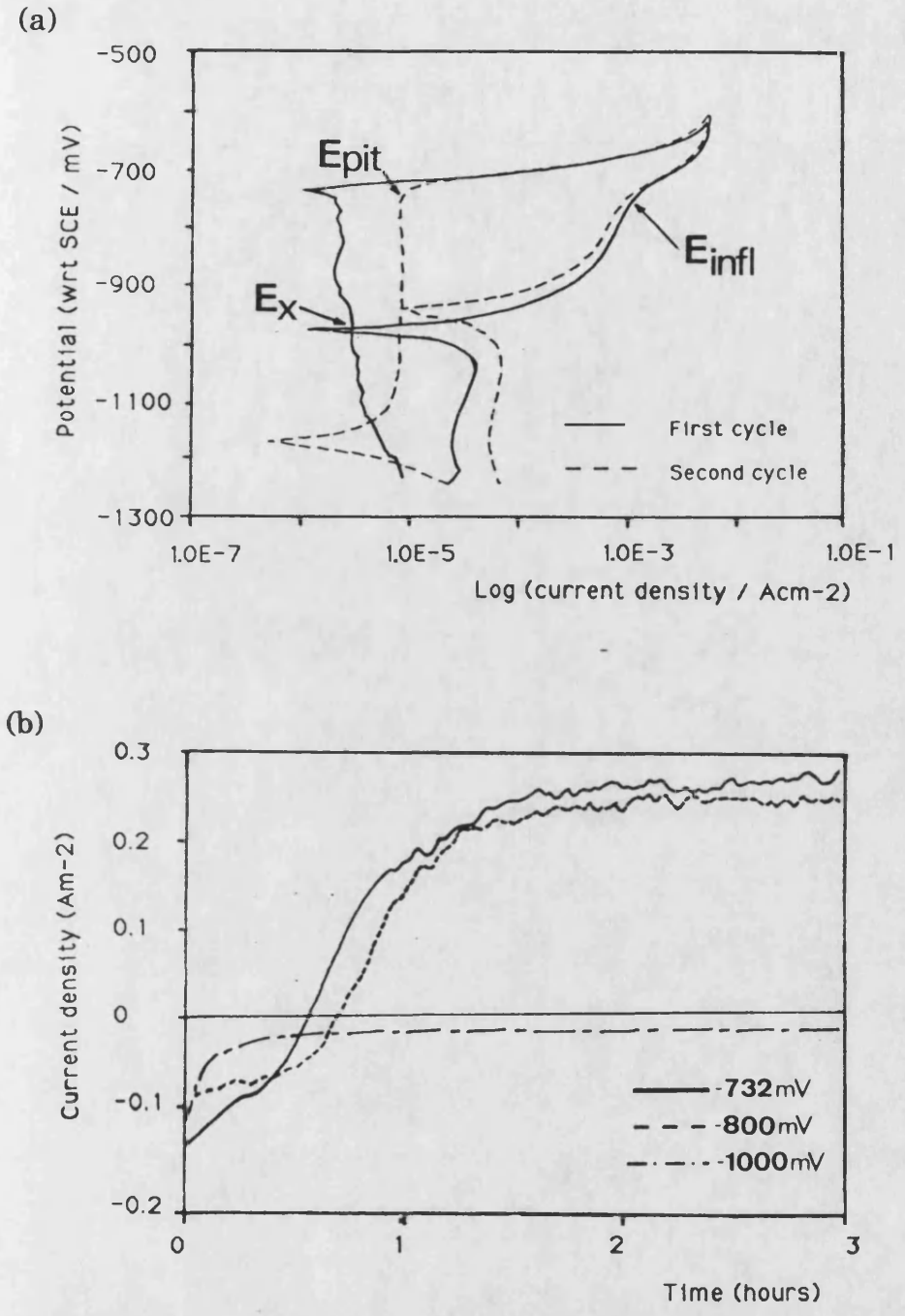

Fig.4.2 (a) A DCP curve for 2124-SiC, showing the position of E_{pit}, E_{infl} and E_x

(b) Potentiostatic tests performed on 2124-SiC at -732mV, -800mV and -1000mV.

(a)

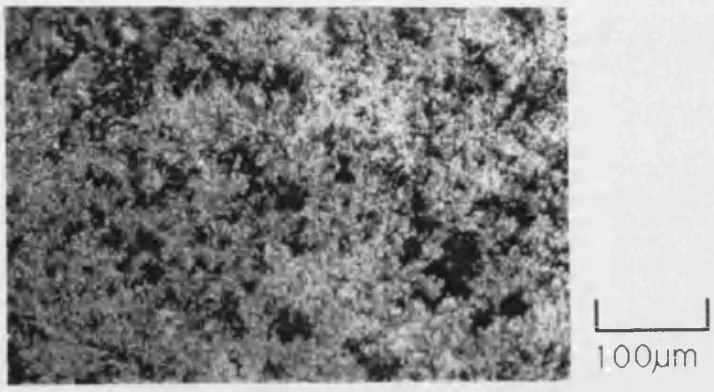

(b)

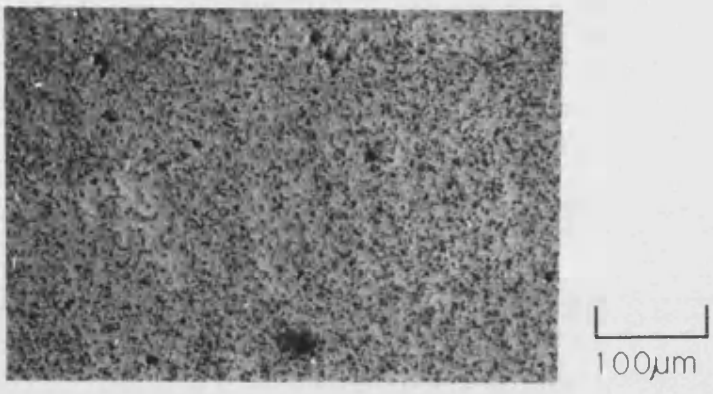

(c)

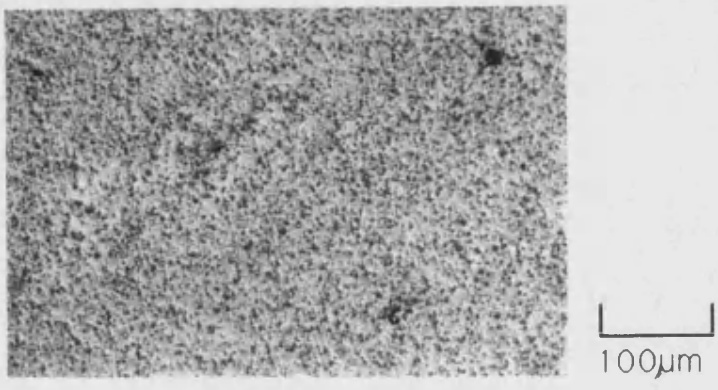

Fig.4.3 Optical micrographs of 2124-SiC
(a) After potentiostatic polarisation at -800mV for 3 hours
(b) After potentiostatic polarisation at -1000mV for 3 hours
(c) After natural immersion for 15 minutes

(a)

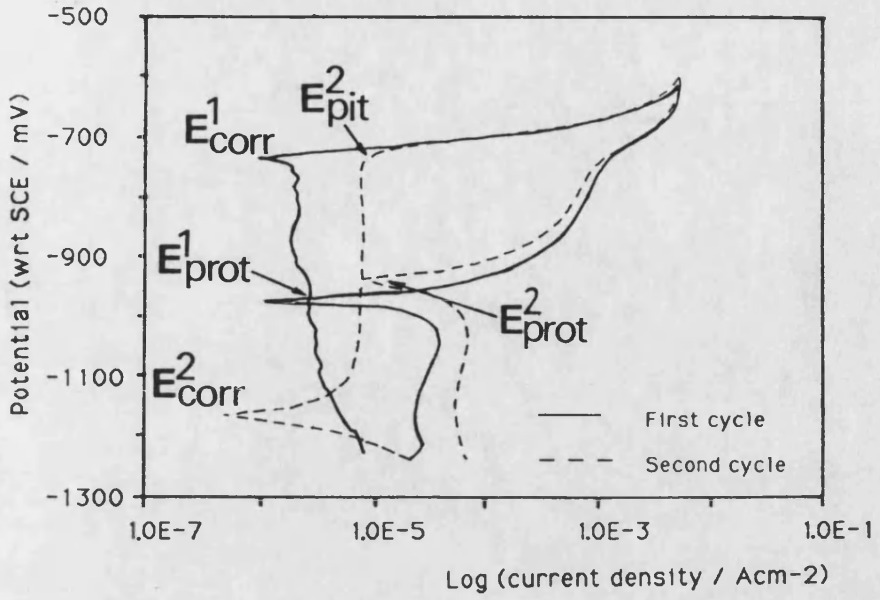

(b)

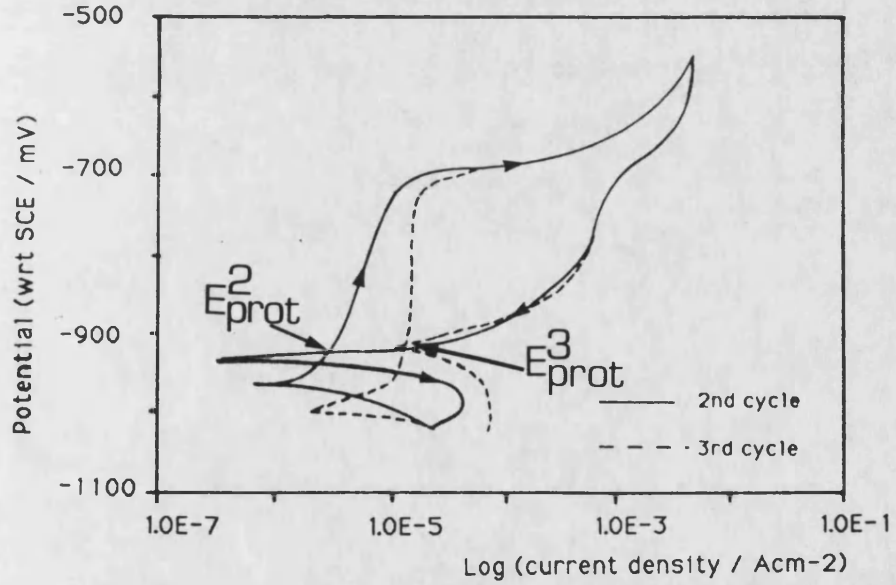

Fig.4.4 (a) A double cyclic polarisation curve for 2124-SiC illustrating the position of E_{pit}, E_{prot} and E_{corr} on each cycle

(b) A triple cyclic polarisation curve for 2124-SiC illustrating the second and third cycles only

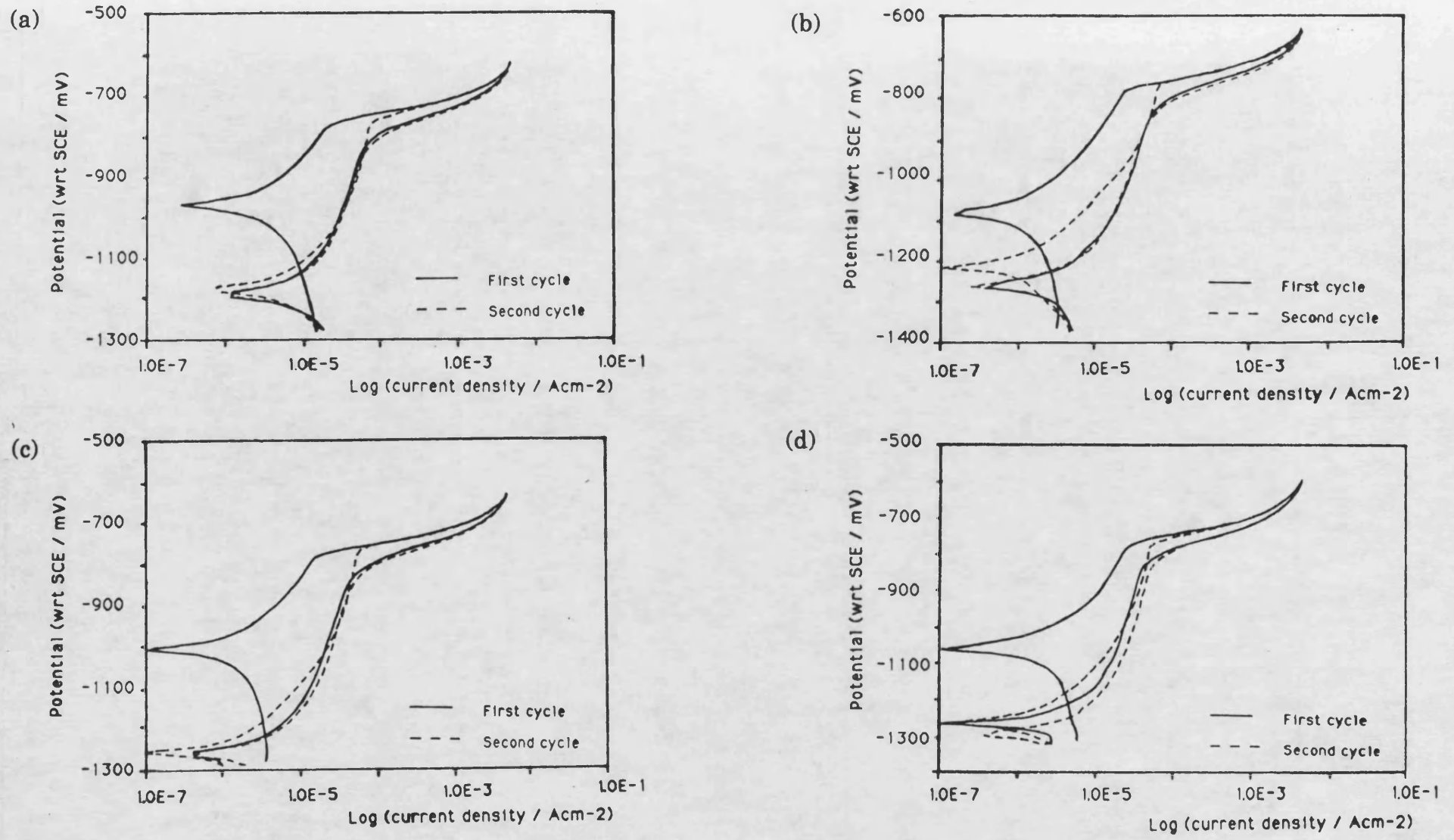

Fig.4.5 DCP curves obtained on single crystals of aluminium different exposed crystallographic orientations (a)(211)(b)(111)(c)(110)and (d)(100)

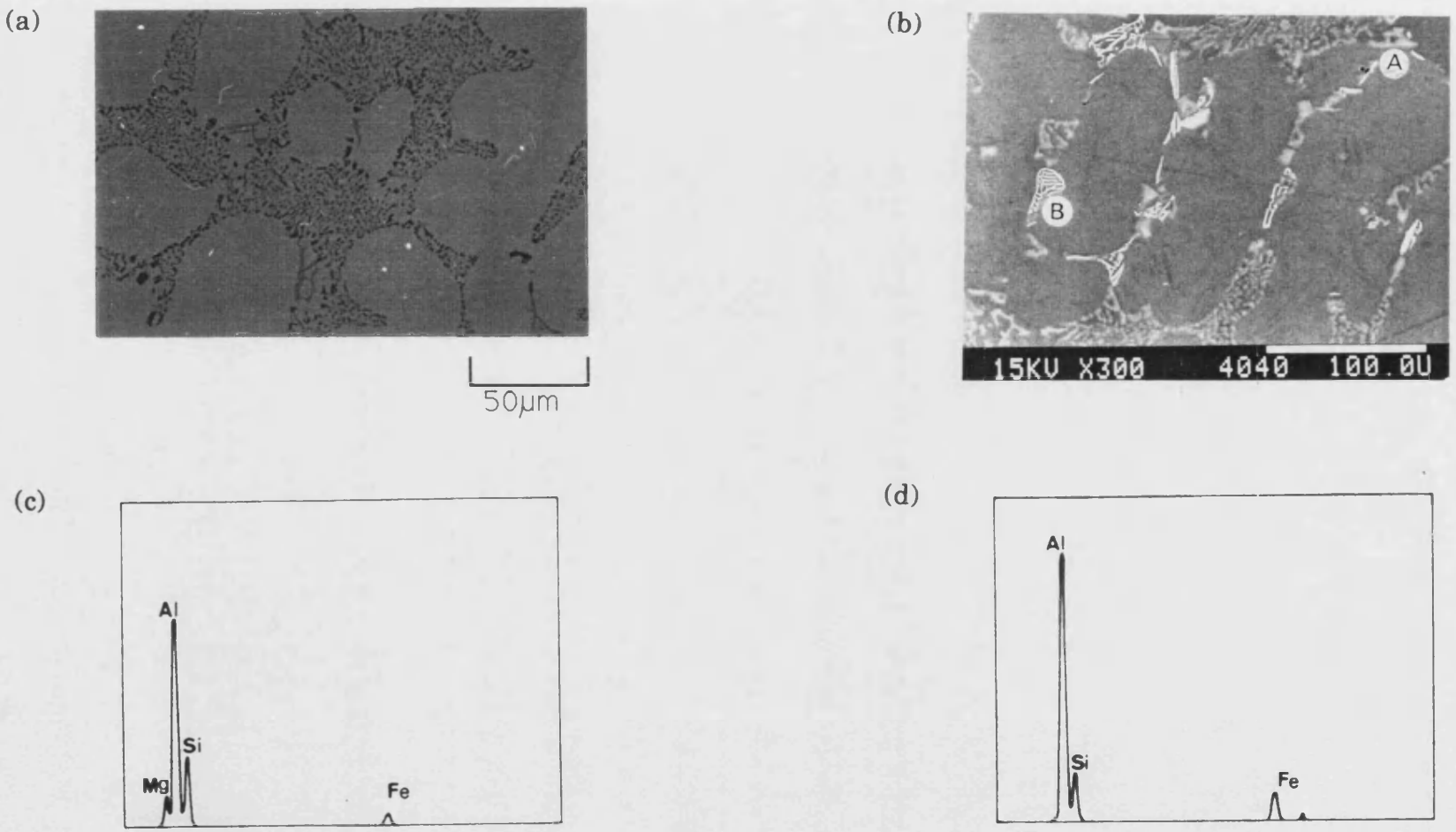

Fig.4.6 (a) Optical micrograph of 357 alloy
(b) SEM micrograph of 357 alloy, illustrating the presence of light grey and white "script"-like phases
(c) EDS analysis of the light grey phase (A)
(d) EDS analysis of the white phase (B)

(a)

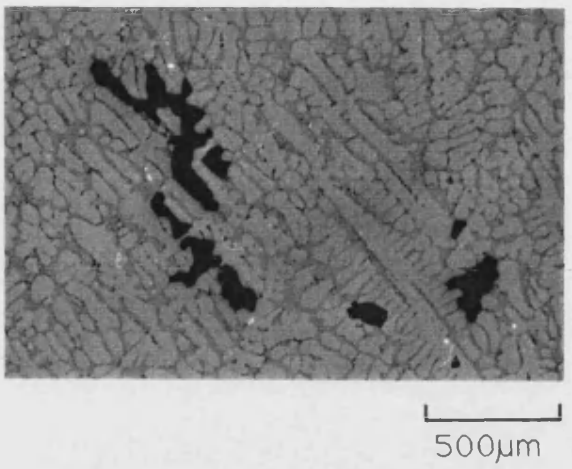

(b)

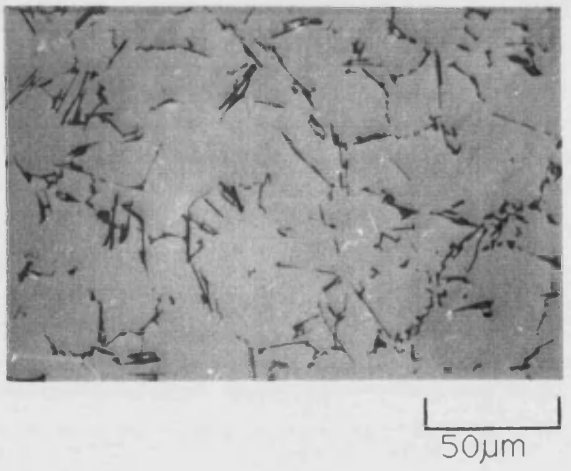

Fig.4.7 (a) Casting defects in 357 alloy
(b) 357 alloy produced by liquid metal infiltration

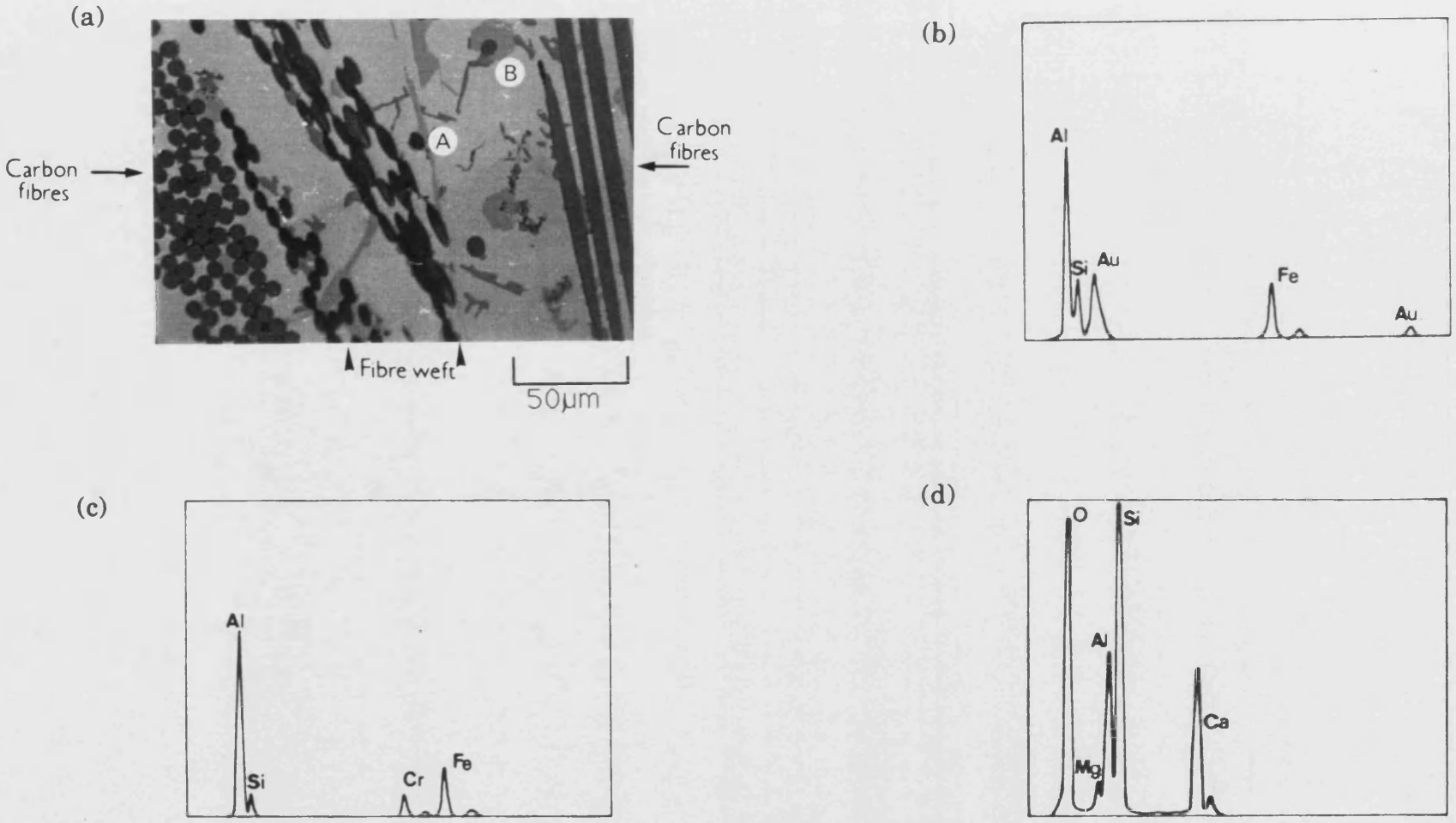

Fig.4.8 (a) Optical micrograph of 357-C_L showing the presence of pale grey needle-like (A) and platelet-like (B) phases
(b) EDS analysis of phase A
(c) EDS analysis of phase B
(d) EDS analysis of fibre weft

(a)

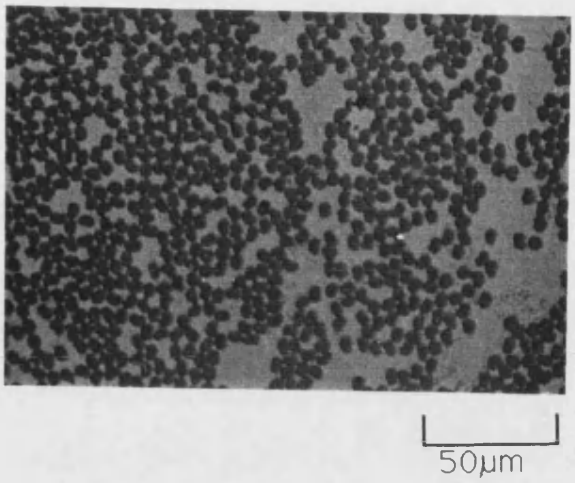

(b)

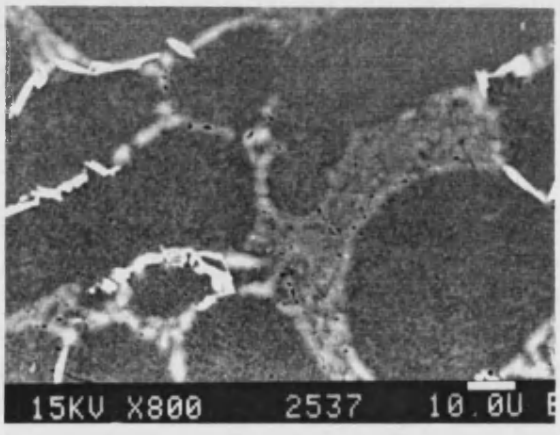

Fig.4.9 (a) Optical micrograph of 357-C_S
(b) SEM micrograph of a fibre-free region in 357-C_S showing the presence of $FeSiAl_5$ intermetallic (white needles)

(a)

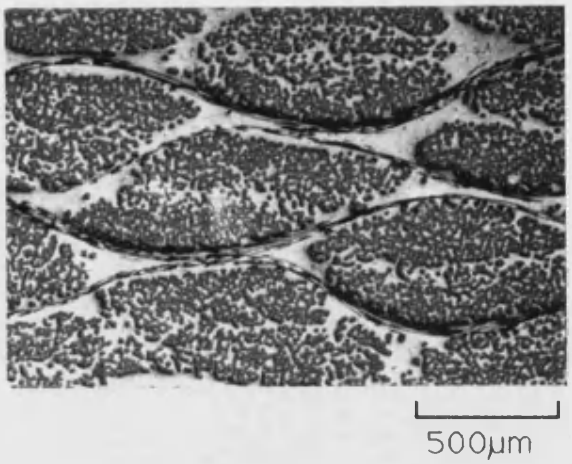

(b)

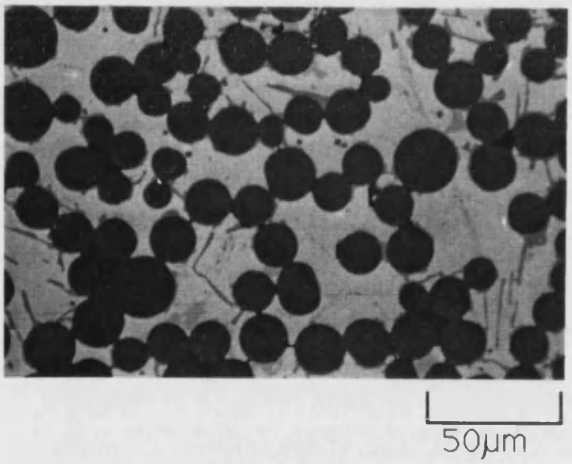

Fig.4.10 Optical micrographs of 357-Nic
(a) With glass fibre weft (material A)
(b) With organic binder (materials B)

(a)

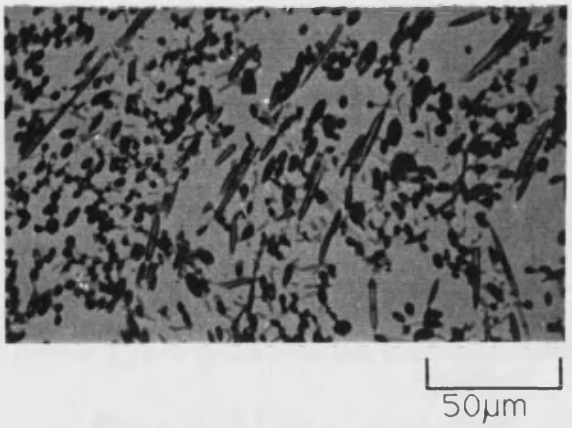

(b)

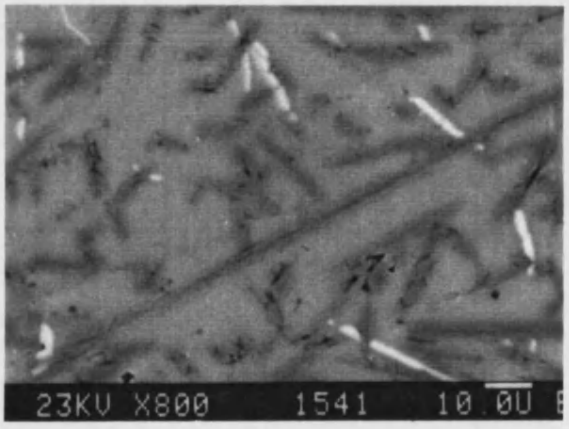

Fig.4.11 (a) Optical micrograph of 357-Saf
(b) SEM micrograph of 357-Saf showing the presence of $FeSiAl_5$ intermetallic (white needles)

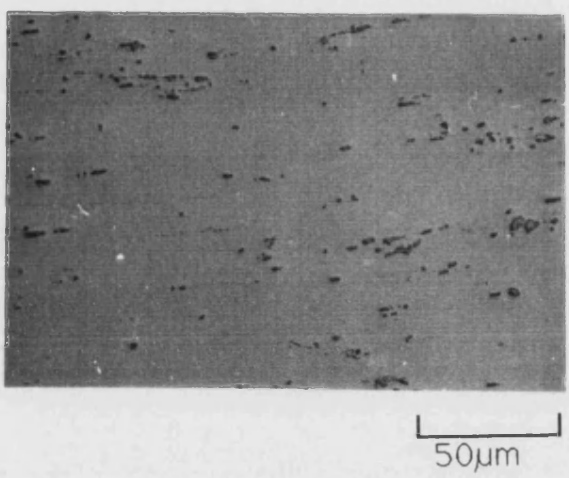

Fig.4.12 Optical micrograph of 2124 alloy

(a)

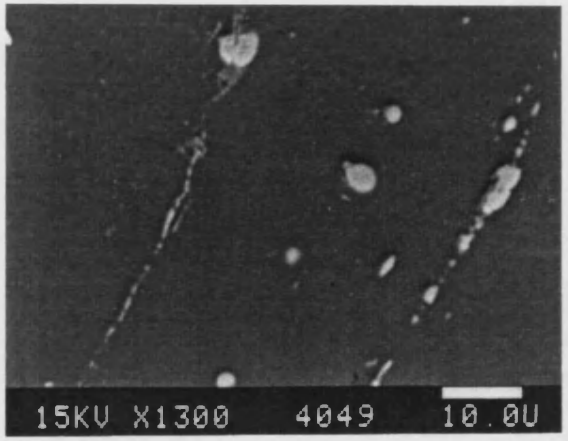

(b)

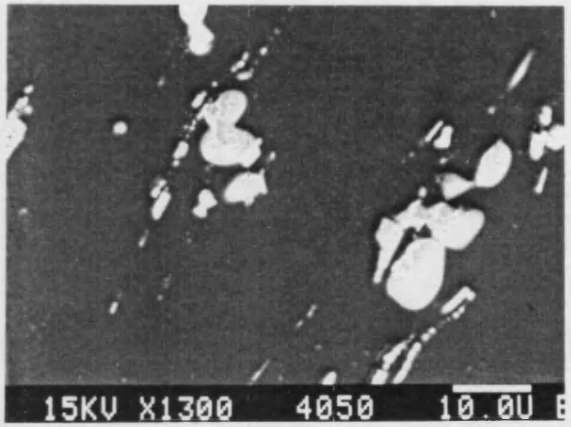

(c)

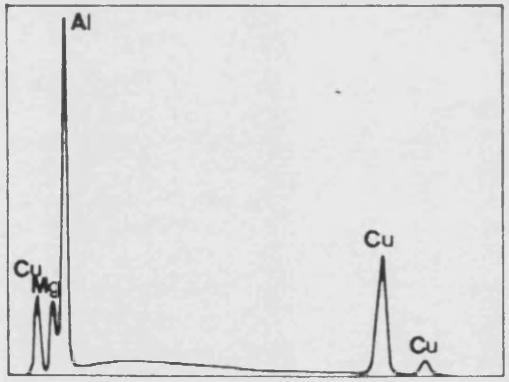

(d)

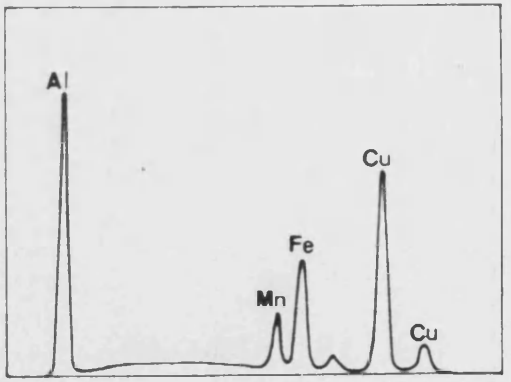

Fig.4.13 (a) SEM micrograph of phase in 2124 alloy containing Al, Cu and Mg
(b) SEM micrograph of phase in 2124 alloy containing Al, Cu, Mn and Fe
(c) EDS analysis of phase in (a)
(d) EDS analysis of phase in (b)

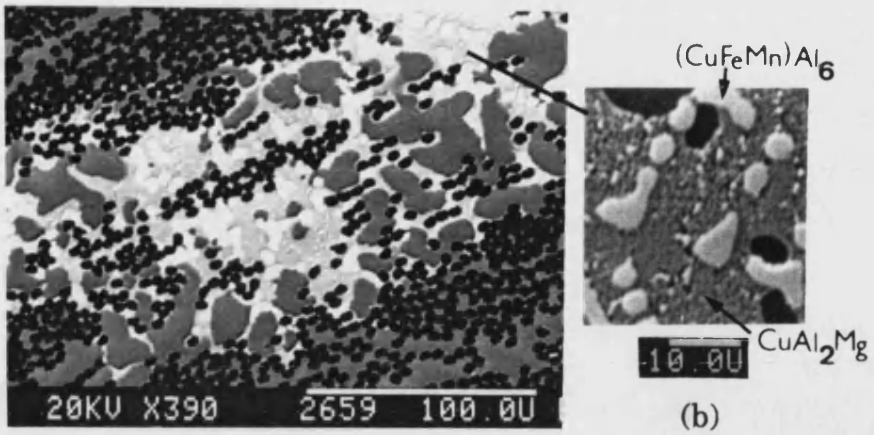

Fig.4.14 SEM micrograph of matrix-rich region in 2124-C

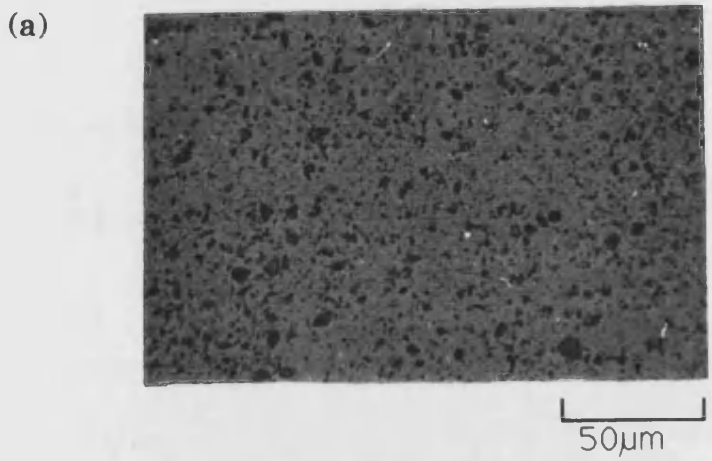

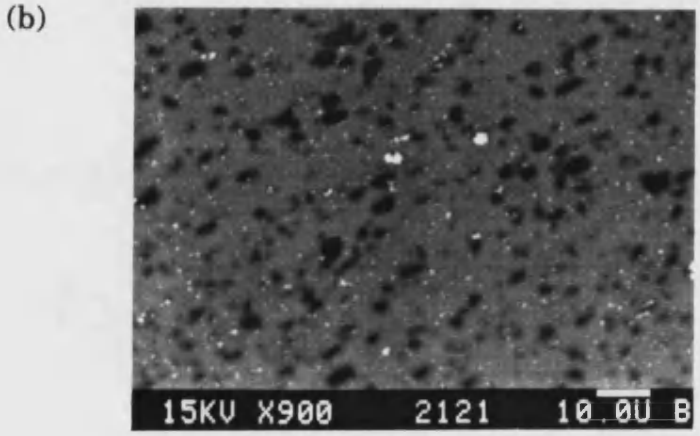

Fig.4.15 2124-SiC
(a) Optical micrograph
(b) SEM micrograph showing the presence second phases (white particles)

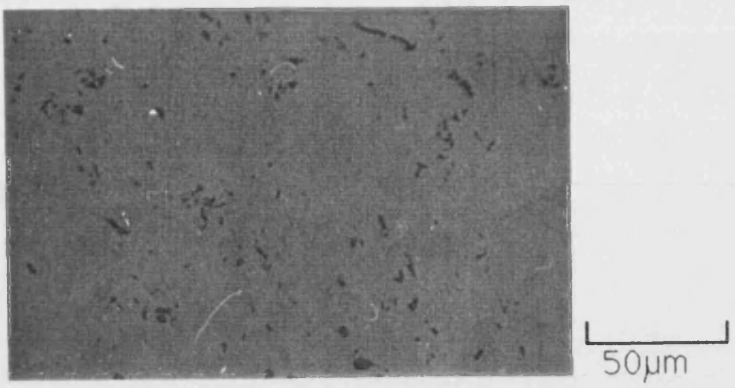

Fig.4.16 Optical micrograph of commercial purity aluminium

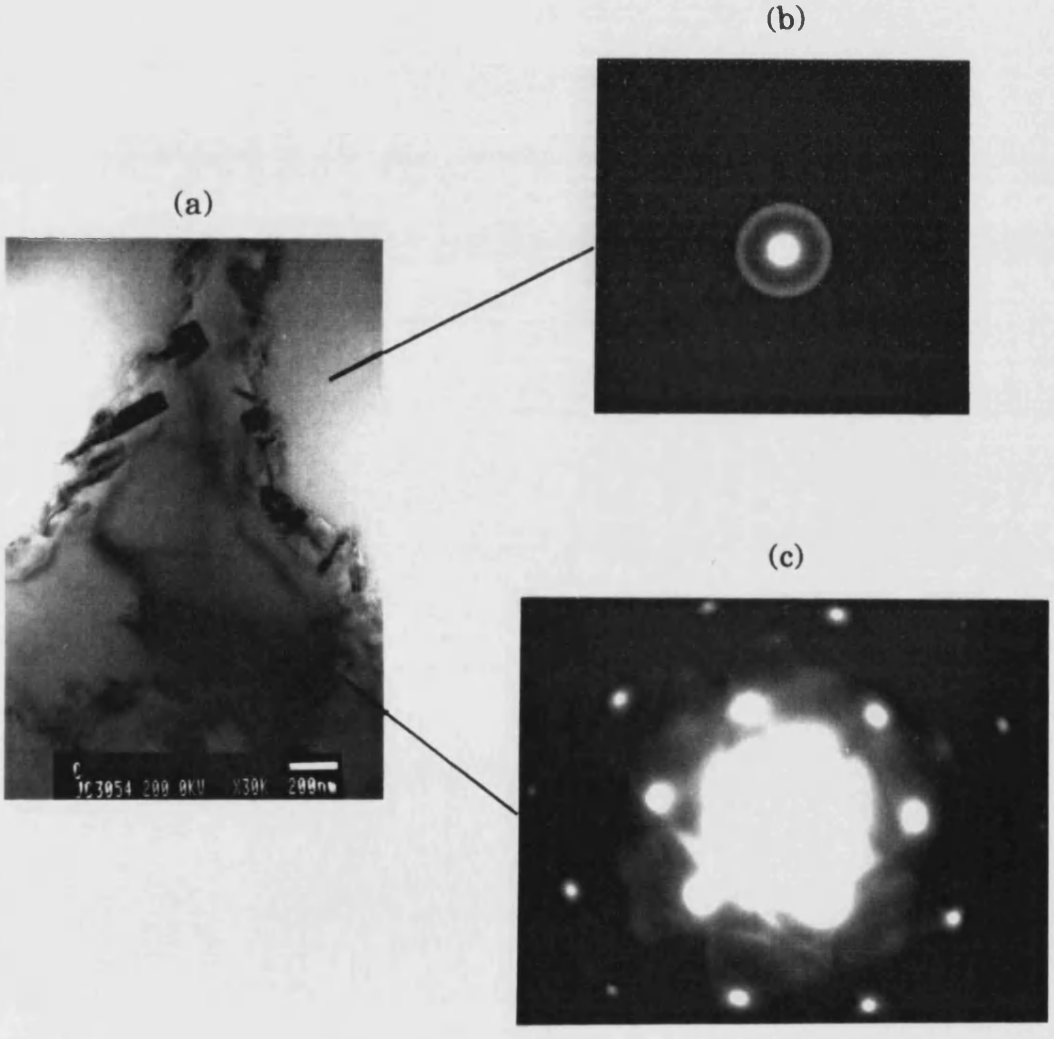

Fig.4.17 (a) TEM micrograph of crystals at the fibre/matrix interface in Al-C
(b) SAD pattern of carbon fibre
(c) SAD pattern of aluminium matrix

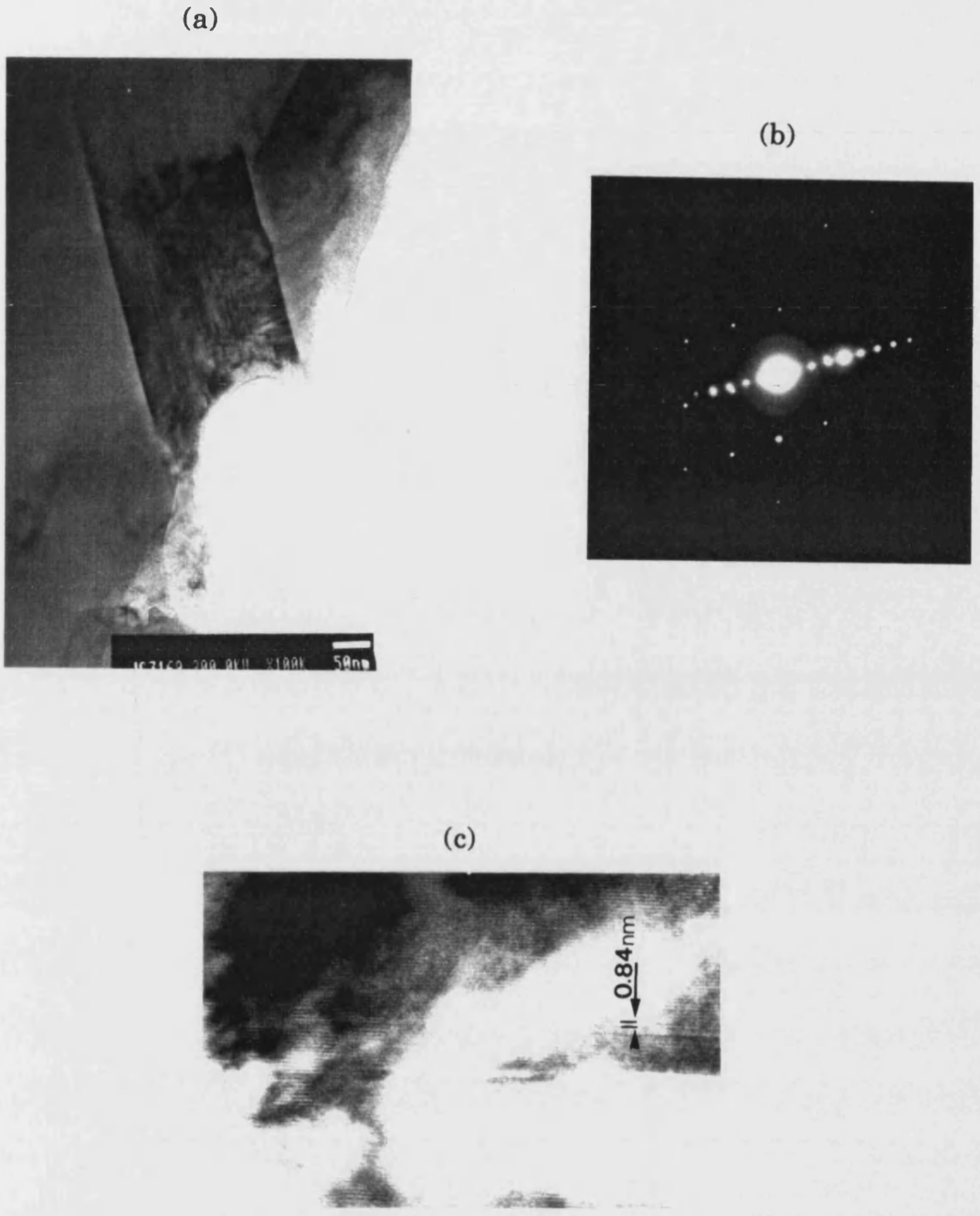

Fig.4.18 (a) Crystal at the fibre/matrix interface in Al-C
(b) SAD pattern of crystal in (a)
(c) Lattice image of a crystal

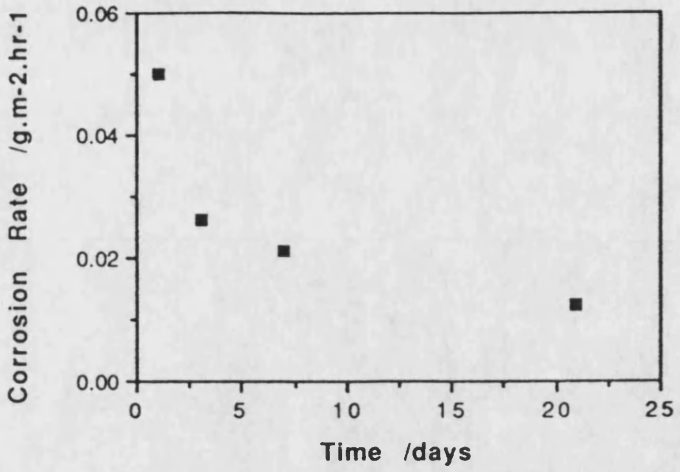

Fig.4.19 The variation of corrosion rate with immersion time for 357 alloy

(a)

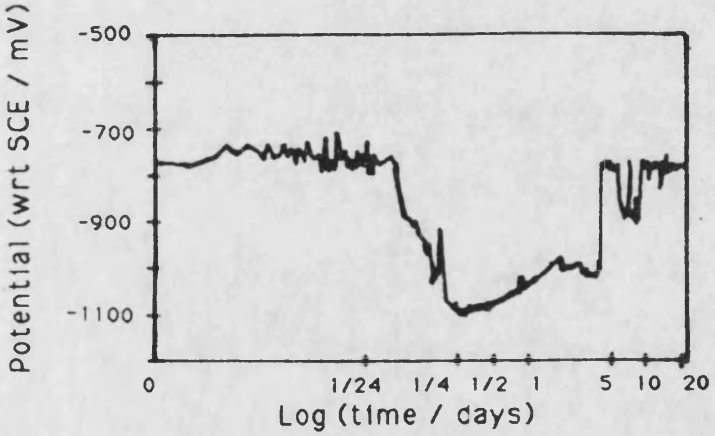

(b)

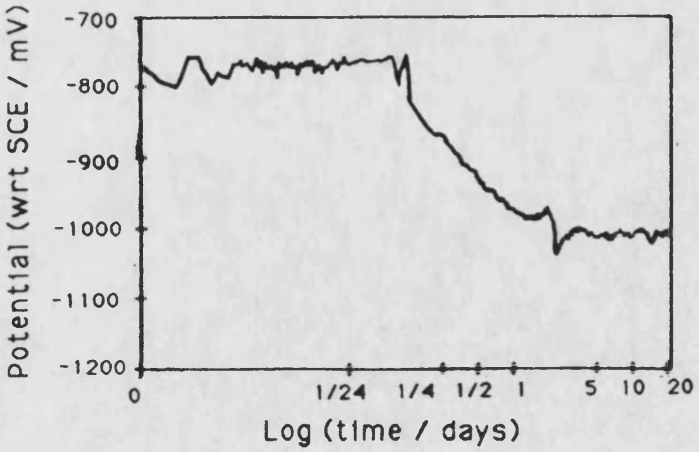

Fig.4.20 (a) The variations of OCP with time exhibited by two specimens of 357 alloy
(b) The variation of OCP with time exhibited by one specimens of 357 alloy

(a)

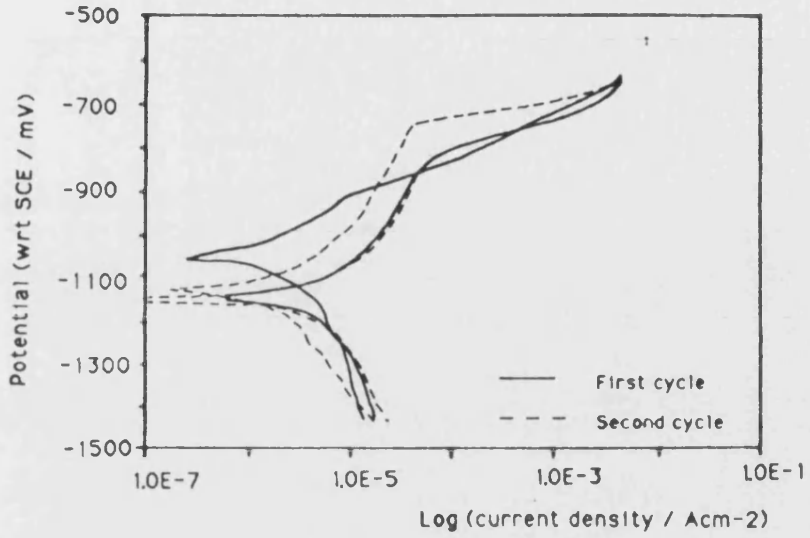

(b)

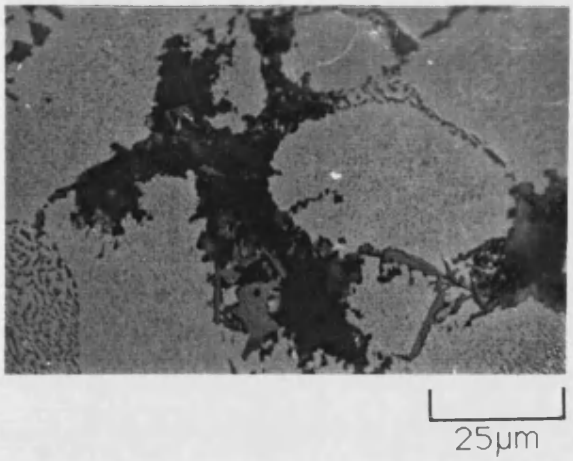

Fig.4.21 The results of DCP tests on 357 alloy (20mV/min scan rate)
(a) DCP curve
(b) Optical micrograph taken after the test

(a)

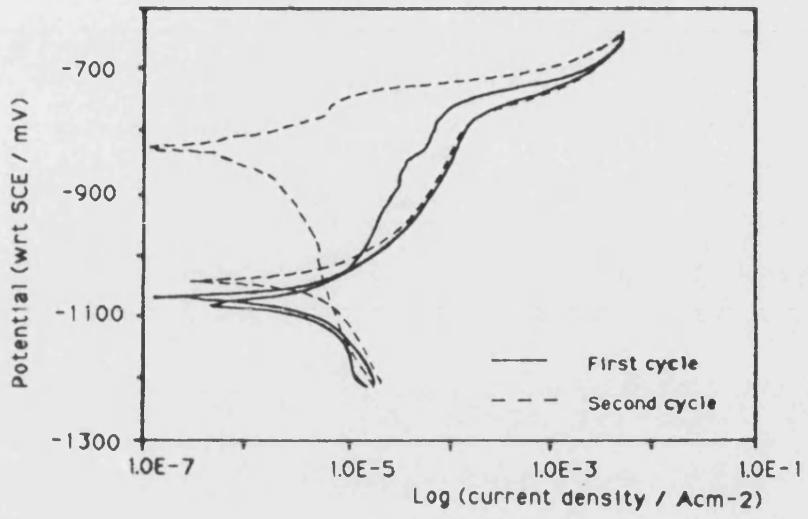

(b)

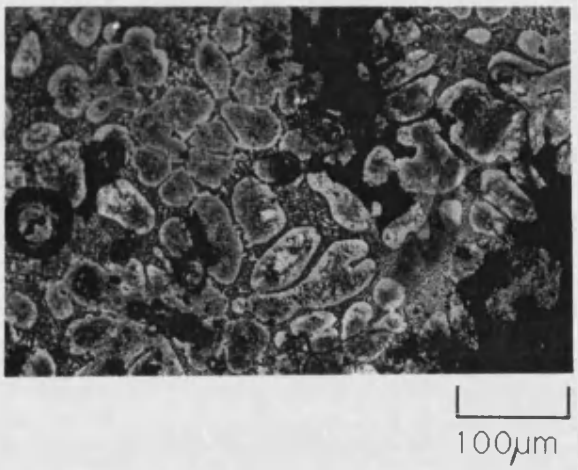

Fig.4.22 The results of DCP tests on 357 alloy (2mV/min scan rate)
(a) DCP curve
(b) Optical micrograph taken after the test

(a)

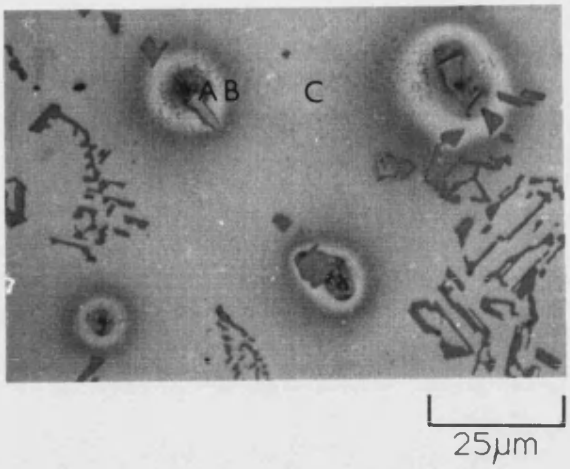

(b)

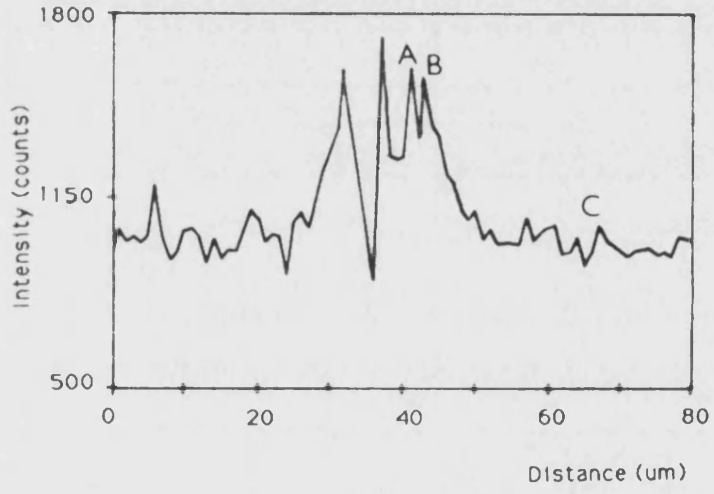

Fig.4.23 (a) Optical micrograph of 357 alloy after 1 hour immersion
(b) Variation of oxygen intensity across a corrosion pit in 357 alloy formed after 1 hour immersion

(a)

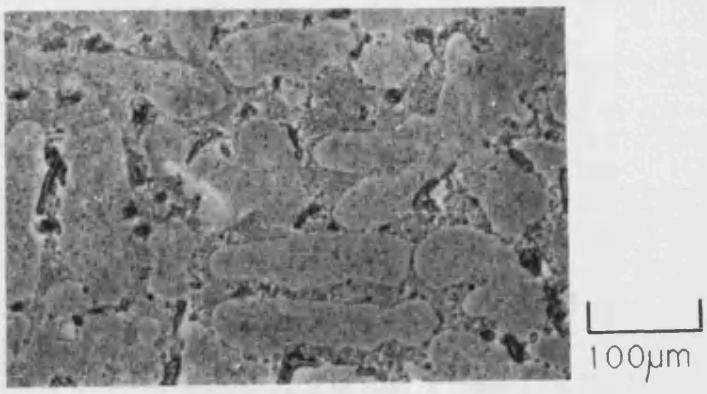

(b)

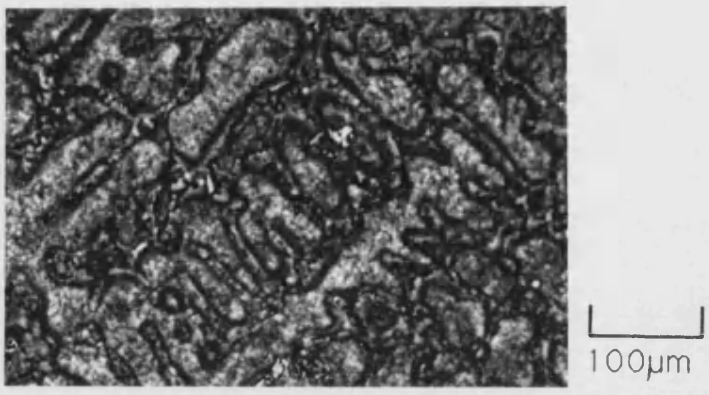

(c)

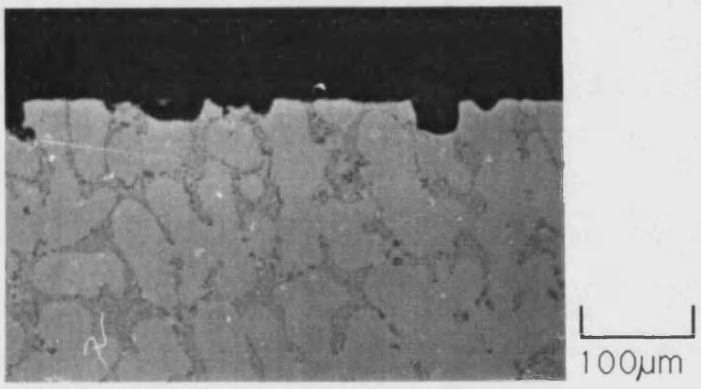

Fig.4.24 Optical micrographs of 357 alloy
(a) After 3 days immersion
(b) After 3 weeks immersion
(c) Cross-section through the specimen after 3 weeks immersion

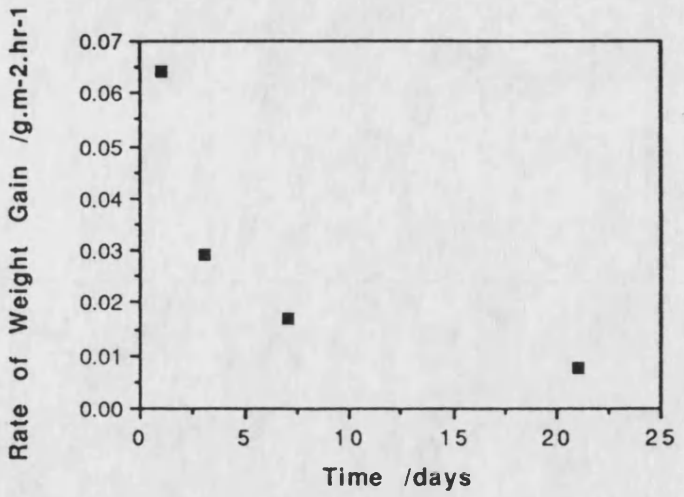

Fig.4.25 The variation in rate of weight gain with immersion time for 357-C_L

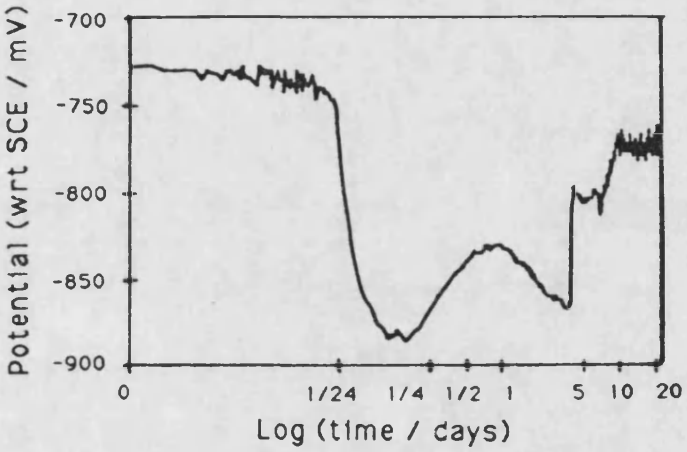

Fig.4.26 The variation of OCP with time for 357-C_L

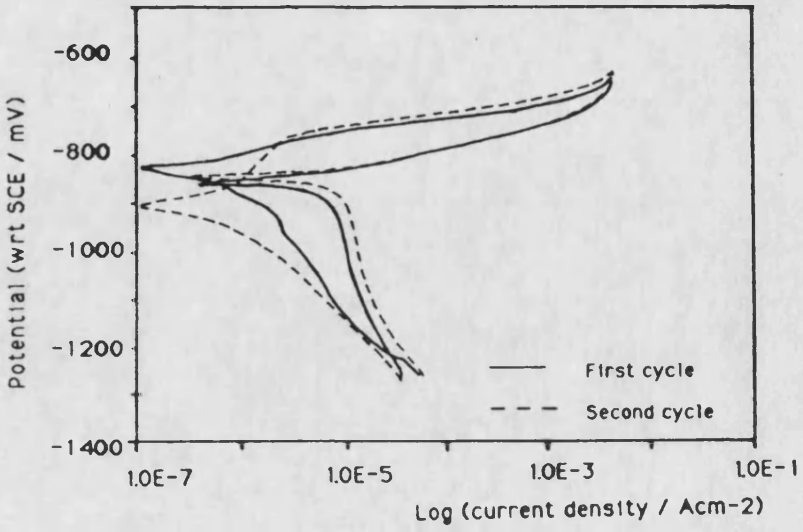

Fig.4.27 DCP curve for 357-C_L (20mV/min scan rate)

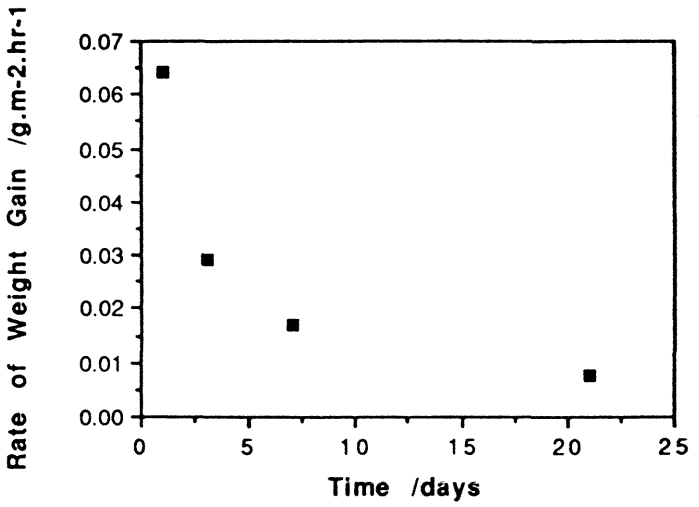

Fig.4.25 The variation in rate of weight gain with immersion time for 357-C_L

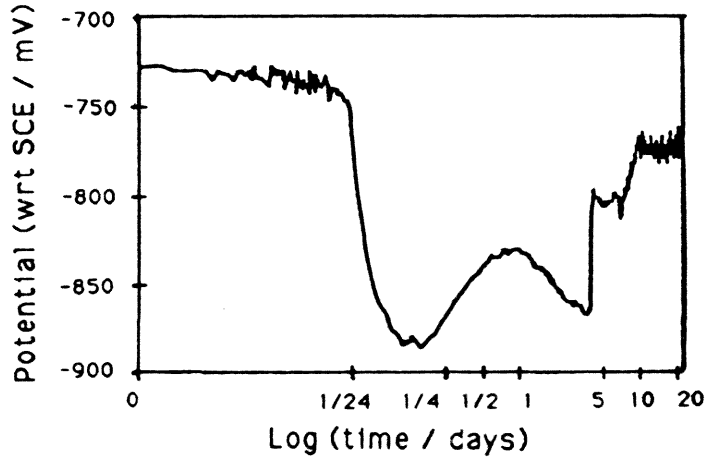

Fig.4.26 The variation of OCP with time for 357-C_L

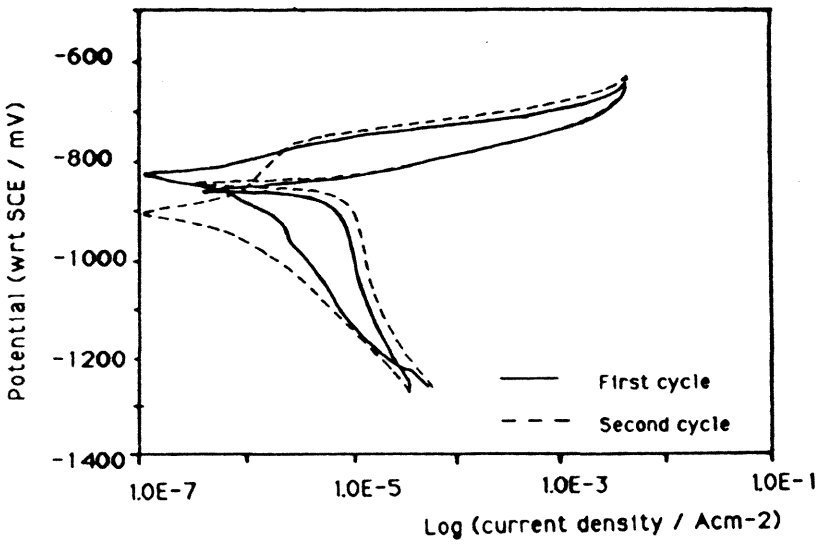

Fig.4.27 DCP curve for 357-C_L (20mV/min scan rate)

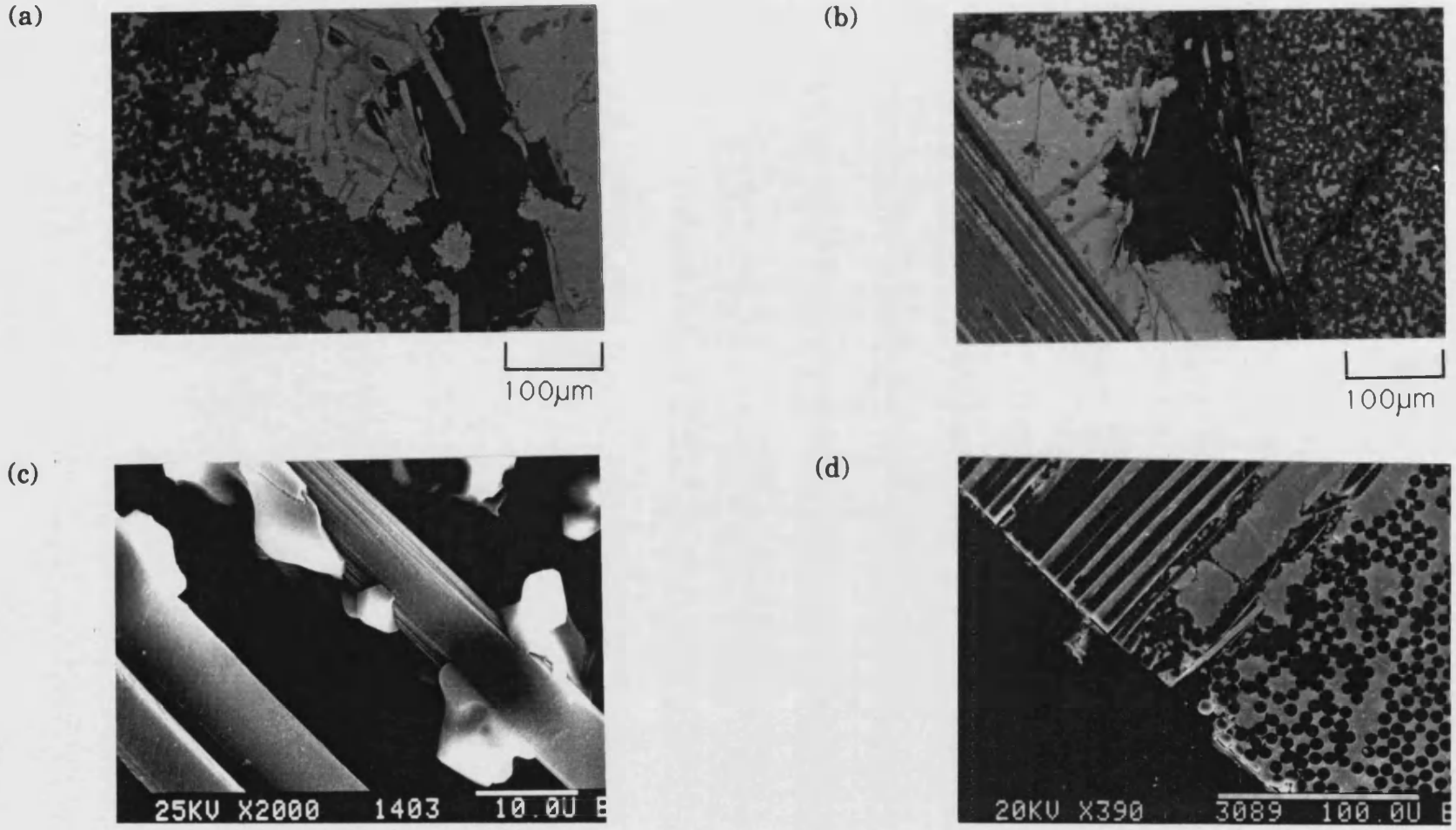

Fig.4.28 Corrosion morphology of 357-C_L after DCP test
(a) Corrosion pit at intermetallic phases at the edge of fibre tow
(b) Corrosion at glass fibre weft
(c) Silicon particles attached to carbon fibres
(d) Cross-section through a specimen

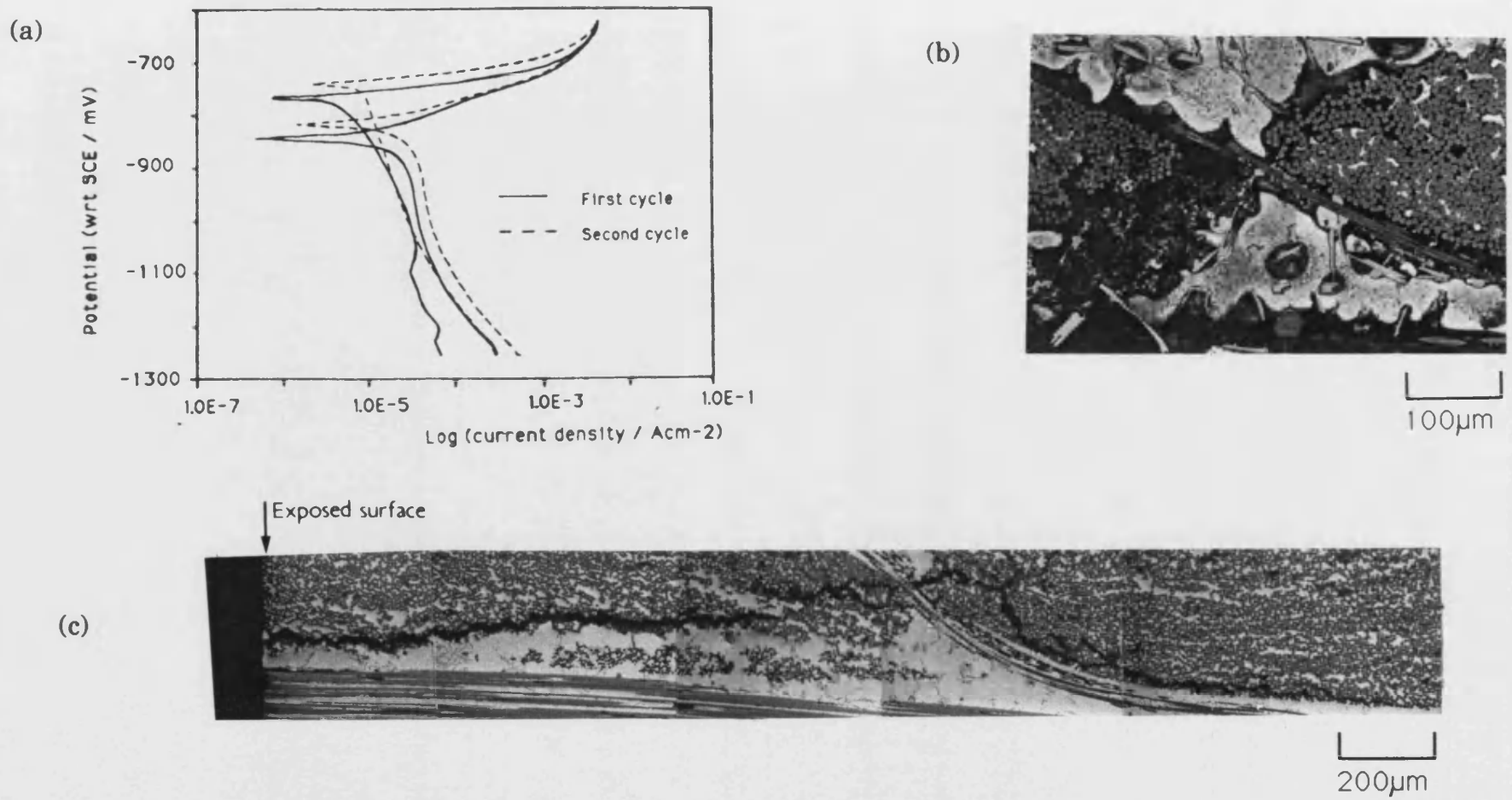

Fig.4.29 The results of DCP tests on 357-C_L (2mV/min scan rate)
(a) DCP curve
(b) Optical micrograph taken after the test
(c) Cross-section through the specimen

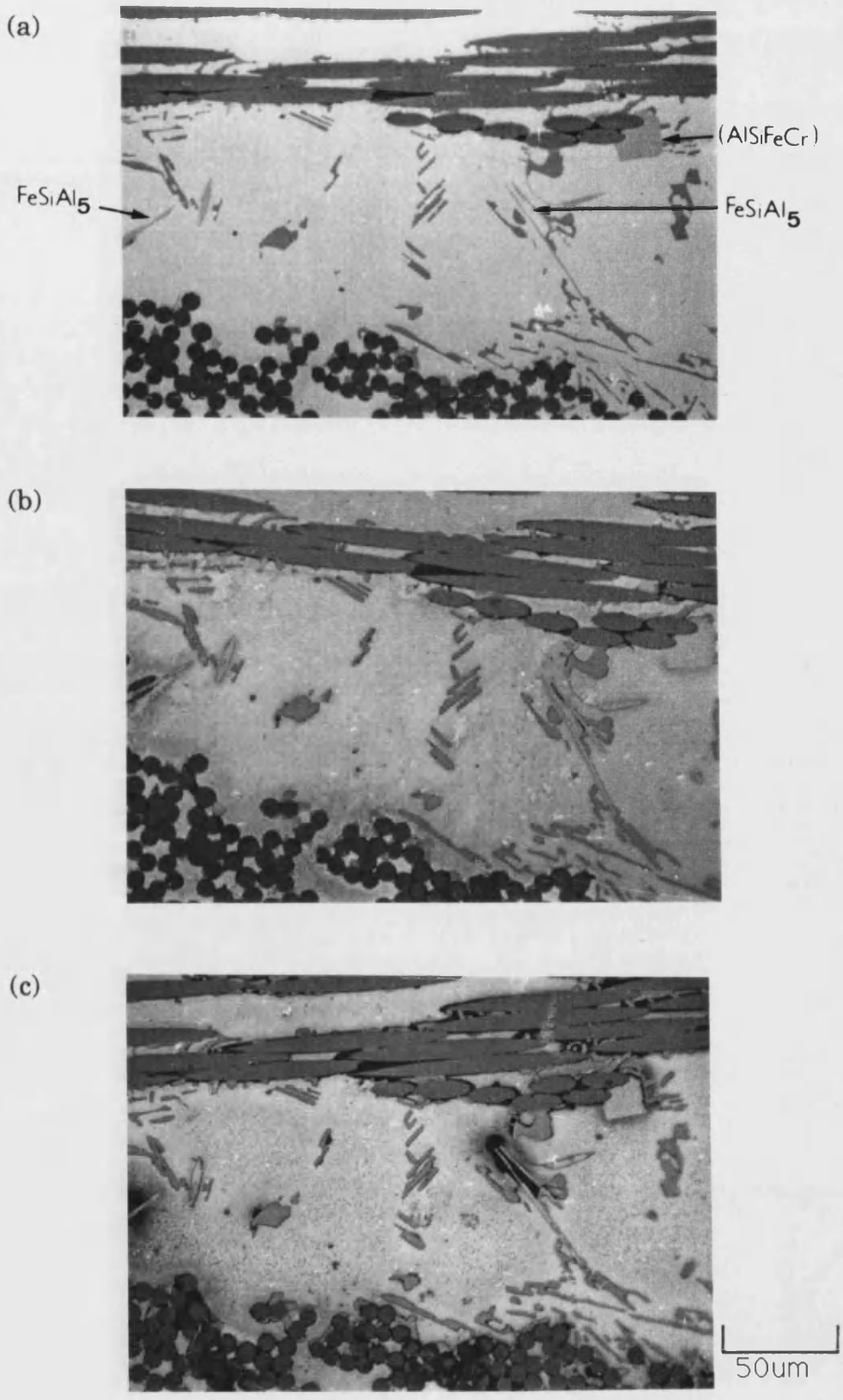

Fig.4.30 Optical micrographs of an area of 357-C_L
(a) Before immersion
(b) After 6 hours immersion
(c) After 1 day immersion

(a)

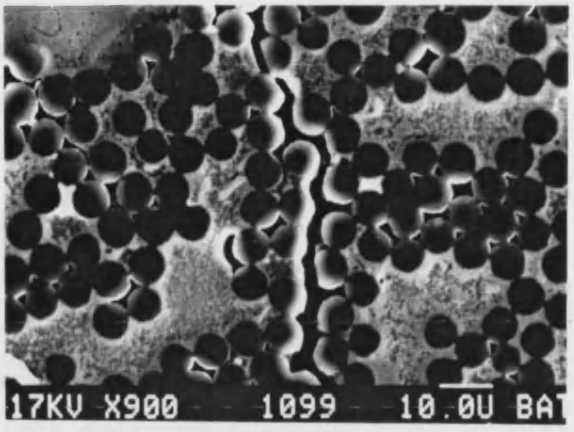

(b)

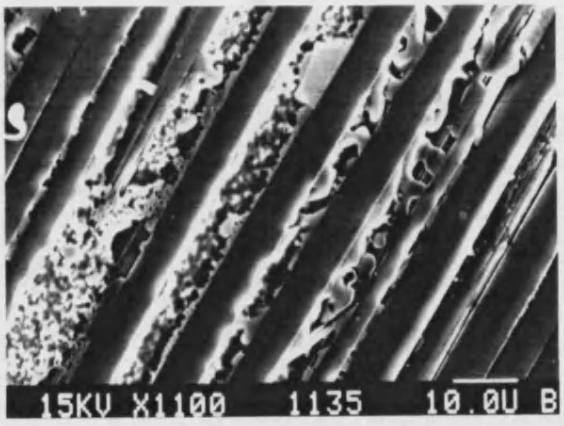

Fig.4.31 Corrosion morphology of 357-C_L
(a) After 1 day immersion
(b) After 3 days immersion

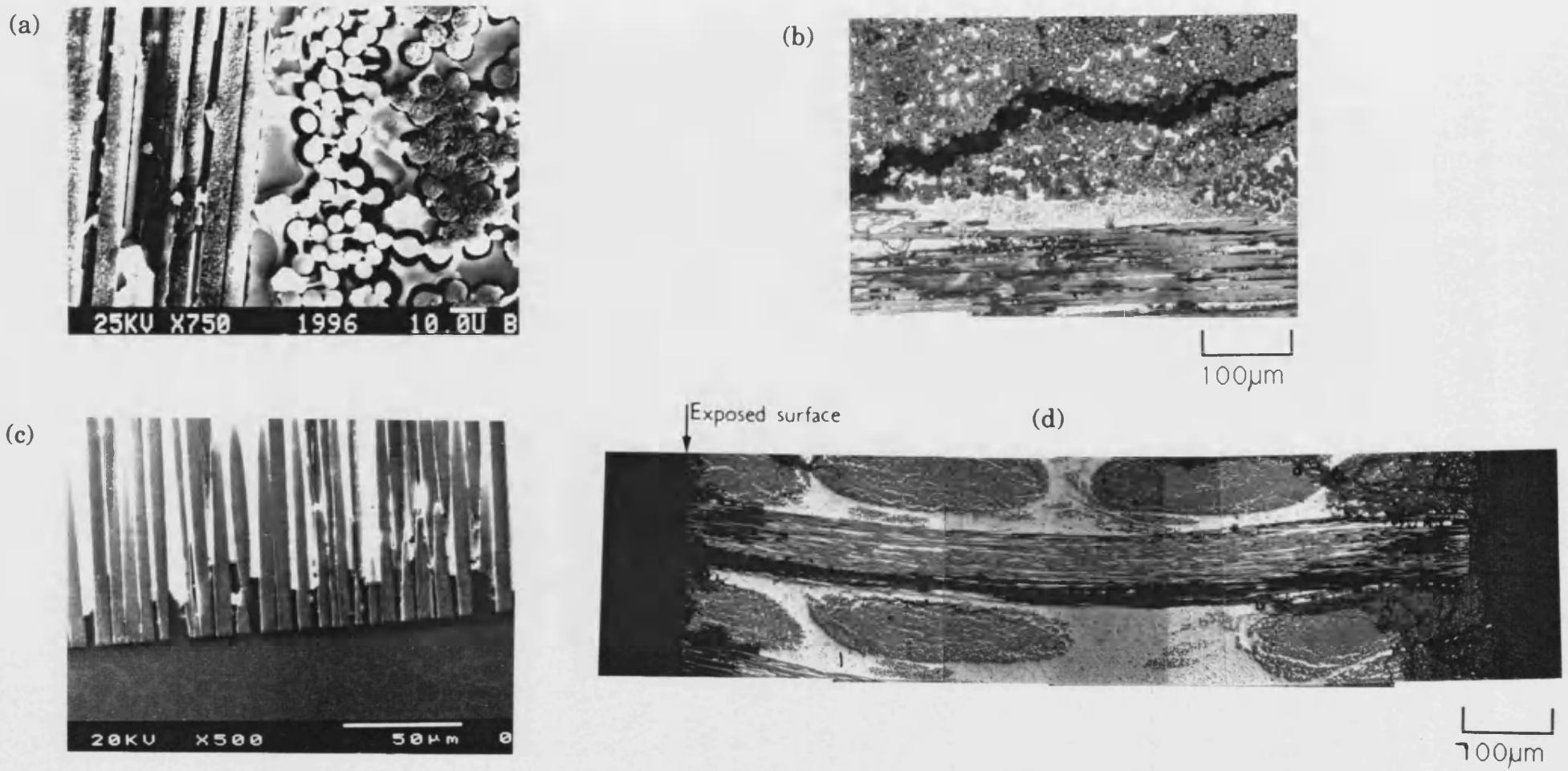

Fig.4.32 Corrosion morphology of 357-C_L after 3 weeks corrosion
(a) Corrosion around carbon and weft fibres
(b) Crack running through fibre tow
(c) Cross-section through the corroded specimen
(d) Cross-section showing complete penetration of corrosion through the specimen

(a)

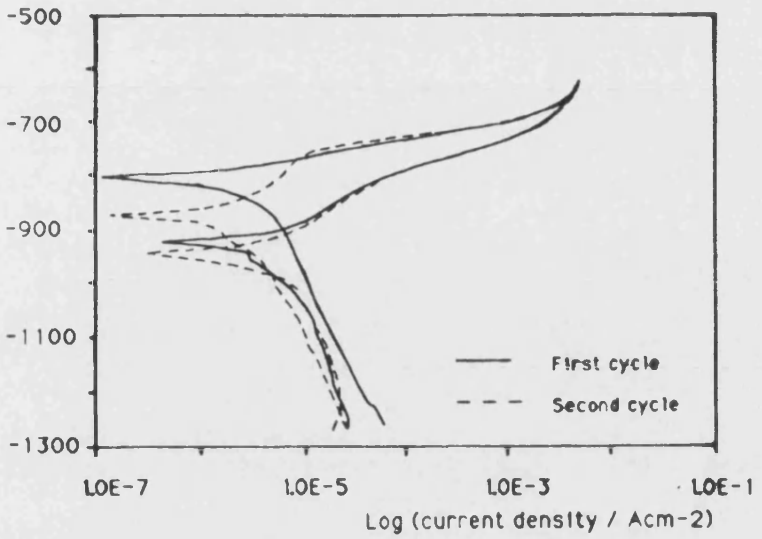

(b)

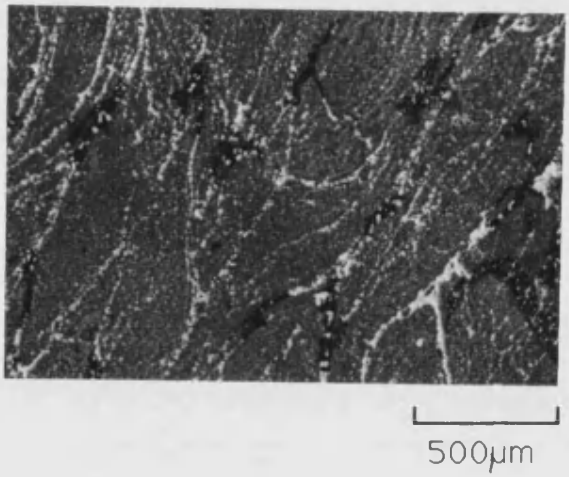

Fig.4.33 The results of DCP tests on 357-C_S (20mV/min scan rate)
(a) DCP curve
(b) Optical micrograph taken after the test

(a)

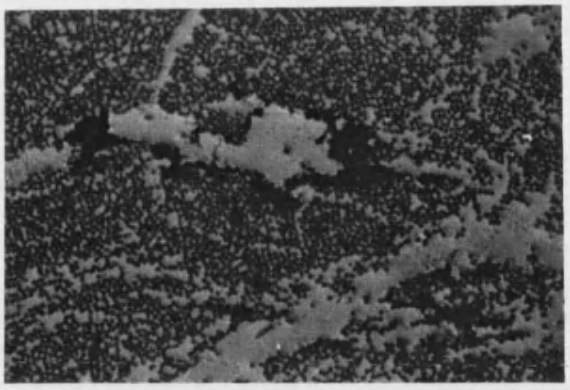

200μm

(b)

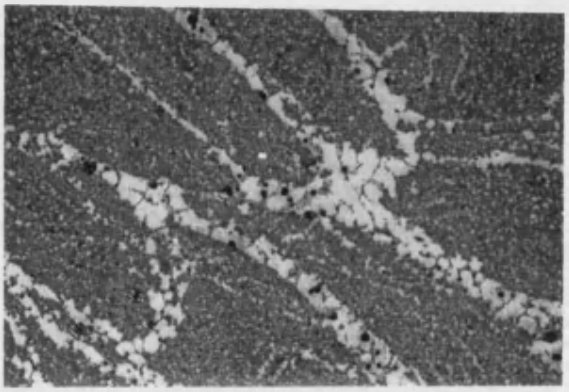

500μm

Fig.4.34 Corrosion morphology of 357-C_S
(a) After 1 day immersion
(b) After 3 days immersion

(a)

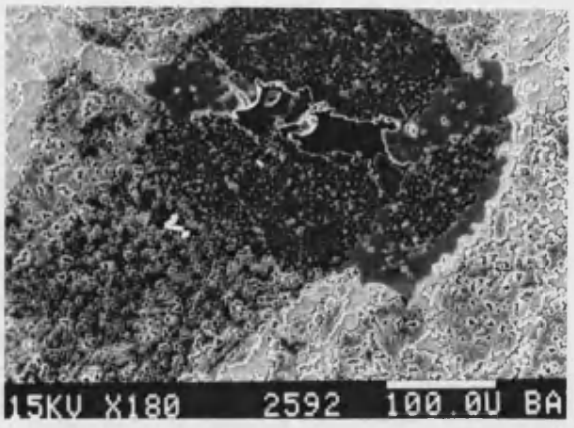

(b)

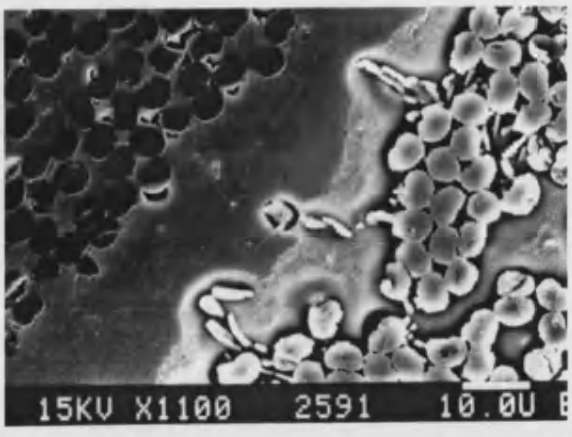

(c)

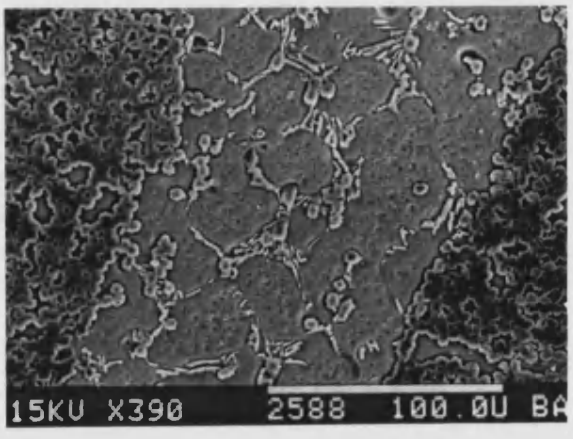

Fig.4.35 Corrosion morphology of 357-C_S after 1 week immersion
(a) Corrosion pit surrounded by an unattacked region
(b) Edge of an uncorroded and corroded region
(c) Corrosion around second phases in matrix-rich region

(a)

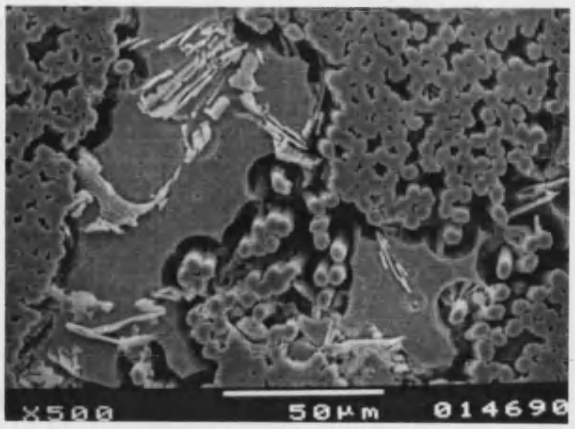

(b)

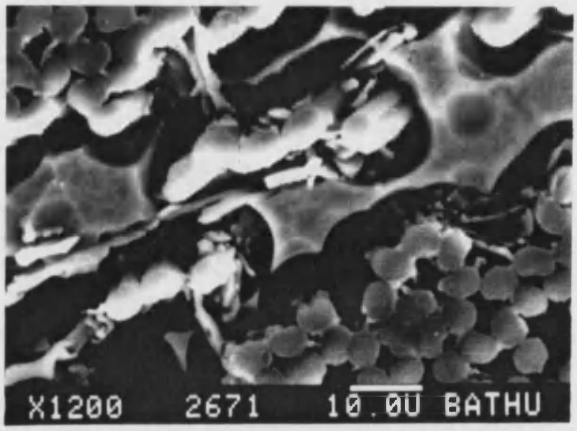

(c)

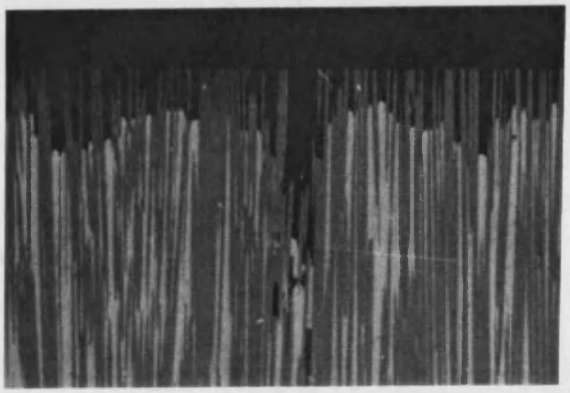

Fig.4.36 Corrosion morphology of 357-C_S after 3 weeks immersion
(a) Corrosion at the fibre/matrix interface
(b) Silicon particles attached to fibres
(c) Cross-section through a corroded specimen

(a)

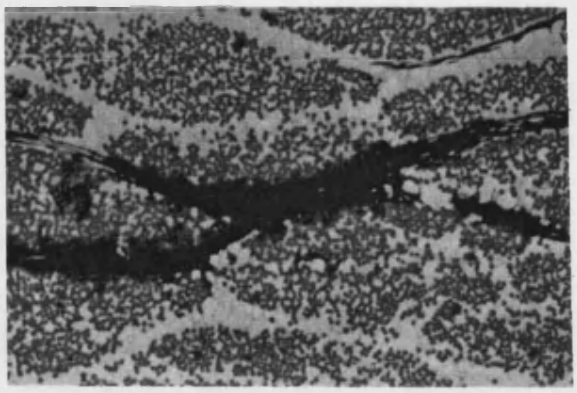

(b)

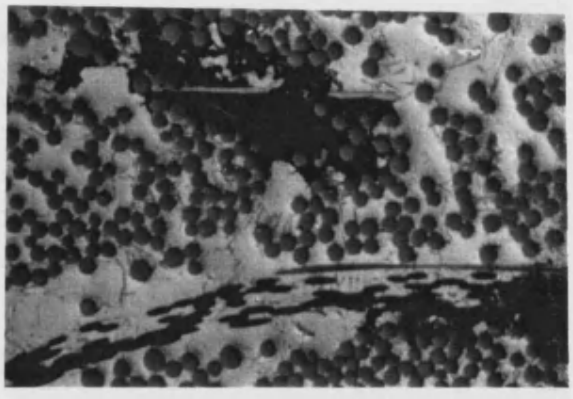

Fig.4.37 Corrosion morphology of 357-Nic (type A) after DCP test (20mV/min scan rate)
(a) Corrosion around the glass weft
(b) Corrosion pit at $FeSiAl_5$ intermetallic

(a)

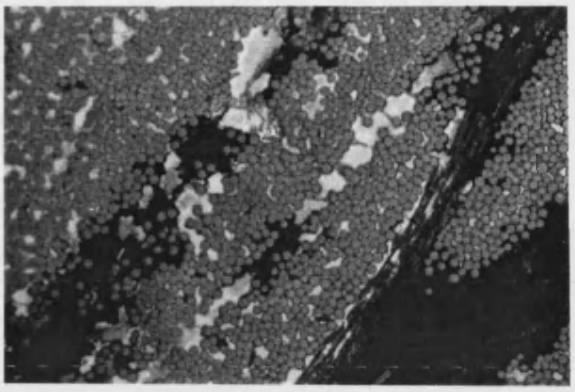

(b)

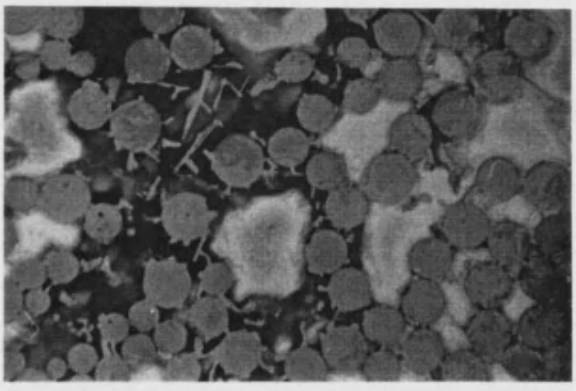

Fig.4.38 Corrosion morphology of 357-Nic (type A) after DCP test (2mV/min scan rate)
(a) Corrosion at the glass-fibre weft and matrix-rich regions
(b) Corrosion at the fibre/matrix interface

(a)

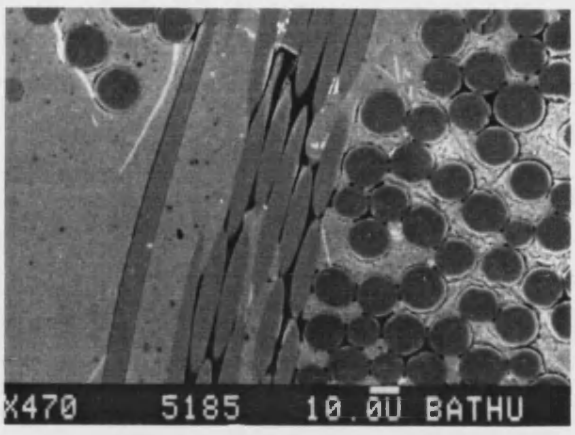

(b)

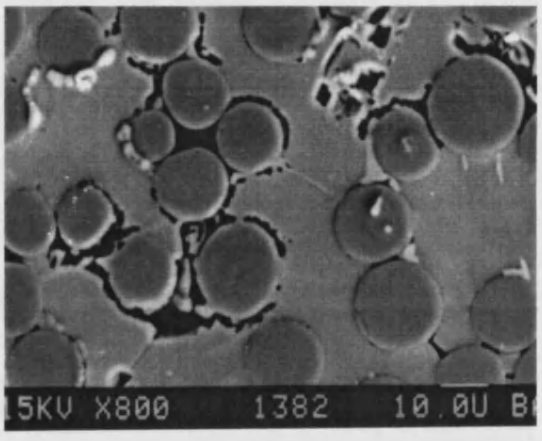

Fig.4.39 Corrosion morphology of 357-Nic after 1 day immersion
(a) Corrosion around glass-weft (type A)
(b) Corrosion at fibre/matrix interface (type B)

(a)

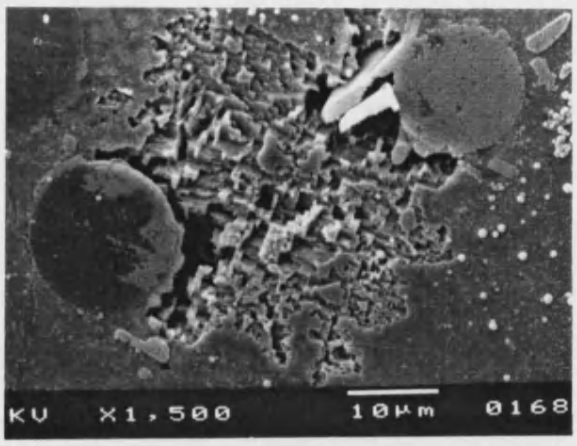

(b)

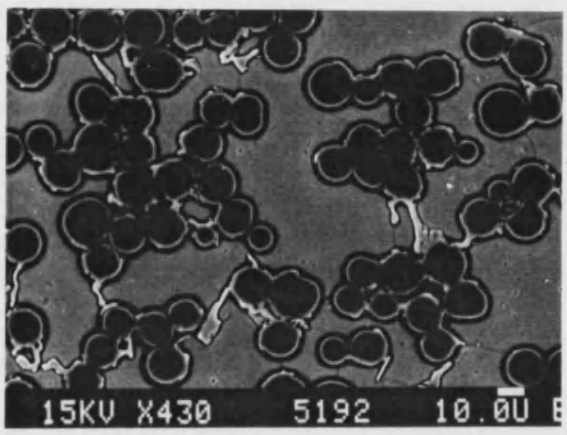

Fig.4.40 Corrosion morphology of 357-Nic after 1 week immersion
(a) Corrosion at $FeSiAl_5$ intermetallic (type A)
(b) Corrosion around fibres and silicon particles (type B)

(a)

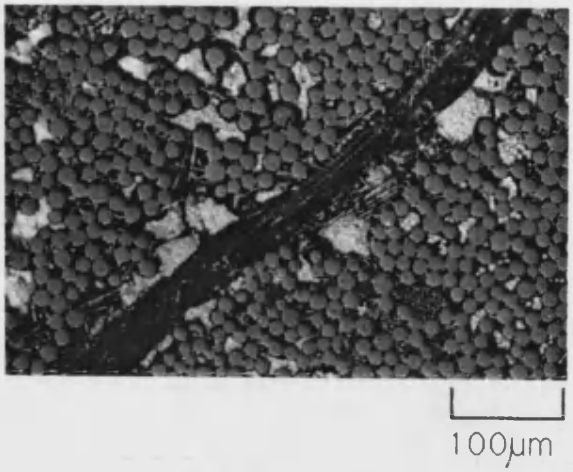

(b)

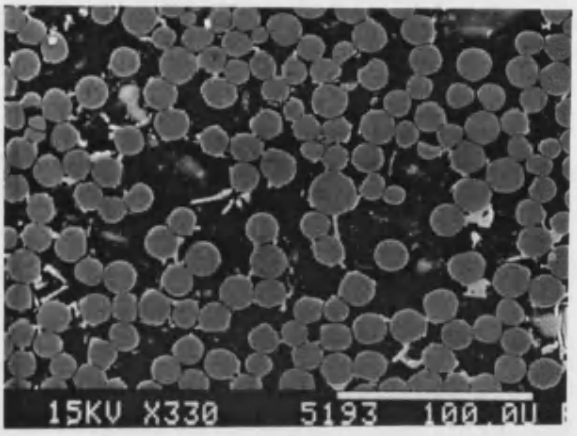

(c)

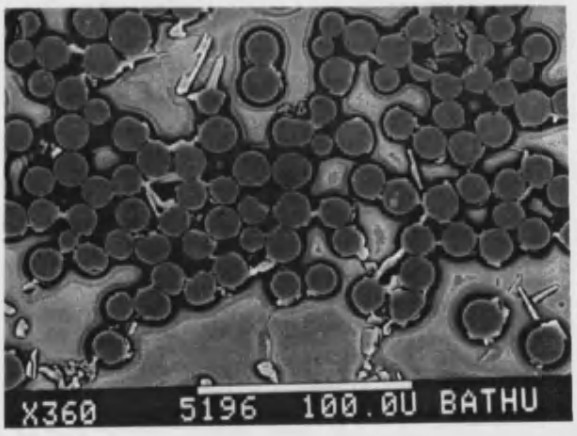

Fig.4.41 Corrosion morphology of 357-Nic after 3 weeks immersion
(a) Corrosion at glass-fibre weft (type A)
(b) Severe corrosion around fibres (type B)
(c) Less extensive corrosion around fibres (type B)

(a)

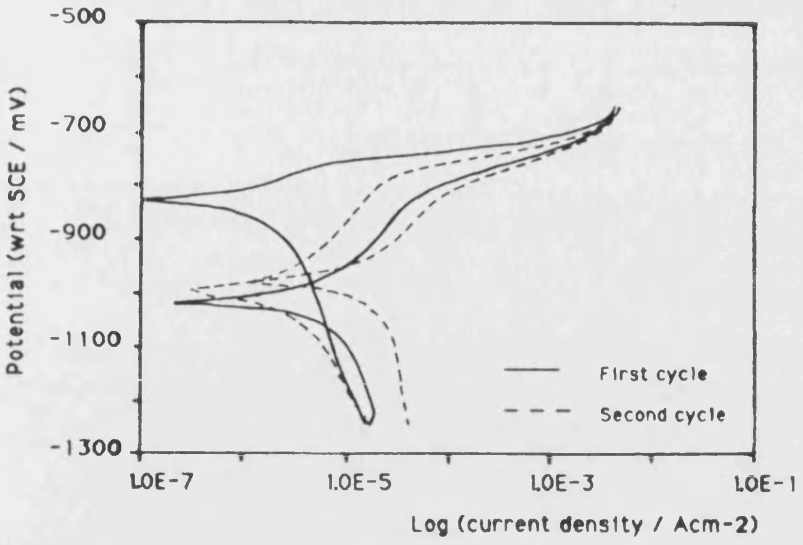

(b)

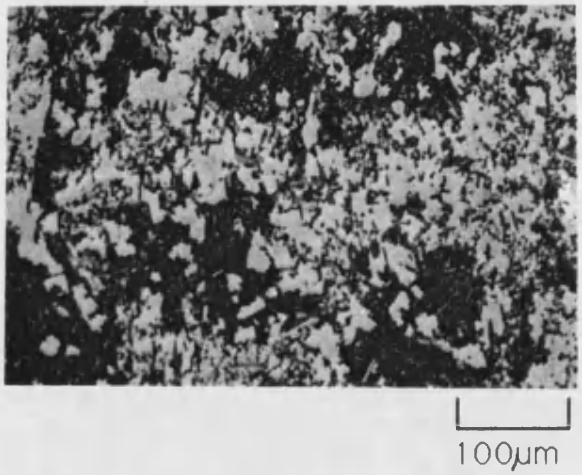

(c)

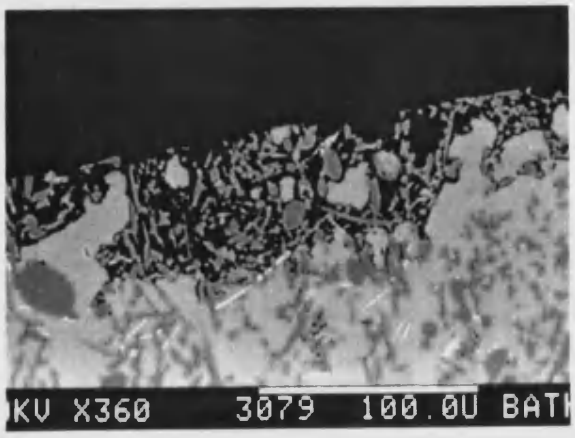

Fig.4.42 The results of DCP tests on 357-Saf (20mV/min scan rate)
(a) DCP curve
(b) Optical micrograph taken after the test
(c) Cross-section through a corroded specimen

(a)

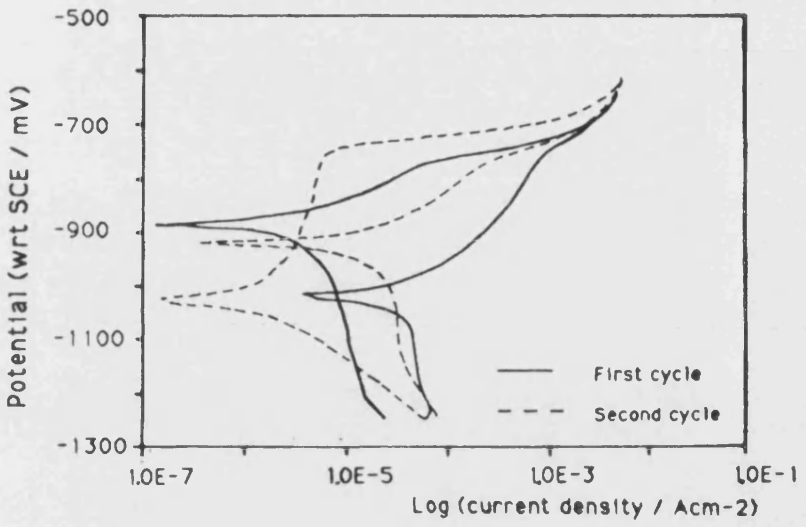

(b)

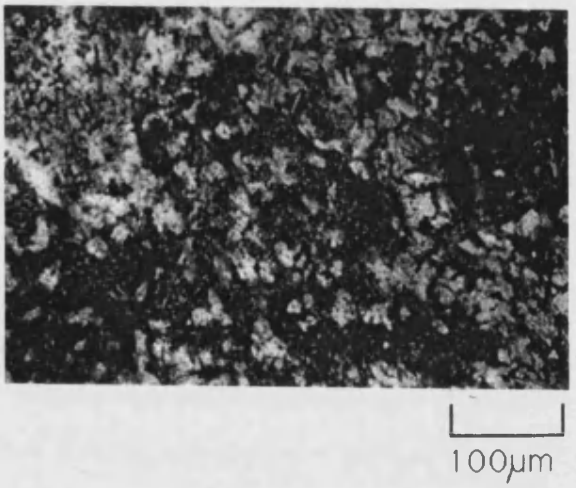

Fig.4.43 The results of DCP tests on 357-Saf (2mV/min scan rate)
(a) DCP curve
(b) Optical micrograph taken after the test

(a)

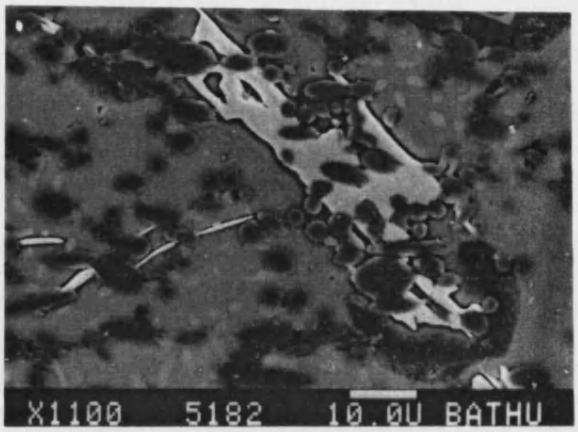

(b)

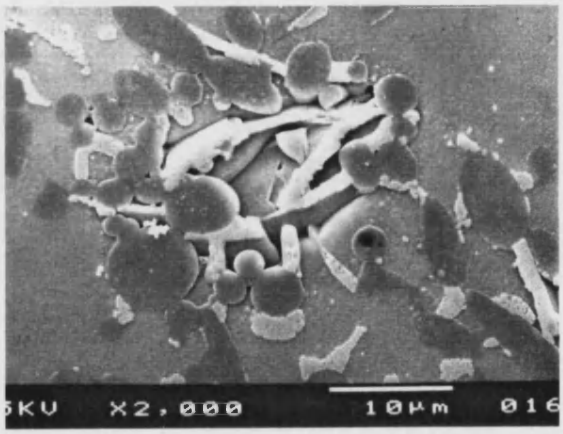

Fig.4.44 Corrosion morphology of 357-Saf
(a) Attack around $FeSiAl_5$ intermetallic phase after 1 day immersion
(b) Corrosion pit at $FeSiAl_5$ after 1 week immersion

(a)

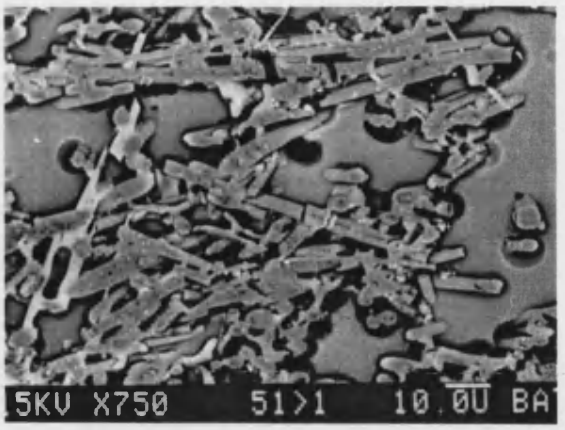

(b)

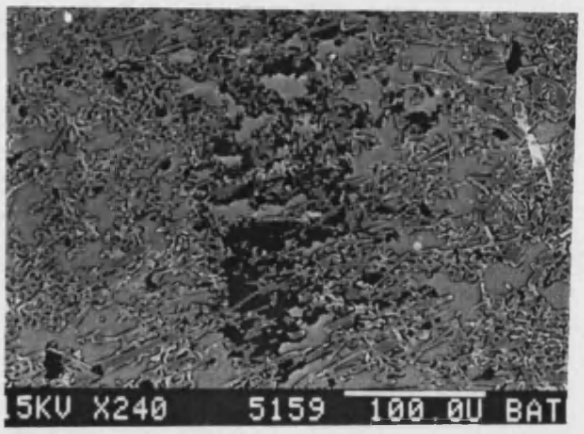

(c)

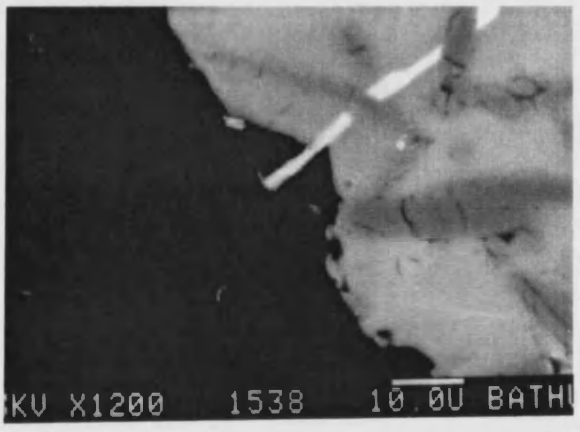

Fig.4.45 Corrosion morphology of 357-Saf after 3 weeks immersion
(a) Corrosion around fibres and second phases
(b) Corrosion pits
(c) Cross-section through a specimen showing a pit initiated at the $FeSiAl_5$ phase

(a)

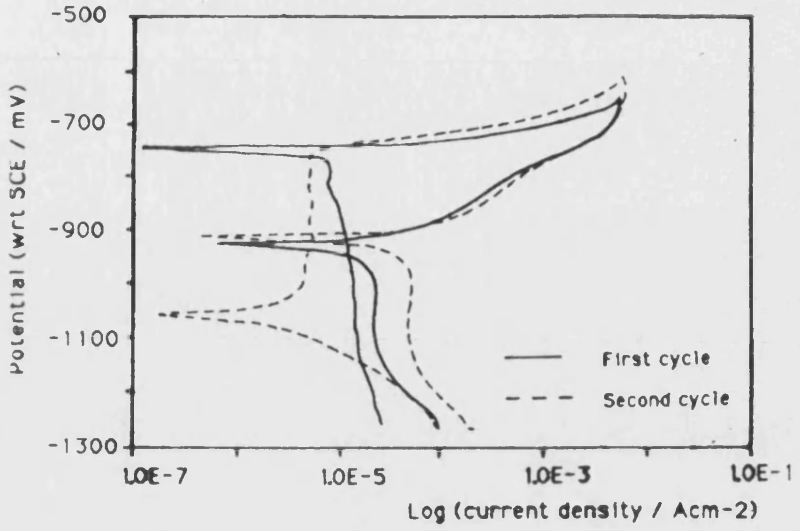

(b)

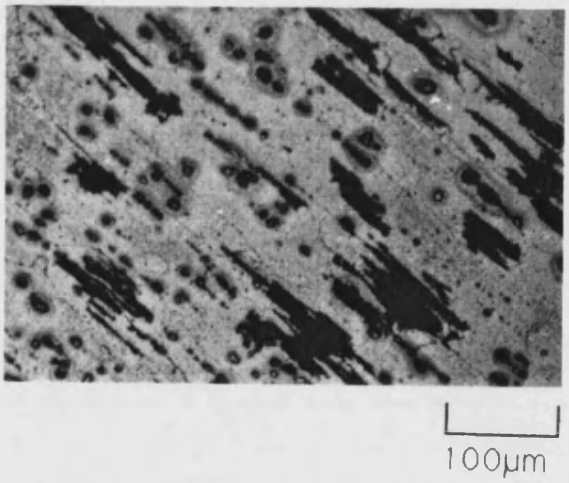

Fig.4.46 The results of DCP tests on 2124 alloy (20mV/min scan rate)
(a) DCP curve
(b) Optical micrograph taken after the test

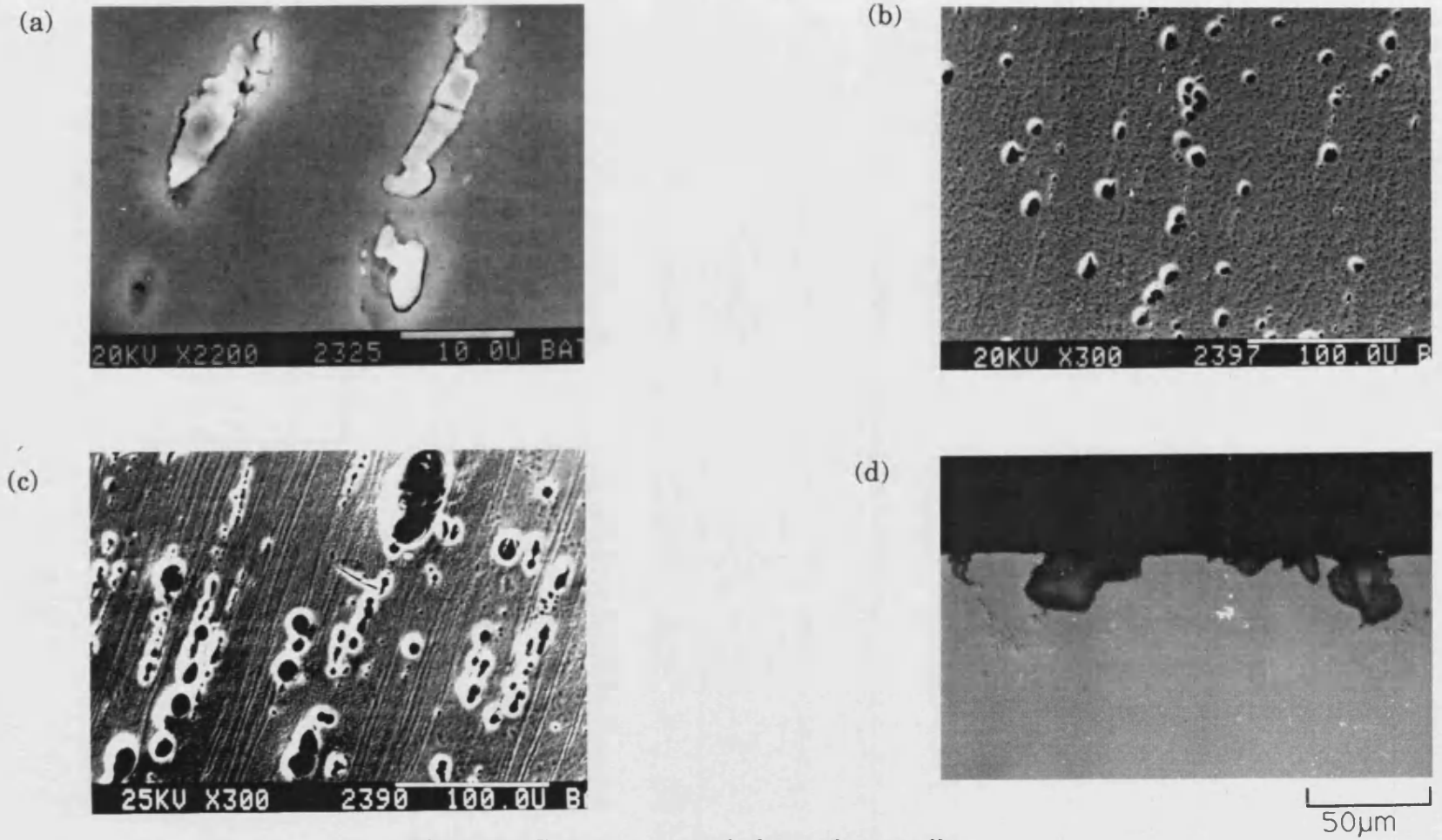

Fig.4.47 Corrosion morphology of 2124 alloy
(a) After 3 days immersion, illustrating corrosion around the (CuFeMn)Al_6 phase
(b) After 1 week immersion
(c) After 3 weeks immersion
(d) Cross-section through a specimen after 3 weeks corrosion

(a)

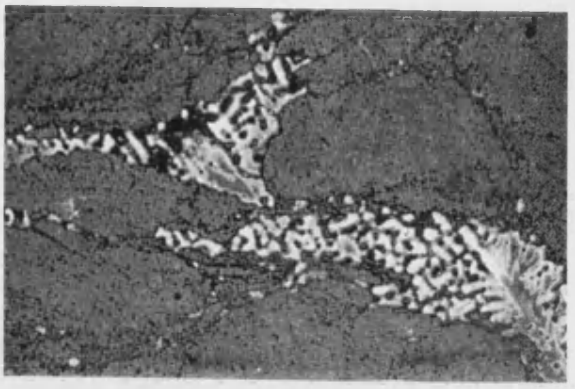

(b)

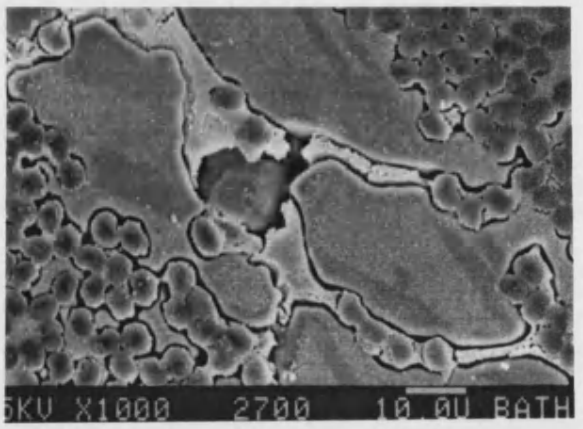

(c)

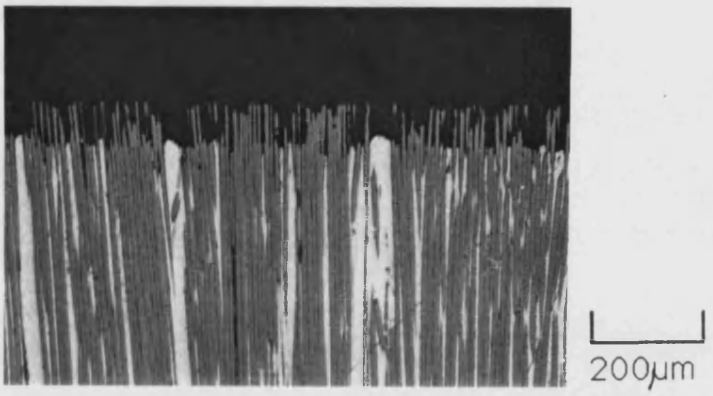

Fig.4.48 The results of DCP tests on 2124-C (20mV/min scan rate)
(a) Corrosion at the second phases in fibre-free regions
(b) Corrosion around Al_2CuMg phase
(c) Cross-section through a corroded specimen

(a)

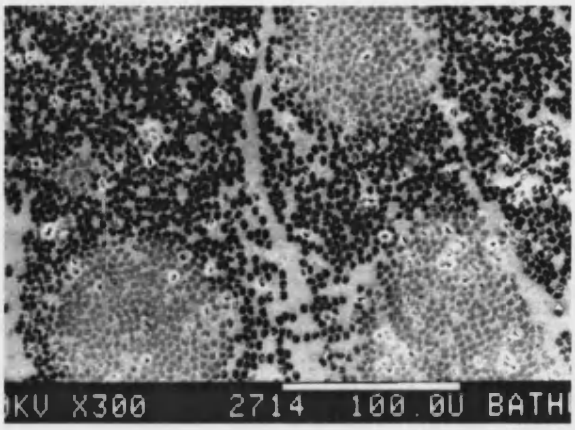

(b)

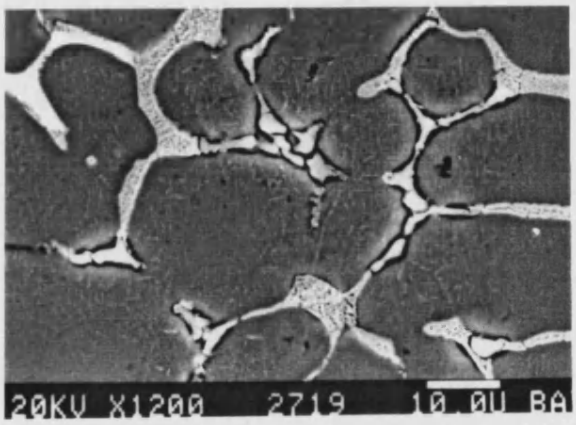

Fig.4.49 Corrosion morphology of 2124-C after 1 day immersion
(a) Small pits between fibres covered by corrosion film
(b) Preferential attack around the (CuFeMn)Al_6 phase

(a)

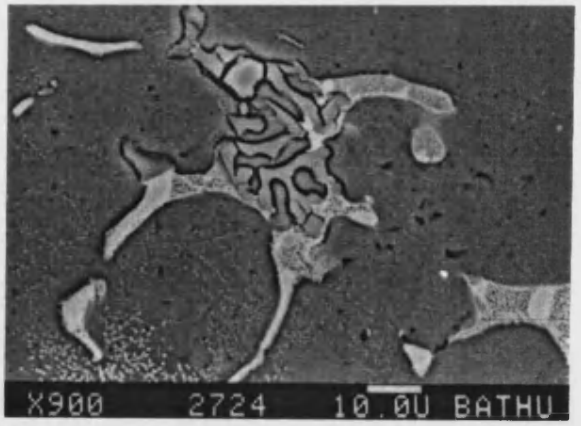

(b)

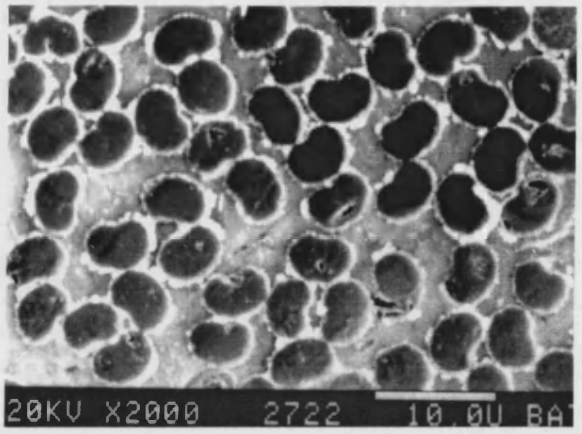

(c)

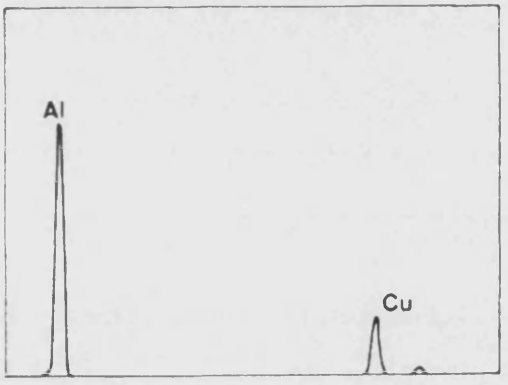

Fig.4.50 Corrosion morphology of 2124-C after 3 days immersion
(a) Preferential attack around the $(CuFeMn)Al_6$ phase
(b) White phase surrounding fibres
(c) EDS analysis of white phase in (b)

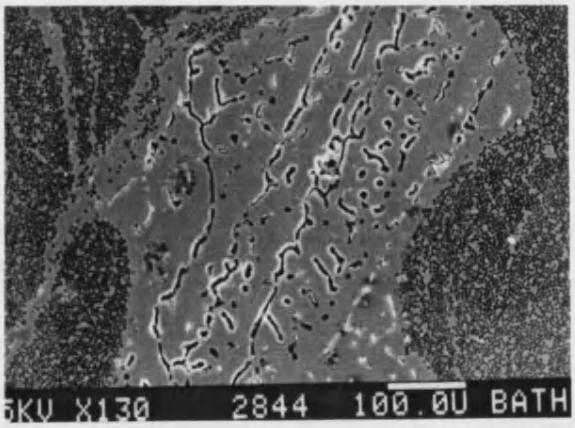

Fig.4.51 Corrosion around second phases in a fibre-free region of 2124-C

(a)

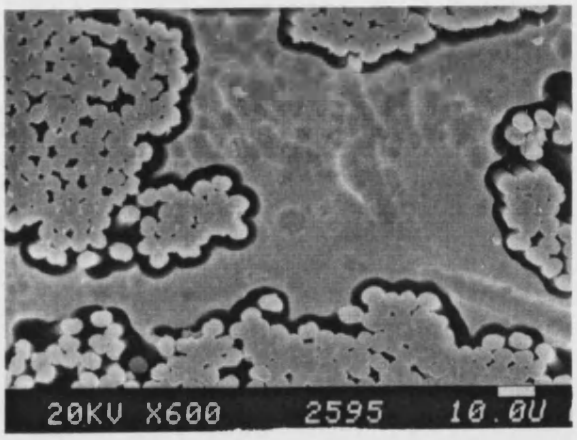

(b)

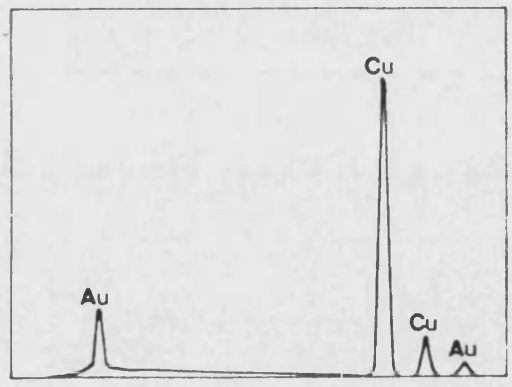

Fig.4.52 (a) 2124-C after 3 weeks immersion; corrosion around fibres
(b) EDS analysis of white phase around fibres (see Fig.4.50(b))

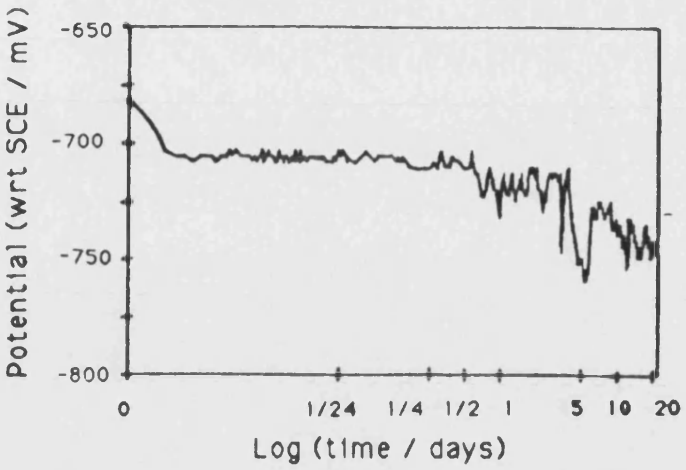

Fig.4.53 The variation in OCP for a specimen of 2124-SiC

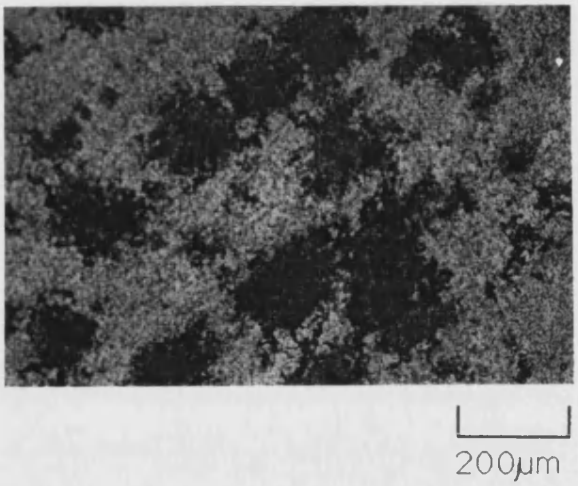

Fig.4.54 Corrosion morphology of 2124-SiC after DCP test (20mV/min scan rate)

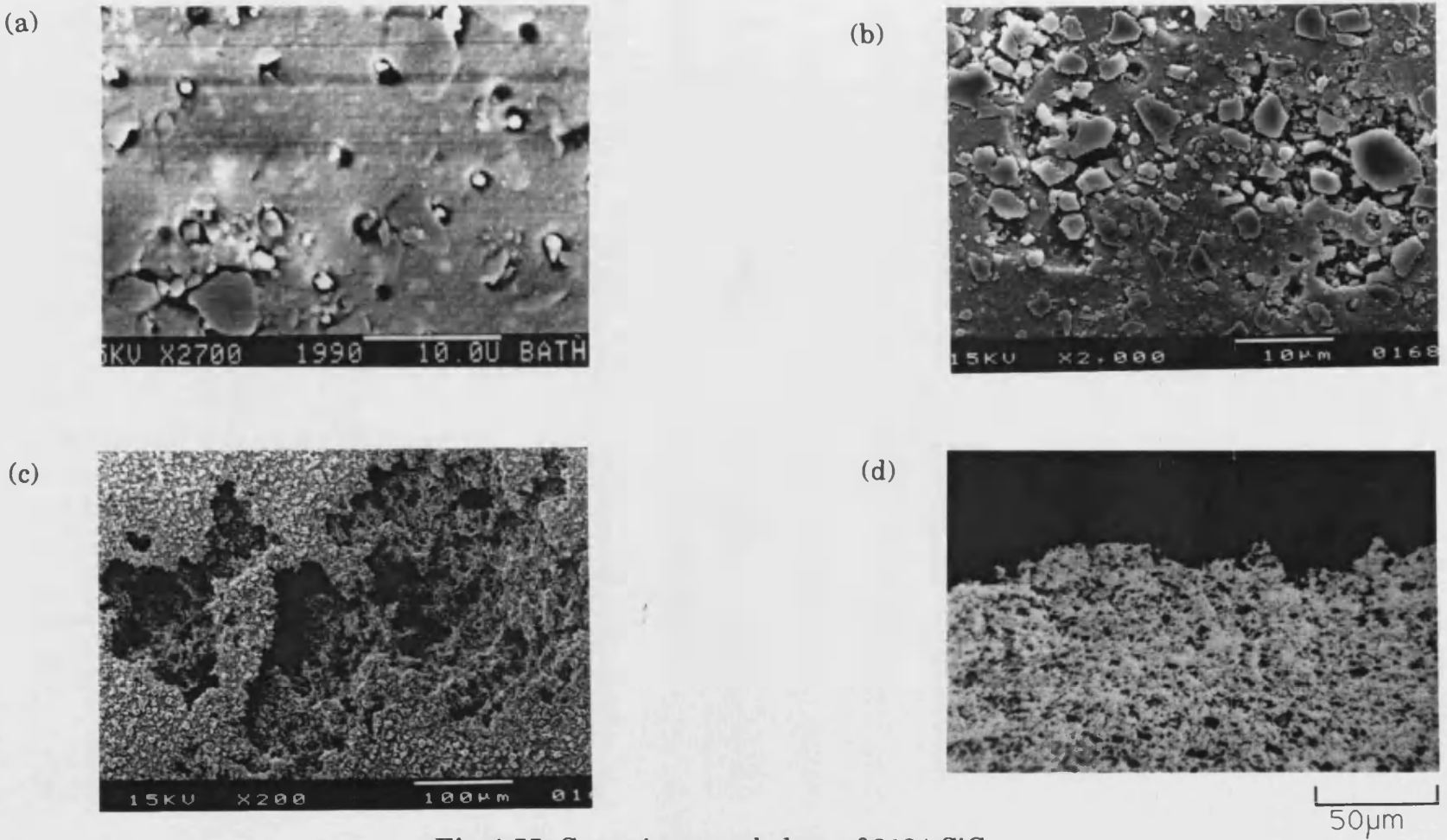

Fig.4.55 Corrosion morphology of 2124-SiC
(a) After 1 day immersion
(b) After 1 week immersion
(c) After 3 week immersion
(d) Cross-section through a specimen after 3 weeks immersion

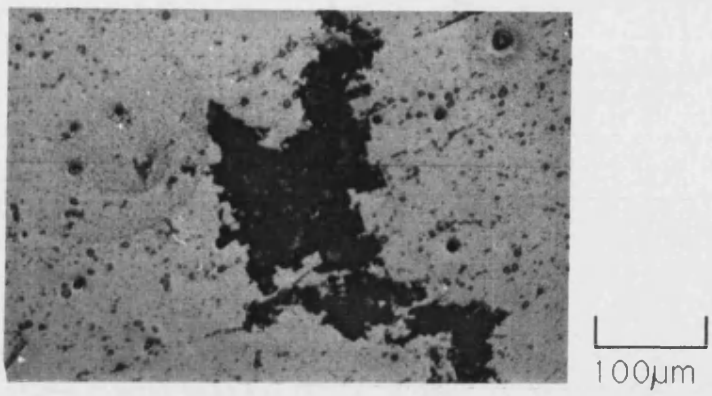

Fig.4.56 Corrosion pit in commercial purity aluminium after DCP test (20mV/min scan rate)

(a)

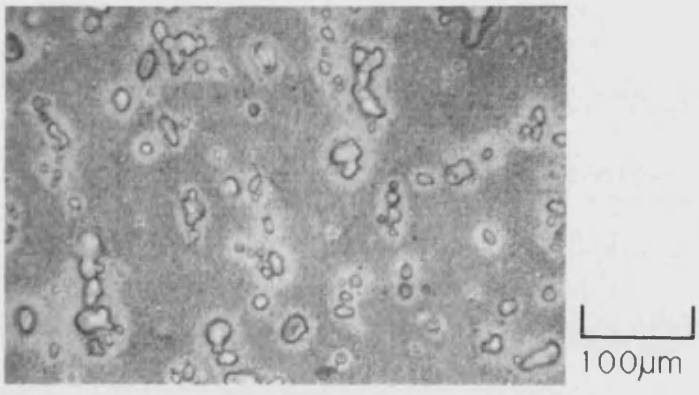

(b)

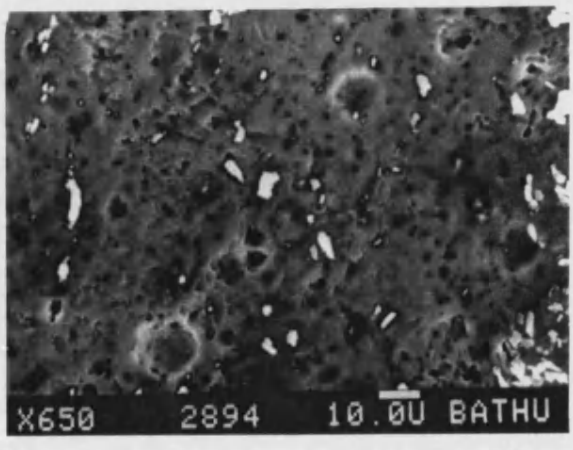

Fig.4.57 Corrosion morphology of commercial purity aluminium
(a) After 1 week immersion
(b) After 3 weeks immersion

(a)

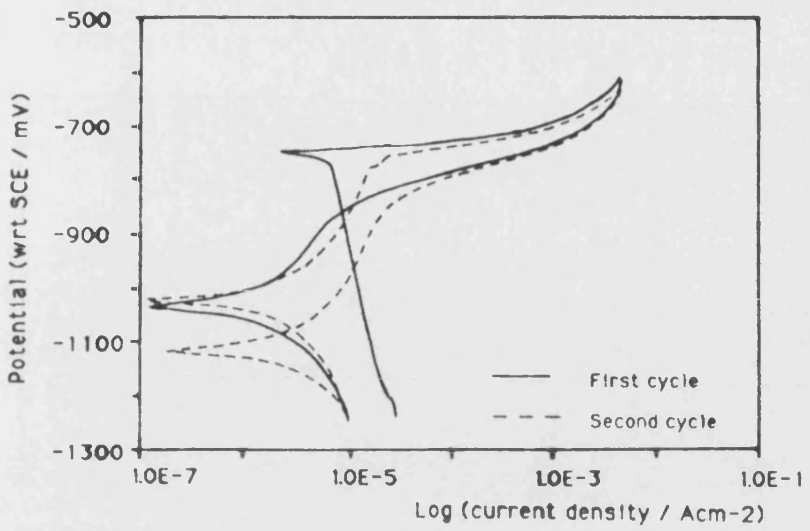

(b)

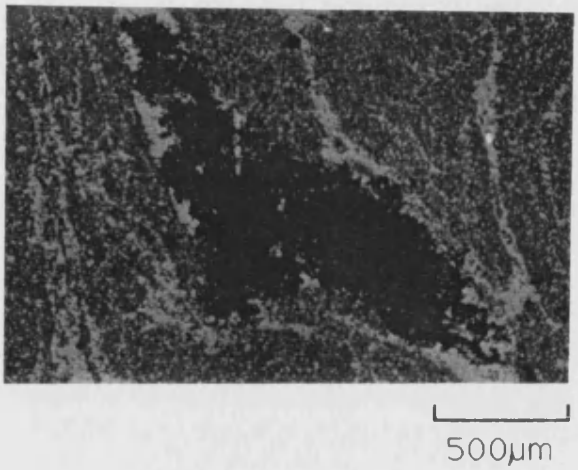

Fig.4.58 The results of DCP tests on Al-C (20mV/min)
(a) A DCP curve
(b) Optical micrograph of a corrosion pit taken after the test

(a)

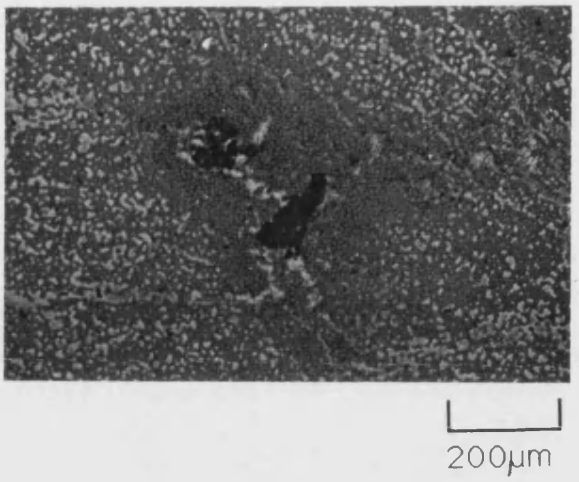

(b)

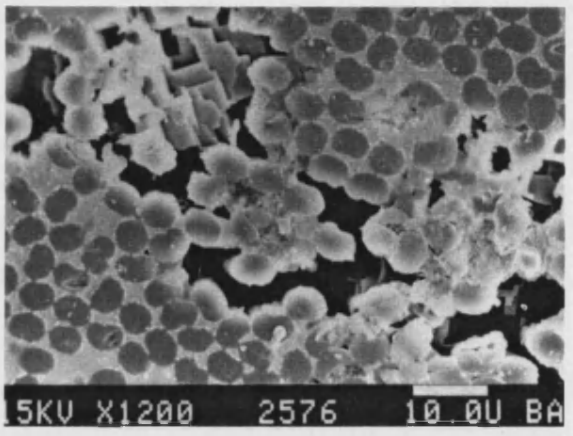

Fig.4.59 Corrosion morphology of Al-C
(a) After 3 days immersion
(c) After 1 week immersion, showing crystallographic attack

(a)

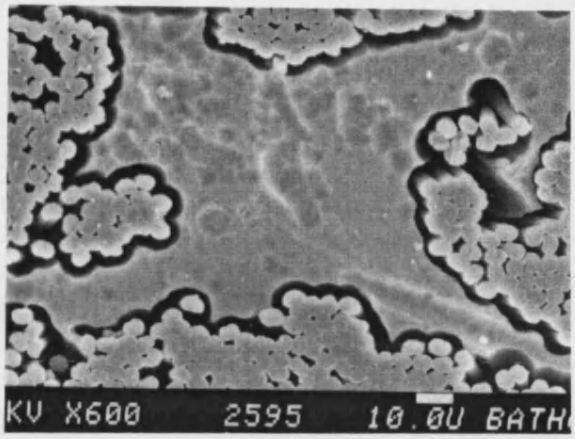

(b)

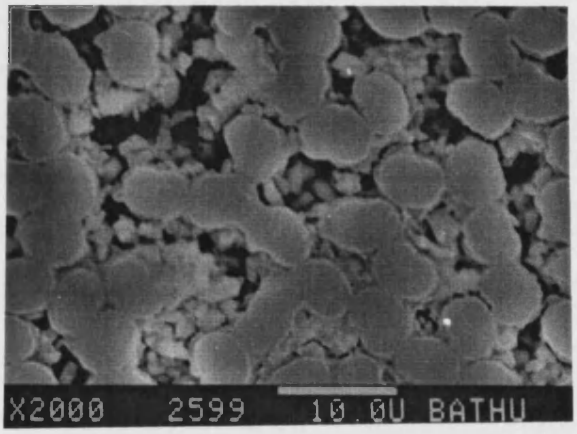

Fig.4.60 Corrosion morphology after 3 weeks immersion
(a) Corrosion around the fibres
(b) Corrosion product trapped between the fibres

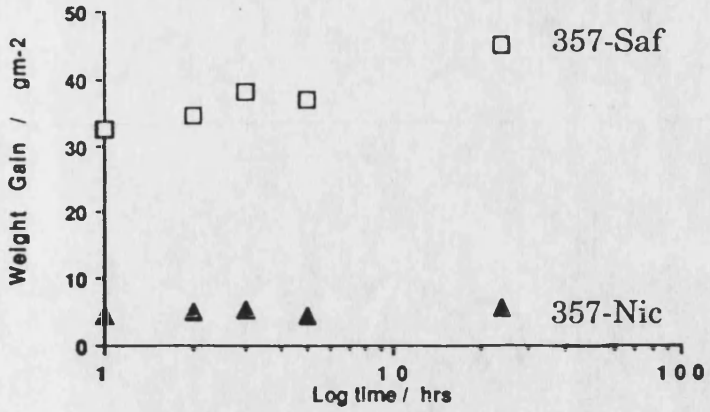

Fig.5.1 The weight gains experienced by specimens of 357-Saf and 357-Nic immersed in distilled water for times of upto 24 hours

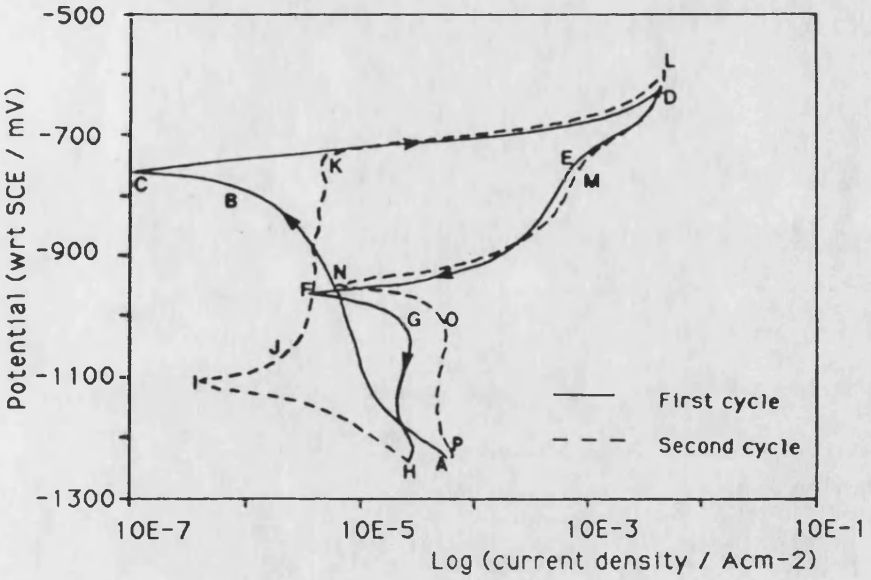

Fig.5.2 Schematic of a DCP curve

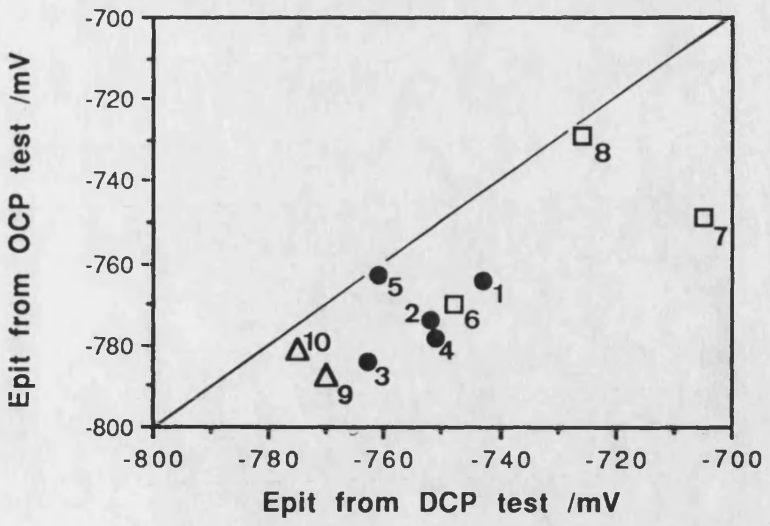

Fig.5.3 The correlation between pitting potentials from OCP and DCP tests

Key: ● 357-based materials
1 357
2 357-C_L
3 357-C_S
4 357-Nic
5 357-Saf

□ 2124-based materials
6 2124
7 2124-C
8 2124-SiC

Δ Al-based materials
9 Al
10 Al-C

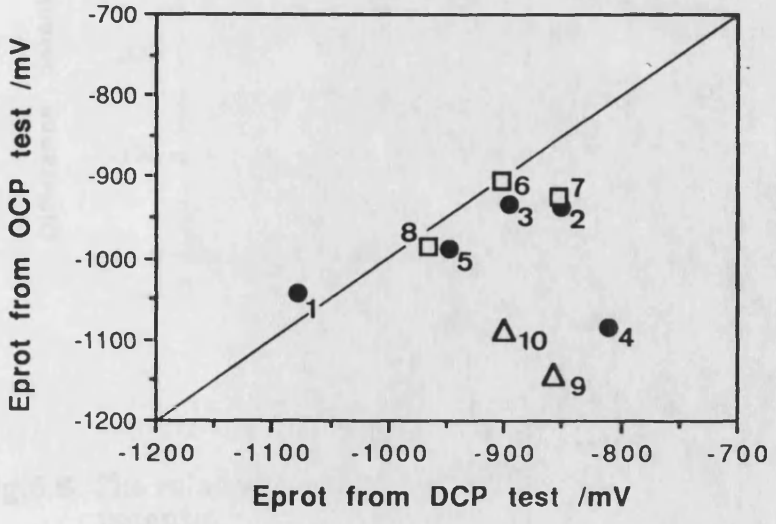

Fig.5.4 The correlation between protection potentials from OCP and DCP tests (see Fig.5.3 for key)

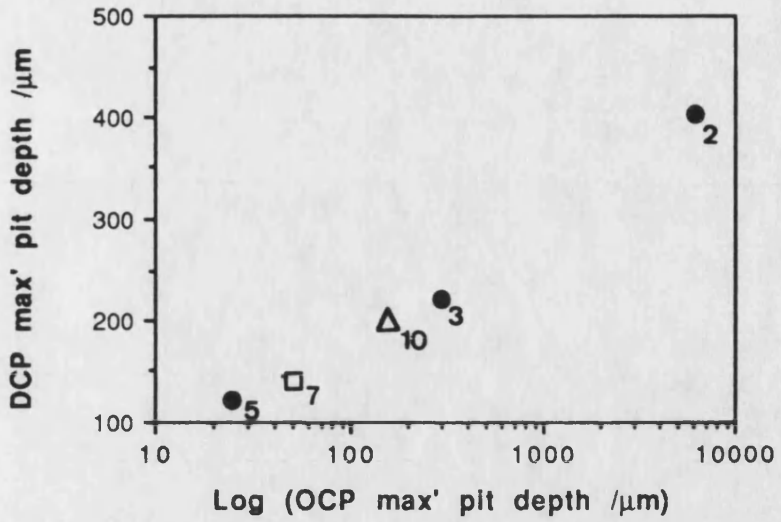

Fig.5.5 The relationship between maximum pit depths measured on specimens from OCP and DCP tests (see Fig.5.3 for key)

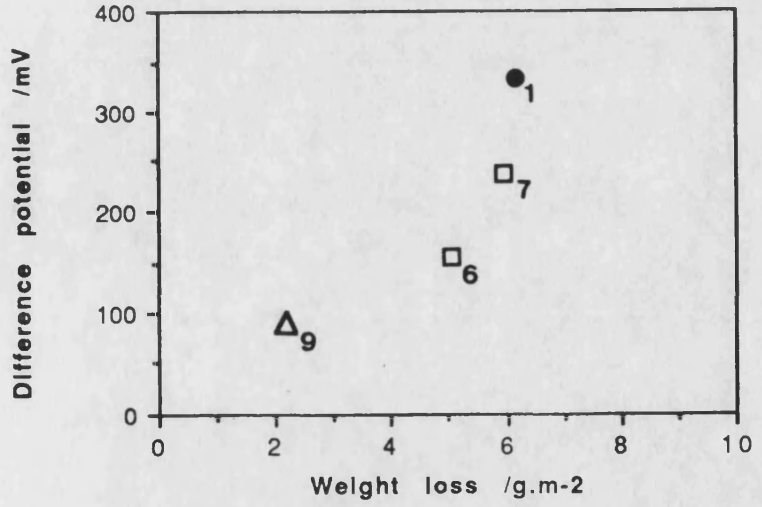

Fig.5.6 The relationship between weight loss data and difference potential for alloys and 2124-SiC (see Fig.5.3 for key)

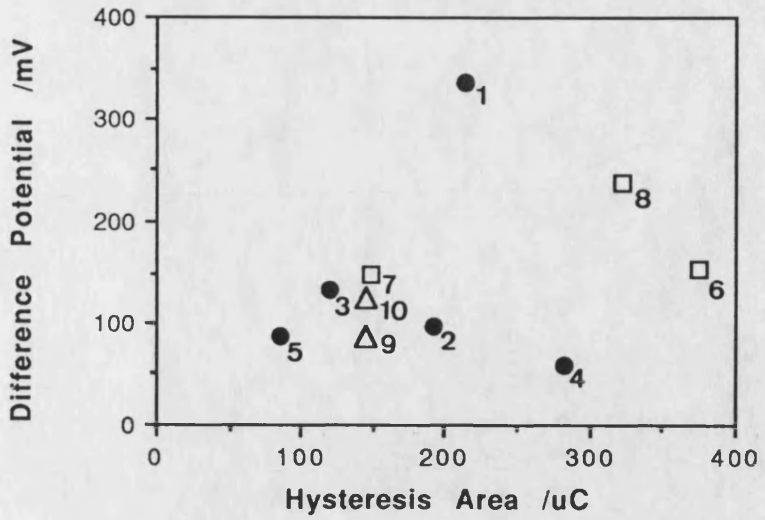

Fig.5.7 The relationship between hysteresis area and difference potential for all materials (see Fig.5.3 for key)

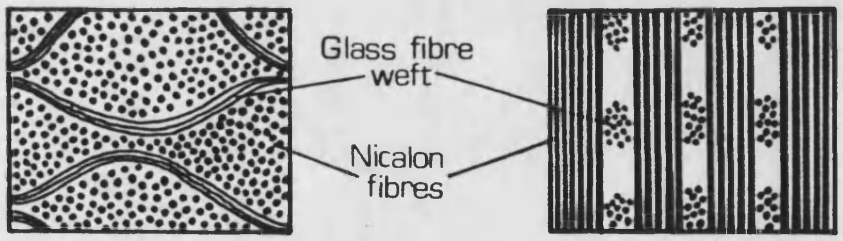

(a) (b)

Fig.5.8 Schematic of 357-Nic (type A)
(a) Transverse section exposing longitudnal glass fibres
(b) Cross-section through the exposed surface showing transverse glass fibres in bundles

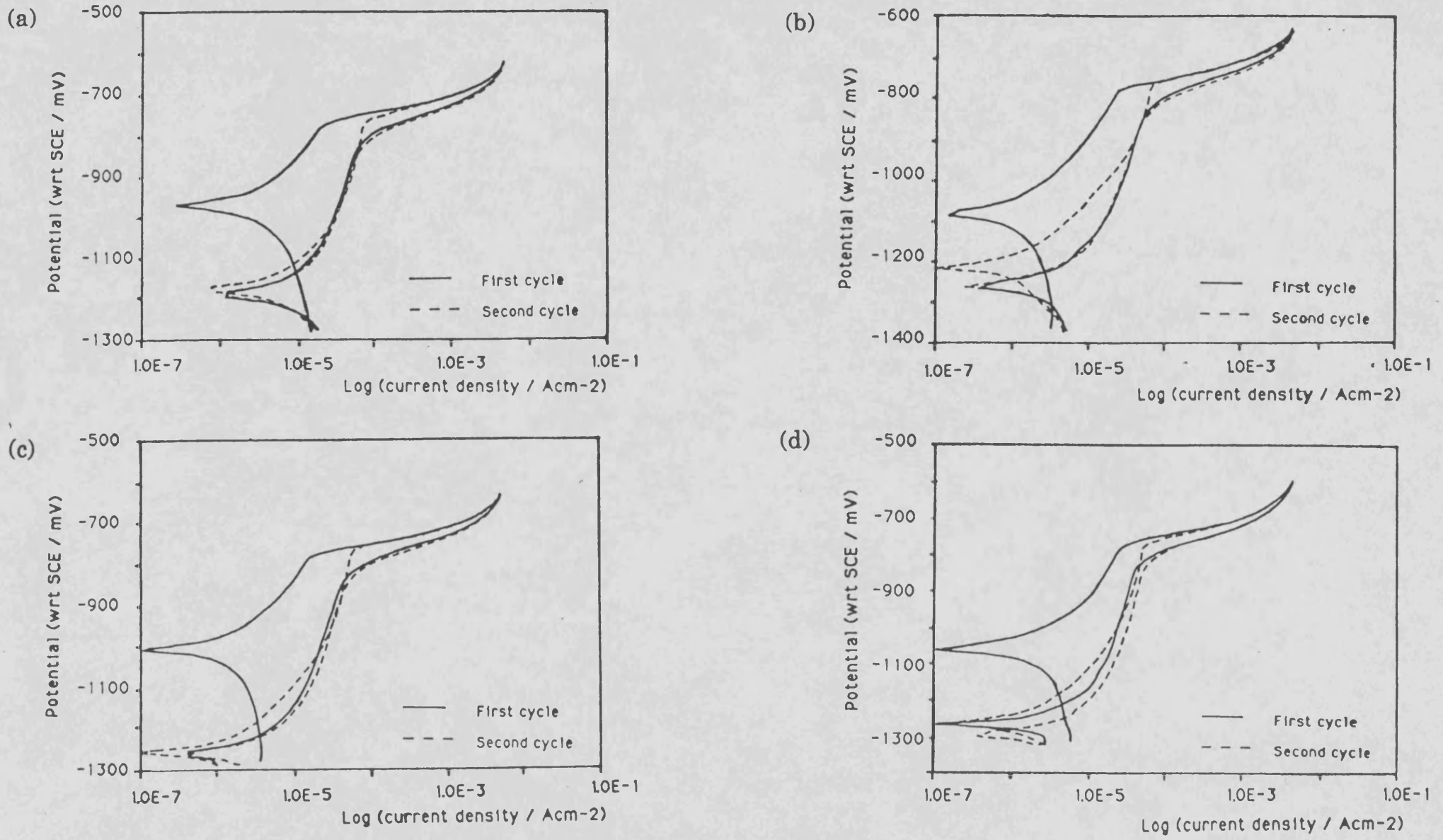

Fig.4.5 DCP curves obtained on single crystals of aluminium different exposed crystallographic orientations (a)(211)(b)(111)(c)(110)and (d)(100)